Analytical modelling and preliminary design of a small-scale experimental whirl flutter demonstrator Université de Liège

Auteur : Di Puma, Léo
Promoteur(s) : Salles, Loïc
Faculté : Faculté des Sciences appliquées
Diplôme : Master en ingénieur civil en aérospatiale, à finalité spécialisée en "aerospace engineering"
Année académique : 2025-2026
URI/URL : http://hdl.handle.net/2268.2/26179

UNIVERSITE DE LIÈGE
FACULTÉ DES SCIENCES APPLIQUÉES

Analytical modelling and preliminary design of a small-scale experimental whirl flutter demonstrator

Léo Di Puma

Thesis presented to obtain the degree of:

Master of Science in Aerospace Engineering

Thesis supervisor:

Professor Loïc Salles

Academic year: **2025 - 2026**

Acknowledgements

First, I would like to thank all the people who contributed to making my academic journey at the University of Liège a successful one. All the people who helped me, guided me, or taught me throughout these years have strengthened my desire to make engineering my profession. They have also contributed to increasing my interest in aerodynamics and aeroelasticity, which has continued to grow throughout this work.

Secondly, I would like to express my sincere gratitude to Professor Loïc Salles for his constant availability and support throughout the entire completion of this work, even when he was abroad. I also wish to thank Professor Thomas Andrianne and Edouard for their valuable help regarding the experimental part of this work. Their scientific expertise, advice, and constructive feedback greatly helped me throughout this project.
I would also like to thank the technicians of the FabLab for their help and support in the design of the required parts of the experimental setup.

Thirdly, thanks to all my friends for the moments of laughter and parties. They are an essential part of my daily happiness.

Finally, and most importantly, I would like to thank my family. I am deeply grateful to my parents, grandparents, brothers, sister, and all my loved ones for their immeasurable support throughout these five years, especially during personally difficult moments. Words are not enough to describe the love I have for them and the gratitude I feel for everything they have given me. I also want to give a special mention to Caro, with whom I have shared this entire journey, which is only the beginning of something amazing.

Abstract

The whirl flutter phenomenon is one of the main concerns when designing aeroelastic structures such as tiltrotor or pylon-propeller systems. First identified by Taylor and Browne in 1938, whirl flutter is a self-excited dynamic aeroelastic instability. It is driven by the coupling between the gyroscopic effects induced by the rotating propeller and the aerodynamic forces acting on the propeller blades. Due to the gyroscopic coupling, two modes appear, namely the forward and backward whirling modes. Depending on the configuration, their stability behaviour can differ.

This work aims to design a small-scale whirl flutter demonstrator in order to support the validation of a finite element-based numerical method for whirl flutter prediction, currently under development at the University of Liège. In particular, the present work investigates the whirl flutter behaviour of two configurations that differ by their source of flexibility. The first one considers a flexible pylon, while the second one considers a rigid pylon with linear traction springs. The results are obtained using an analytical method, which relies on several assumptions and uses a quasi-steady aerodynamic approach.

For both configurations, the results are obtained for the APC 15.75x13-3 propeller, with a rotational speed of 2000 rpm and free-stream velocities ranging from 7 m/s to 13 m/s. They show that only the backward whirling mode leads to whirl flutter, while the forward mode remains stable. Both configurations are compared, and the spring-based one appears to be more convenient from an experimental point of view, since the flexible pylon exhibits significant static tip deflection and rotation.

Finally, experimental procedures for the flexible pylon configuration are presented, and all the components are described in detail. The motor-pylon connection is designed, while the motor-propeller link is also discussed. Additionally, the propeller rotational speed control is described through the use of a pulse-width modulation device.

AI disclaimer

AI, in particular *ChatGPT*[1], was used during the realization of this work. It provided support for LaTeX formatting, as well as for *Python*[2] code debugging. Additionally, it helped with English writing, especially regarding grammar and vocabulary in order to improve the readability and clarity of the report. However, it did not form the basis of any development, scientific reasoning or result interpretation. All conclusions are the sole responsibility of the author and all figures not explicitly sourced were produced by the author. Furthermore, all figures adapted from external sources were fully adapted by the author without using artificial intelligence.

[1]https://chatgpt.com/, accessed: 2026-06-04
[2]https://www.python.org/, accessed: 2026-06-04

Contents

List of Figures

List of Tables

Nomenclature

Symbol	Description
Chapter 3 - Methodology	
$R_1 = (O,\ \mathbf{x}_1,\ \mathbf{y}_1,\ \mathbf{z}_1)$	Reference frame in which the equations of motion are written
$R_2 = (C,\ \mathbf{x}_2, \mathbf{y}_2, \mathbf{z}_2)$	Moving frame located at the propeller centre
$R_{b_n} = (C,\ \mathbf{x}_{b_n},\ \mathbf{y}_{b_n},\ \mathbf{z}_{b_n})$	Undeformed blade moving frame
$\bar{R}_{b_n} = (P',\ \bar{\mathbf{x}}_{b_n},\ \bar{\mathbf{y}}_{b_n},\ \bar{\mathbf{z}}_{b_n})$	Deformed blade moving frame
$\mathbf{R}_n$	Transfer matrix from R_{b_n} to R_1
$\mathbf{P}_n$	Transfer matrix from R_{b_n} to R_2
$\bar{\mathbf{R}}_n$	Transfer matrix from $\bar{R}_{b_n}$ to R_1
P_A	Virtual power of acceleration
P_{int}	Virtual power of internal forces
P_{ext}	Virtual power of external forces
$\hat{\mathbf{y}}$	Kinematically admissible virtual velocity field
$\mathbf{u}_c$	Vector of translational degrees of freedom of the propeller centre
$\boldsymbol{\theta}_c$	Vector of rotational degrees of freedom of the propeller centre
θ, ψ, φ	Pitch, yaw, and roll rotational degrees of freedom of the pylon, respectively
u_c^x, u_c^y, u_c^z	Translations of the propeller centre along the $\mathbf{x}_1-$, $\mathbf{y}_1-$ and $\mathbf{z}_1-$directions, respectively
N	Number of propeller blades
α	Blade azimuthal angle
β	Angular spacing between two consecutive blades
q_{pylon}	Number of pylon degrees of freedom
$h(r)$, $w(r)$, $v(r)$, $\theta_t(r)$	Radial distributions of the blade in-plane bending, traction, out-of-plane bending and torsion, respectively
θ_h, θ_v	Blade deformation angles associated with blade in-plane, and out-of-plane bending, respectively
$q_h^{(i)}$, $q_w^{(i)}$, $q_v^{(i)}$, $q_t^{(i)}$	Generalized coordinates associated with in-plane bending, traction, out-of-plane bending and torsion, respectively
N_h, N_w, N_v, N_t	Number of shape functions associated with in-plane bending, traction, out-of-plane bending and torsion, respectively

Symbol	Description
$\mathbf{\Phi}$	Matrix gathering the shape functions associated with in-plane, out-of-plane bending, and traction
$\mathbf{q}_n$	Vector gathering the generalized coordinates associated with in-plane, out-of-plane bending and traction relative to the n^{th} blade
$\mathbf{\Phi}_t$	Matrix gathering the shape functions associated with torsion
$\mathbf{t}_n$	Vector gathering the torsional generalized coordinates of the n^{th} blade
K_θ, K_ψ	Pitch and yaw rotational stiffnesses of the pylon, respectively
C_θ, C_ψ	Pitch and yaw damping coefficients of the pylon, respectively
R_p	Propeller radius
r_0	Propeller hub radius
L	Blade length
L_{pylon}	Pylon length
Ω	Propeller rotational speed
V	Free-stream velocity
$\mathbf{v}_\infty$	Free-stream velocity vector in frame R_1
r	Blade radial location
J_1^p, J_2^p	Polar and transverse mass moments of inertia of the pylon expressed at the pivot point, respectively
J_1, J_2	Polar and transverse mass moments of inertia of the propeller expressed at the propeller centre, respectively
J_1^h, J_2^h	Polar and transverse mass moments of inertia of the propeller hub expressed at the propeller centre, respectively
m_{motor}	Motor mass
ρ_b	Blade density
E_b	Young's modulus of the blade
G_b	Shear modulus of the blade
$S(r)$	Blade cross-section at radial location r
I_x, I_z	Second moments of area of the blade beam section about $\mathbf{x}_{b_n}$ and $\mathbf{z}_{b_n}$, respectively
I_y	Polar second moment of area of the blade beam section
$\mathbf{J}$	Inertia matrix of the cross-sections of the blade
$c(r)$	Blade chord at radial location r

Symbol	Description
$t(r)$	Blade maximum thickness at radial location r
γ	Blade twist angle
$\mathbf{u}$	Relative flow velocity at a blade section expressed in $\bar{R}_{b_n}$
V_a, V_t	Axial and tangential induced velocities, respectively
u_P^0, u_T^0	Steady parts of the out-of-plane and in-plane relative velocities of a blade section, respectively
C_{3D}	Finite blade length correction
$\mathbf{P}_{tot}$	Coordinate transformation matrix
$\mathbf{y}$	Vector gathering the generalized coordinates of the blades, sorted by blades, and those of the pylon
$\mathbf{y}_\xi$	Vector gathering the generalized coordinates of the blades, sorted by shape functions, and those of the pylon
f_{cx}^{stat}	Static force applied along the propeller axis
$\mathbf{T}$	MBC transformation matrix
$\boldsymbol{\xi}$	Multi-blade coordinate vector
ρ_a	Air density
α_0	Zero-lift angle of attack
ϕ_0	Steady inflow angle of a blade section
m_0	Static pitching moment per unit length of a blade section
C_L, C_D	Blade profile lift and drag coefficients, respectively
a_l	Lift-curve slope of a blade section with finite blade length correction
C_{flex}, C_{tor}, C_{tract}	Structural damping coefficients associated with bending, torsion, and traction, respectively
σ	Real part of an eigenvalue
ω	Imaginary part of an eigenvalue
f	Mode oscillation frequency
T	Mode period
$\boldsymbol{\phi}_r$, $\boldsymbol{\psi}^H$	Right and left eigenvectors of a mode, respectively
Δ	Phase difference between yaw and pitch motions
R	Amplitude ratio between yaw and pitch motions
W_a	Aerodynamic work over one period associated with a mode
P_a	Mean aerodynamic power over one period associated with a mode

Symbol	Description
δ_{tip}	Static tip deflection
θ_{tip}	Static tip rotation angle
Chapter 4 - Analytical modelling of the whirl flutter demonstrator	
C_T, C_P	Propeller thrust and power coefficients, respectively
L_{motor}	Motor length
E_{pylon}	Young's modulus of the pylon
ρ_{pylon}	Density of the pylon
V_{crit}	Critical speed
I_{pylon}	Second moment of area of the pylon cross-section
x_0	Initial elongation of the linear springs
k_z, k_x	Linear spring stiffness coefficients associated with pitch and yaw motion, respectively

Chapter 1. Introduction

1.1 Context and motivations

In the mid-2010s, urban air mobility started to gain importance in the transport sector. Indeed, large cities are facing increasing mobility and infrastructure problems, due to rapid urbanisation and population growth. Additionally, urbanisation contributes to pollution, traffic jams and congestion, leading to a negative impact on the population.
Therefore, mobility in cities needs to be reconsidered in order to reduce congestion and enable faster and more convenient travel between different points within a city [1]. During the last 15 years, many studies have been conducted on urban air mobility, confirming the growing interest in this technology as a potential solution to improve urban mobility [2]. Figure 1.1 represents the evolution of the number of scientific publications on urban air mobility over the years, from 2010 to 2024.

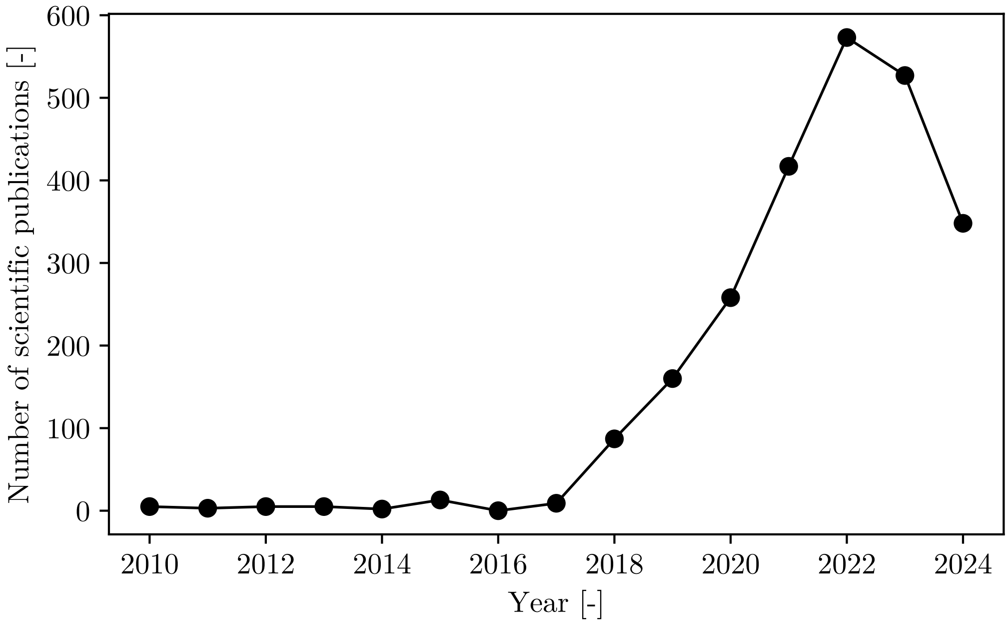

Figure 1.1: Evolution of the number of scientific publications over the years, from 2010 to 2024, reproduced from [3].

One possible solution is the use of electric vertical take-off and landing (eVTOL) aircraft. Equipped with distributed propulsion systems, this type of aircraft is capable of transporting passengers or goods within and around urban areas. Figure 1.2 shows two examples of such aircraft configurations.

(a) eVTOL Joby Aviation S4, carrying four passengers and one pilot, with six electric motors powering tilting propellers, with a maximum range of 214 km and a maximum speed of 321 km/h [4].

(b) eVTOL EH216, developed by EHang, carrying two passengers, with sixteen independent rotors, with a maximum range of 35 km and a maximum speed of 135 km/h [5].

Figure 1.2: Joby Aviation S4 and EH216 eVTOL aircraft configurations [4, 5].

Although the present work does not focus directly on urban air mobility, this context highlights the growing importance of propeller-driven and distributed propulsion systems, for which aeroelastic stability remains a critical design concern. Due to their distributed propeller systems, such aircraft may be subjected to aeroelastic instabilities, as is also the case for helicopters, tiltrotors, and classical propeller systems.

Aeroelasticity is therefore one of the main concerns when designing aeronautical structures. It considers the interaction between the incoming flow and the structure, which is critical for the stability of a body within a fluid. Based on Collar's work, aeroelastic problems can be divided according to three types of forces: elastic, aerodynamic, and inertia forces. He defined a triangle, known as Collar's triangle, representing these forces and the interactions between them [6]. The triangle is represented in Figure 1.3.

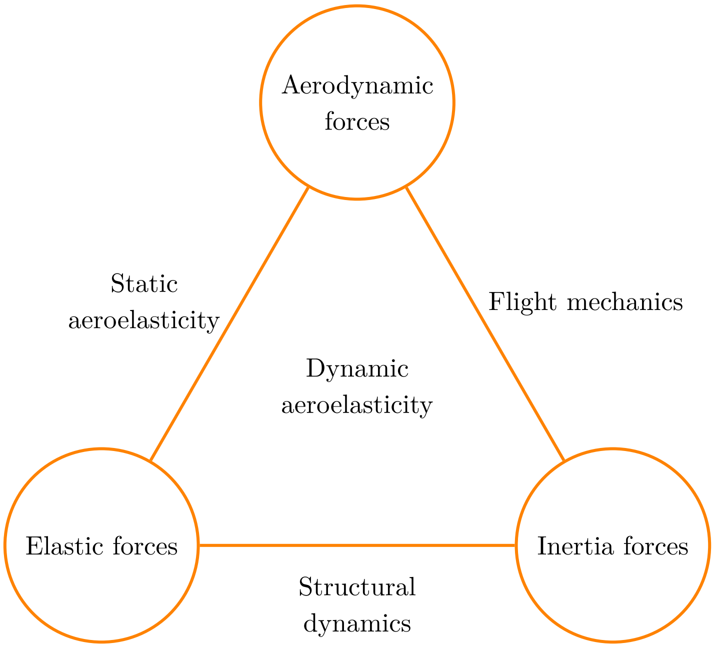

Figure 1.3: Aeroelastic Collar's triangle, reproduced from [6, 7].

For aircraft structures, both dynamic and static aeroelastic instabilities can occur. In the scope of this work, static instabilities are not discussed. In particular, this work focuses on whirl flutter, a dynamic aeroelastic instability that can occur in propeller-driven configurations.
The word *whirl* describes the precession of the propeller rotational axis around its equilibrium position, while *flutter* denotes a dynamic aeroelastic instability caused by the coupling between aerodynamic forces and structural motion.

This whirl flutter instability was first identified by Taylor and Browne in 1938 [8]. When studying vibrations in aircraft structures, they discovered a low-frequency precession that became unstable due to aerodynamic effects. At this stage, the phenomenon had not yet been named whirl flutter, but the observations correspond to the first known description of this instability.
Nevertheless, based on their work, this self-excited vibration was unlikely to occur in practical aircraft structures, as long as a small amount of friction was present. Therefore, it was only possible to observe this instability for structures intentionally built without significant friction [8].
A few years later, in 1945, Ribner based his work on Lanchester's findings that a propeller in yaw generates a side force [9]. Thus, he identified propeller aerodynamic derivatives due to motions and velocities in the yaw and pitch directions. These quantities are key parameters for determining the whirl flutter behaviour of the structure as a function of the aerodynamic parameters.

Nevertheless, it was only after the accidents involving the Lockheed L-188 Electra, a four-engine turboprop airliner, in 1959 and 1960 that this previously unnamed instability attracted renewed attention [7]. These accidents enabled whirl flutter to be studied in depth for turboprop and tilt-rotor aircraft, as well as for helicopters.

For aircraft configurations, propeller whirl flutter is defined as a dynamic instability occurring in a flexibly mounted aircraft engine-propeller combination [10]. It involves a coupling between aerodynamic and gyroscopic forces, resulting in a precession motion of the propeller rotational axis. Following both accidents, engineers decided to build an experimental model of the aircraft in order to identify the key parameters contributing to this instability [10]. A picture of this reduced-scale experimental model is shown in Figure 1.4.

They observed propeller whirl flutter at high forward speeds and for sufficiently low engine support stiffnesses. Such low stiffnesses can occur, for example, when the engine support structure is damaged. In the undamaged condition, the aircraft appeared to be safe with respect to whirl flutter [11].

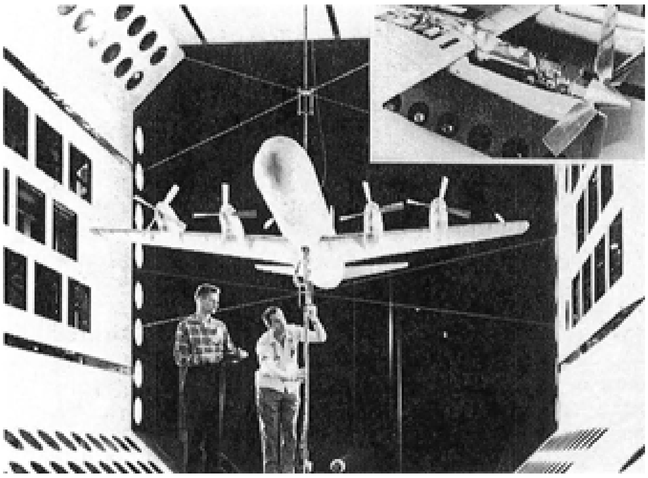

Figure 1.4: Reduced-scale experimental model of the Lockheed L-188 Electra aircraft in the NASA Langley wind tunnel facilities [11].

Since that time, whirl flutter has become an important concern for wind turbines, aircraft and helicopter applications. Additionally, many analytical methods have been developed for the prediction of the whirl flutter behaviour of aeronautical structures. Some of them are presented in the analytical methods state of the art in Section 2.2.

1.2 Thesis objectives

The first objective of this work is to implement an analytical method in order to describe the aeroelastic behaviour of a pylon-propeller structure. This method allows the whirl flutter stability boundaries of the system to be predicted as functions of the free-stream velocity and the pitch and yaw stiffnesses of the pylon. Then, the method is applied to a realistic case, using real propeller geometry and performance, in order to obtain physically interpretable quantities. Two different theoretical configurations are studied in order to compare their behaviour and assess their practical feasibility.

Finally, based on the analytical results, the second objective is to develop the preliminary design of an experimental setup allowing the observation of whirl flutter for well-defined operating conditions identified by the analytical method. This setup is designed to validate a finite element-based numerical method currently under development at the University of Liège [12]. However, this numerical method is not used for the experimental design in the present work, for which the analytical approach is preferred.

The final goal is to define and design in detail all the components required for a cost-effective small-scale demonstrator.

1.3 Thesis outline

First, Chapter 2 introduces the whirl flutter aeroelastic instability by providing a detailed physical description. It also gives an overview of existing analytical methods, whirl flutter experimental demonstrators, and some numerical approaches used for aeroelastic stability prediction.

Then, Chapter 3 presents the complete analytical method, from the derivation of the equations of motion to the identification of the whirl flutter modes.

Using the elements defined in this chapter, two possible setup configurations are analysed in Chapter 4. For both configurations, the influence of several model parameters, such as stiffness and free-stream velocity, is investigated. Their whirling nature is verified and their ability to lead to whirl flutter is studied. Additionally, a comparison between both configurations is also provided.

Furthermore, Chapter 5 describes in detail the experimental procedures and the setup components for one of the configurations. This chapter therefore provides a practical application of one of the analytical models presented in Chapter 4.

Finally, Chapter 6 concludes the thesis and presents possible future work to continue this study.

Chapter 2. State of the art

This chapter introduces the whirl flutter phenomenon and its main physical mechanisms. It also presents analytical methods that have been used in the past to characterize the whirl flutter behaviour of propeller systems. Methods involving different numbers of degrees of freedom are discussed, together with comments on existing aerodynamic formulations, ranging from quasi-steady to unsteady models. Finally, existing experimental setups are presented and some numerical approaches are briefly discussed.

2.1 Whirl flutter physical description

Whirl flutter is a self-excited dynamic aeroelastic instability that can occur, for instance, in propeller systems. It emerges from the coupling between gyroscopic effects induced by the rotating propeller and the aerodynamic forces acting on the propeller blades.

The physical mechanism of whirl flutter can be understood using a simplified model, in which a propeller with rigid blades is mounted on a pylon that is flexible in both pitch and yaw.
Without propeller rotation and without aerodynamic forces, the pylon has two distinct modes in the pitch and yaw planes. These modes vibrate independently, without coupling. They are represented in Figure 2.1 [7, 13].

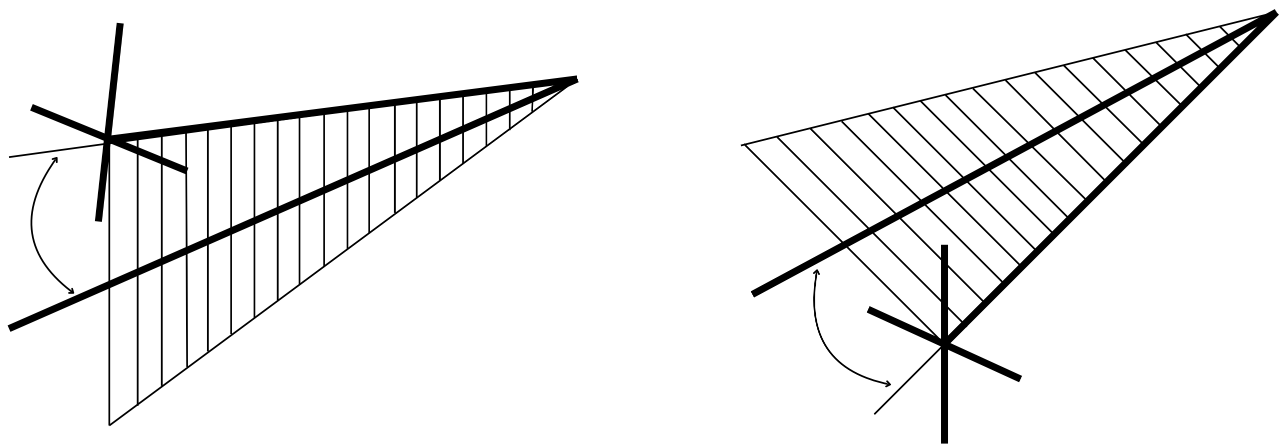

(a) Independent pitch mode. (b) Independent yaw mode.

Figure 2.1: Independent pitch and yaw modes of a non-rotating rigid four-bladed propeller not subjected to aerodynamic force, adapted from Reed [10].

The whirling motion appears when the propeller has a non-zero rotational speed. The two previously independent modes then become coupled, due to gyroscopic effects, leading to the appearance of two natural precession modes.

On the one hand, the frequency of one mode increases as the propeller rotational speed increases. On the other hand, the frequency of the other mode decreases with the rotational speed. The first one is called the forward mode, since its whirling direction is the same as the propeller rotation, while the second is the backward mode, since it whirls in the opposite direction to the propeller. This is how both whirling modes emerge: they are created through gyroscopic coupling. Both precession modes are shown in Figure 2.2, where Ω denotes the rotational speed of the propeller.
Nevertheless, these modes are not necessarily unstable, since the onset of whirl flutter is caused by the aerodynamic forces acting on the propeller blades [7, 13].
Even in the case of a perfectly symmetric system in terms of pitch and yaw stiffnesses, both whirling modes do not have the same oscillatory frequency. In general, the backward mode corresponds to the lower frequency, while the forward mode corresponds to the higher one [10].

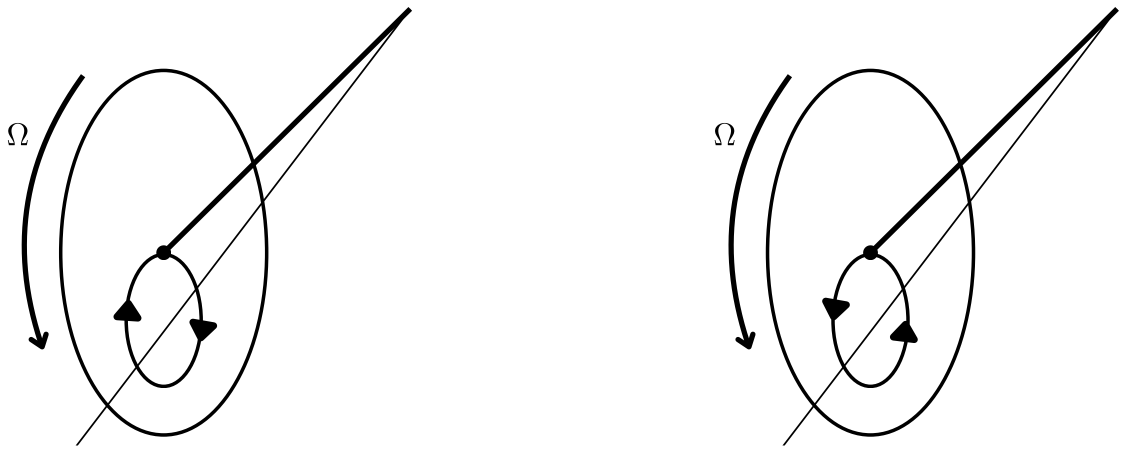

(a) Backward precession mode. (b) Forward precession mode.

Figure 2.2: Backward and forward precession modes with Ω the rotational speed of the propeller, adapted from Reed [10].

Both modes are associated with complex eigenvalues, meaning that they are oscillatory modes. In the ideal case, the pitch and yaw stiffnesses are equal, so that the whirling motion describes a circular motion instead of an elliptical one. Additionally, a whirling mode is characterized by a $\pm 90°$ phase shift between the pitch and yaw motions in the ideal symmetric case [7].

Furthermore, once the origin of the precession motion has been identified, the instability mechanism can be explained by introducing the aerodynamic forces.
When the pylon is whirling, the orientation of the propeller plane changes, which induces a variation in the angle of attack of the blades. As a result, aerodynamic forces act on the propeller plane and can drive the instability by transferring energy to the whirling motion. This mechanism can be understood through a simple illustrative case. Considering a small pitch inclination θ of the propeller shaft due to the pylon precessing motion, the incoming velocity has a cross-flow component V_θ with respect to

the propeller disk. This situation is shown in Figure 2.3.

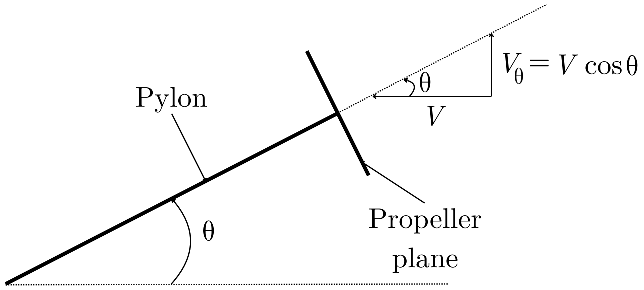

Figure 2.3: Representation of the cross-flow component V_θ of the free-stream velocity V induced by a pitch rotation θ of the propeller plane caused by the pylon whirling motion.

The blades on the ascending side experience a reduced relative velocity and a reduced angle of attack, because the cross-flow velocity component decreases both quantities on this side. In contrast, the cross-flow velocity component increases both the relative velocity and the blade angle of attack for the blades on the descending side. When the lift force variations induced by these changes in angle of attack and relative velocity are projected onto directions parallel and normal to the propeller disk plane, and then integrated over one propeller revolution, they produce a resultant vertical force and a yawing moment. The vertical force acts in a direction that increases the pitch angle, therefore opposing the restoring force of the structural spring. A similar physical mechanism can be described when an initial yaw angle ψ is considered [10].

In a manner similar to classical wing flutter, once the incoming flow velocity exceeds the critical speed, the system becomes unstable. However, when considering a rigid-blade propeller, the backward mode is the one expected to become unstable, while the forward mode remains stable [7, 13]. If the blades are flexible, the forward mode can also become unstable [14]. Moreover, according to Reed, the propeller thrust has only a small effect on the whirl flutter stability boundaries. He also states that, for very low mounting stiffnesses, the system can exhibit static divergence [10].

2.2 Existing analytical methods

Several analytical methods exist and allow the behaviour of an aeroelastic structure to be predicted. In this section, two historically important methods are presented, as they were established in the early stages of whirl flutter studies.

2.2.1 Two-degrees-of-freedom model

This two-degrees-of-freedom model is taken from the 1961 work of Reed and Bland [15]. This model considers a rigid-blade propeller mounted on a pylon that is flexible in pitch and yaw. Therefore, the two degrees of freedom are θ, the pitch angle, and ψ, the yaw angle. The system is represented in Figure 2.4.

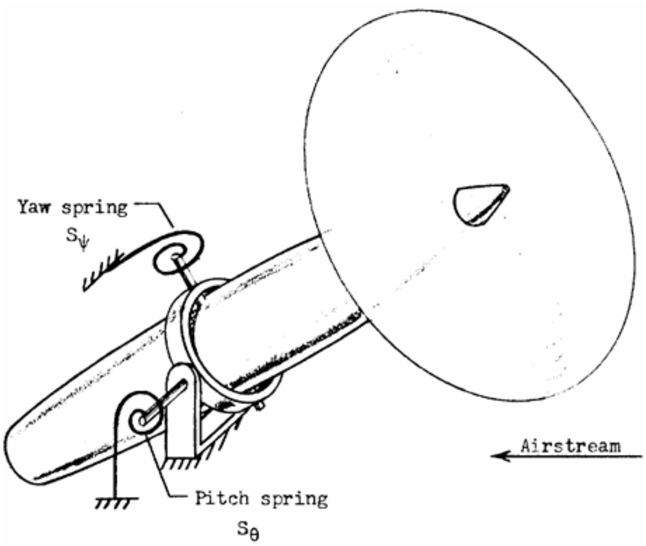

Figure 2.4: Representation of the idealized system used to derive the two-degrees-of-freedom model, with pitch and yaw springs [15].

The equations of motion are derived from Lagrange's principle. The Lagrange equation is written as:

$$\frac{d}{dt}\left(\frac{\partial T}{\partial \dot{q}_i}\right) - \frac{\partial T}{\partial q_i} + \frac{\partial U}{\partial q_i} + \frac{\partial D}{\partial \dot{q}_i} = Q_{q_i}, \tag{2.1}$$

where q_i denotes the generalized coordinate, either θ or ψ, T is the kinetic energy, U is the potential energy, D is a dissipation function and Q_{q_i} is the generalized moment associated with q_i.

Assuming small pitch and yaw deflections around the gimbal axis, the total kinetic energy of the system is given by [15]:

$$T = \frac{1}{2} I_X \left(\Omega^2 + 2\Omega\dot{\theta}\psi\right) + \frac{1}{2} I_Y \left(\dot{\theta}^2 + \dot{\psi}^2\right) \tag{2.2}$$

where Ω is the rotational speed of the propeller, I_X is the polar moment of inertia of the propeller and $I_Z = I_Y$ are the moments of inertia of the complete system about the **Z**- and **Y**-axes.
The total potential energy of the system is given by:

$$U = \frac{1}{2} S_\theta \theta^2 + \frac{1}{2} S_\psi \psi^2, \tag{2.3}$$

where S_θ and S_ψ are the rotational stiffnesses of the pitch and yaw springs, respectively.

By considering a damping force in phase with the oscillation velocity and proportional to the elastic restoring force, the dissipation function is written as:

$$D = \frac{1}{2}\frac{S_\theta g_\theta}{\omega}\dot{\theta}^2 + \frac{1}{2}\frac{S_\psi g_\psi}{\omega}\dot{\psi}^2, \tag{2.4}$$

where ω is the oscillation frequency, and g_θ and g_ψ are the damping coefficients of the uncoupled pitch and yaw modes, respectively.

Furthermore, M_Y and M_Z are the aerodynamic pitch and yaw moments of the propeller about the gimbal axes, such that:

$$Q_\theta = M_Y \qquad \text{and} \qquad Q_\psi = M_Z. \tag{2.5}$$

By substituting these expressions into the Lagrange equation given in Equation 2.1, the equations of motion become:

$$\begin{cases} I_Y\ddot{\theta} + I_X\Omega\dot{\psi} + S_\theta\theta + \frac{S_\theta g_\theta}{\omega}\dot{\theta} = M_y \\ I_Y\ddot{\psi} - I_X\Omega\dot{\theta} + S_\psi\psi + \frac{S_\psi g_\psi}{\omega}\dot{\psi} = M_Z. \end{cases} \tag{2.6}$$

The aerodynamic pitch and yaw moments can be expressed as functions of the aerodynamic derivatives, whose expressions are derived in the work of Reed and Bland [15]. However, these aerodynamic derivatives are evaluated using Ribner's method, originally derived in 1945 [16].

This two-degrees-of-freedom method already shows some relevant trends, such as the evolution of stability boundaries with respect to thrust, Mach number, and yaw-to-pitch stiffness ratio $\frac{S_\psi}{S_\theta}$.

2.2.2 Wing flexibility

In the model previously presented in Section 2.2.1, the propeller system was attached to a rigid wing. Zwaan and Bergh studied the influence of wing flexibility on whirl flutter stability boundaries when the propeller is attached to a flexible wing [17]. The considered system is represented in Figure 2.5, where the wing flexibility is taken into account through wing bending and wing torsion.

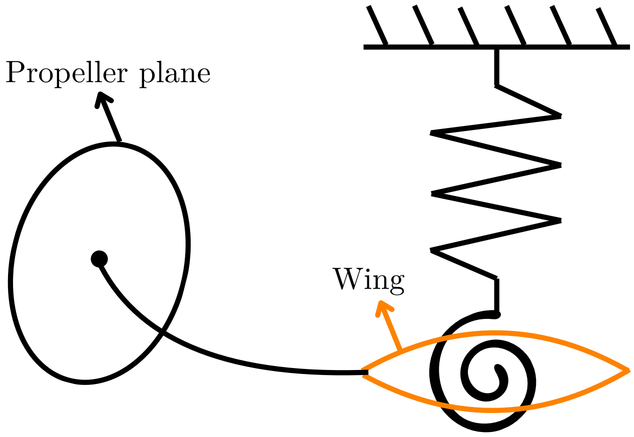

Figure 2.5: Representation of the four degrees of freedom model, in which wing flexibility is taken into account through wing torsion and bending, adapted from Cecrdle [7].

The model is not developed in detail here, but it follows the same principle as the two-degrees-of-freedom model. First, the energies are expressed and then introduced into the Lagrange formulation of Equation 2.1 in order to obtain the equations of motion [7, 17]. However, the aerodynamic interaction between the propeller and the wing is neglected.

In general, wing flexibility appears to have a stabilizing effect on the whirl flutter behaviour of a system, as shown in Figure 2.6. Nevertheless, for some configurations, it can reduce the whirl flutter critical speed.

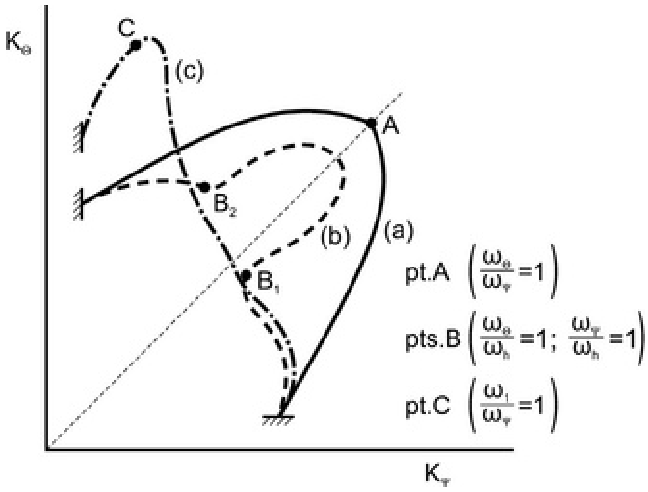

Figure 2.6: Whirl flutter stability boundaries of the four-degrees-of-freedom model, represented as the pitch stiffness K_θ as a function of the yaw stiffness K_ψ, for three different cases. Case A corresponds to a rigid wing, case B to a wing flexible in bending, and case C to a wing flexible in both bending and torsion [7].

It can be seen that the whirl flutter stable region increases for most stiffness values when wing flexibility is taken into account. Point C in Figure 2.6 shows the interaction between the torsional mode, or the coupled bending torsional mode, and the propeller pitch motion, since these wing motions involve a pitching motion of the propeller [7].

2.2.3 Other analytical methods

In addition to their number of degrees of freedom, analytical methods can also differ through their aerodynamic model, which can for example be based on quasi-steady or unsteady assumptions. Under the quasi-steady approximation, the flow adapts instantaneously to the propeller motion, thus neglecting the time-dependent behaviour of the flow.

For instance, the quasi-steady method introduced by Houbolt and Reed uses a linearized version of strip theory, which consists in dividing the blade into several radial sections [18]. They also developed another model based on the same strip theory formulation, but including Theodorsen's function to model the unsteady lift lag. Theodorsen's function is a complex function expressed in the frequency domain used to construct circulatory aerodynamic forces resulting from the harmonic oscillation of a flat plate in an incompressible flow. Several simplifications of this function are often used in aerodynamic models [19].
Additionally, Wagner developed a model using the strip theory with airfoil polars, together with Wagner's function to model the unsteady lift lag. Wagner's function is equivalent to Theodorsen's function, but formulated in the time domain rather than in the frequency domain [20, 21]. Wagner also proposed a method combining the previously described Wagner formulation with blade element momentum theory, in order to model the induced velocities [22–24].

2.3 Existing experimental setups

Several experimental setups have been designed and tested, each with its own goals and objectives. They can be classified according to their scale. First, two medium-scale demonstrators are presented, one of which corresponds to the first experimental whirl flutter study. Then, a small-scale demonstrator is introduced. This setup is relevant to the present master thesis, since this work aims to design a similar setup, at least in terms of size. Finally, several large-scale demonstrators are discussed, approaching real full-scale tiltrotor aircraft systems.

2.3.1 Bland and Bennett model

In 1963, Bennett and Bland created one of the first experimental setups fully dedicated to the study of whirl flutter. The objective of this setup was to validate existing analytical methods for whirl flutter prediction. They also aimed to highlight the influence of the wing on whirl flutter stability [25]. Pictures of both experimental rigs, with and without wing, are shown in Figure 2.7.

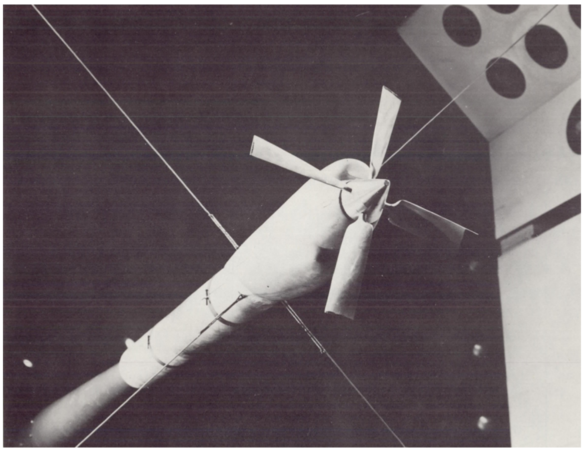

(a) Bland and Bennett whirl flutter test rig without cantilever wing in the Langley wind tunnel [17].

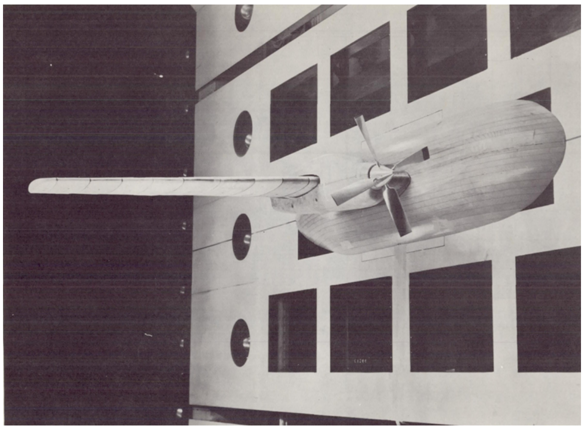

(b) Bland and Bennett whirl flutter test rig mounted on a semi-span cantilever wing in the Langley wind tunnel [17].

Figure 2.7: Both experimental setups of Bland and Bennett, with and without cantilever wing, in the Langley transonic dynamics tunnel [25].

This setup was a 1/8-scale model and two different propeller shaft lengths were tested. The propeller is mounted on a steel beam through a gimbal, and the engine was represented by a simulated engine mass, since the propeller was operating in windmilling mode.

The pitch and yaw degrees of freedom were enabled by the gimbal. The model was restrained in pitch and yaw by steel springs, which provided equal stiffnesses in both directions. The setup was equipped with a nacelle cover, enclosing the gimbal, the propeller shaft, and the simulated engine mass.

As shown in Figure 2.7, the propeller had four identical aluminium blades. In order to measure the angular accelerations about the gimbal axis, linear accelerometers were mounted on the simulated engine mass. This measurement setup is depicted in Figure 2.8, where the nacelle cover is removed.

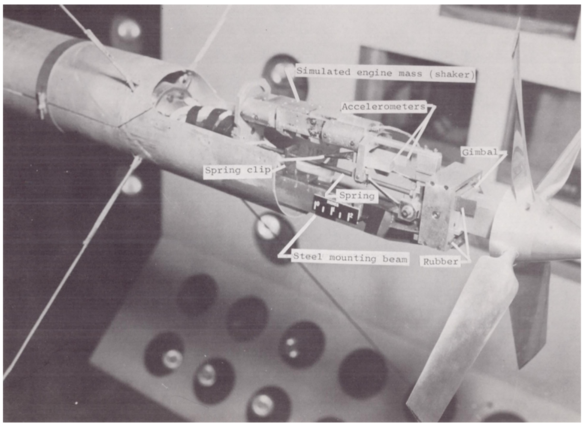

Figure 2.8: Representation of the measurement technique of the Bland and Bennett experimental test rig in the Langley test tunnel, for which the nacelle cover is removed, allowing the view of the springs, accelerometers, simulated engine mass and steel beam [25].

All the tests were performed at Mach number below 0.25 and under atmospheric pressure. The measured whirl flutter speeds and frequencies appeared to be close to the predicted values of the two-degrees-of-freedom model presented in Section 2.2.1. Additionally, for the considered configuration, the semi-span wing did not significantly change the whirl flutter boundaries [25].

2.3.2 W-WING demonstrator

Initially developed in 2014 for two experimental campaigns, the W-WING demonstrator regained attention for whirl flutter experimental studies in 2022, when J. Cecrdle et al. modified and upgraded it in the scope of the OFELIA project [26, 27]. This test rig allows several important parameters influencing whirl flutter stability to be varied, which makes it relevant for research activities. A representation of this aeroelastic demonstrator is shown in Figure 2.9.

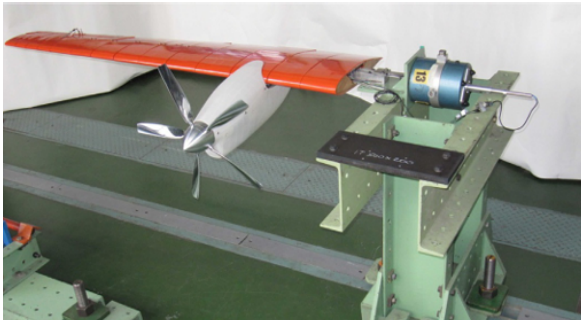

(a) With the cover [26].

(b) Without the cover [28].

Figure 2.9: W-WING demonstrator before being modified by Cecrdle et al., shown with and without the cover [26, 28].

This model is based on a 40-passengers commuter aircraft, but it is not fully representative due to structural modifications. Its main parameters are listed in Table 2.1. The total mass of 55 kg includes a simulated fuel weight. Duralumin spars with several cross-sections are used to build the wing and to define the aileron stiffnesses. The system is covered by several plastic covering segments in order to reproduce the aerodynamic shape of the model.

The pylon has two degrees of freedom, corresponding to yaw and pitch motions, and their stiffnesses are represented by cross-spring pivots. Additionally, the engine inertia is modelled by movable masses, whereas the wing dynamics can be modified through adjustable masses in order to simulate fuel weight variations. Furthermore, the setup includes two different blade sets: one with duralumin blades and one with steel blades [26].

Parameter	Value
Half-wing span	2.56 m
Wing weight	30 kg
Nacelle weight	25 kg
Propeller diameter	0.7 m
Number of blades	5

Table 2.1: Main parameters of the W-WING whirl flutter demonstrator [26].

In the scope of the OFELIA project, the motor was replaced in order to allow operation under non-zero thrust conditions. As another example of the modifications, the connection between the propeller and the motor was also redesigned.

2.3.3 Small-scale demonstrator

This small-scale whirl flutter demonstrator, presented at the International Forum on Aeroelasticity and Structural Dynamics (IFASD) in Madrid in 2022, was developed by three engineers from the University of Naples Federico II. It uses a multi-bladed windmilling propeller, and aims to identify the pitch and yaw mode shapes when the propeller is at rest, as well as to verify the role of propeller rotation in the emergence of whirl flutter. This rig exists in two versions: one with a two-bladed propeller, and another one with a five-bladed propeller [29]. Representations of both versions are shown in Figure 2.10.

(a) Two-bladed propeller [29].

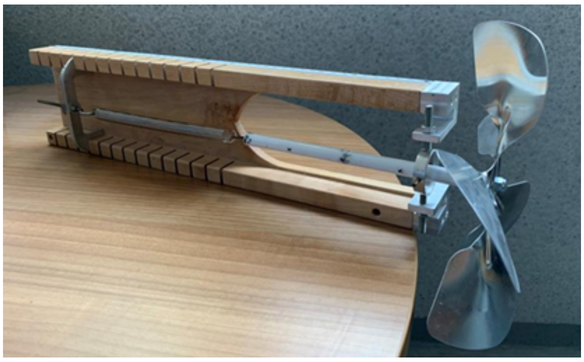

(b) Five-bladed propeller [29].

Figure 2.10: Both two- and five-bladed propellers mounted on the small-scale test rig [29].

The propeller is connected to the shaft through bearings, and the shaft is assumed to represent the inertia of the engine-nacelle system. Pitch and yaw motions are allowed by the use of a Cardan joint, while the associated stiffnesses are introduced by connecting the shaft to a spring. These stiffnesses can be varied by modifying the position of the aluminium plate. The spring can also be replaced in order to adjust the stiffnesses. Additionally, both propeller diameters are equal to 0.25 m.

The experimental results showed a good agreement with the analytical and numerical predictions. In particular, when several parameters of the setup were varied, the obtained whirl flutter stability boundaries remained consistent with the predicted trends [29].

2.3.4 NASA tiltrotor test rig (TTR)

Developed by NASA, the U.S. Army and the U.S. Air Force between 2007 and 2015, the NASA tiltrotor test rig (TTR) is a recent large-scale tiltrotor test system involved in aeroelastic studies at the National Full-Scale Aerodynamic Complex (NFAC). An experimental campaign started in March 2017. This experimental rig aims to acquire data from large-scale experiments under full NFAC operational conditions, with speeds up to 555 km/h [30]. A picture of this test rig in the NFAC wind tunnel is shown in Figure 2.11.

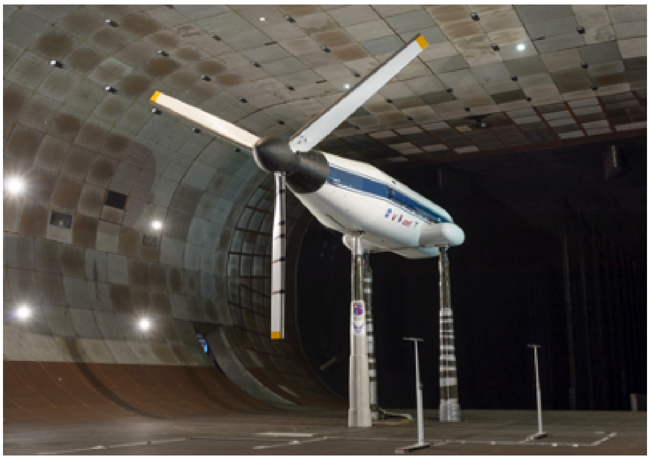

Figure 2.11: NASA tiltrotor test rig (TTR) in the NFAC wind tunnel facilities [30].

The model was tested up to 555 km/h in axial flight conditions, while the velocity was increased up to 333 km/h for the tiltrotor conversion mode. The main characteristics of this large-scale experimental setup are listed in Table 2.2.

Parameter	Value
Total weight	27578.4 kg
Maximum rotor shaft speed	629.5 rpm
Rotor diameter	7.92 m
Total length	11 m
Continuous power during two hours	3.73 MW
Width (excluding vertical pylons)	2.16 m

Table 2.2: Main parameters of the NASA tiltrotor test rig (TTR) [30].

This is the first rig of such a size used for high-speed experimental analysis. It enabled the acquisition of a large set of aerodynamic and aeroelastic data, allowing further stability studies for similar models.

2.3.5 Tiltrotor aeroelastic stability testbed (TRAST)

This tiltrotor whirl flutter stability testbed was developed by the U.S. Army and NASA and was tested for the first time in 2021 in the NASA Langley transonic dynamics tunnel facilities [31]. A picture of this test rig is shown in Figure 2.12.

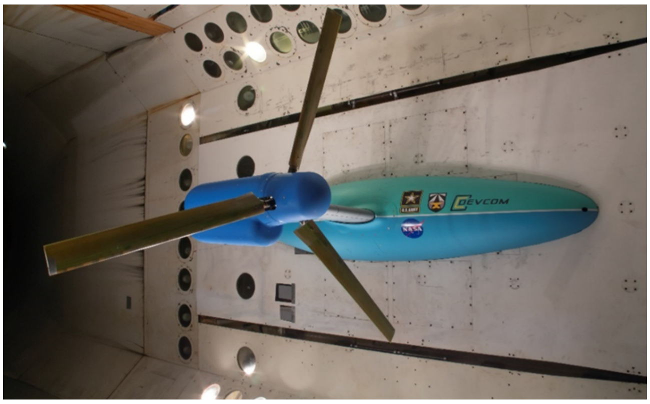

Figure 2.12: Tiltrotor aeroelastic stability testbed (TRAST) in the NASA Langley transonic dynamics tunnel facilities [32].

The objective of this experimental setup was to study the whirl flutter behaviour and stability of a tiltrotor aircraft. The rig consists of a rigid fuselage attached to a semi-span wing, on which a pylon-propeller system is mounted. The rotor is representative of a classical tiltrotor, for which several parameters and stiffnesses can be varied in order to adapt the rig to new tiltrotor designs and configurations. For example, springs, tuning masses, and interchangeable hubs can be modified in order to represent the desired configuration [32].

Two thrust configurations were tested in the wind tunnel. First, the motor was used to prescribe the rotational speed of the tiltrotor. Then, the rig was tested in the windmilling configuration, which is the most conservative arrangement for whirl flutter experimental tests because it provides the lowest stability margin [32].

In 2023, a second experimental campaign took place in order to quantify the influence of pitch-flap coupling on whirl flutter stability for tiltrotors. Blade stiffness was also analysed, as well as several spring stiffnesses. During these tests, the tiltrotor rotational speeds ranged from 727 rpm to 909 rpm [31]. Table 2.3 lists the main parameters of the tiltrotor aeroelastic stability testbed.

Parameter	Value
Tiltrotor diameter	2.44 m
Tiltrotor mass	2.84 kg
Maximum thrust	836 N
Wing length	1.34 m
Wing chord	0.46 m

Table 2.3: Main parameters of the tiltrotor aeroelastic stability testbed (TRAST) [32].

2.3.6 Advanced testbed for tiltrotor aeroelastics (ATTILA)

The ATTILA demonstrator is a European testbed mainly conducted by the Royal Netherlands Aerospace Centre. It is a Froude-scale model, meaning that the Froude number is preserved between the model and the full-scale prototype [33, 34].

This setup aims to demonstrate the validity of numerical methods used to obtain approval for high-speed flight testing of the Leonardo next-generation civil tiltrotor technology demonstrator.

The ATTILA testbed is illustrated in Figure 2.13. It consists of a three-bladed gimballed rotor mounted on a half-span cantilever wing. Additionally, the rotor rotates at a constant speed during the test campaign.

Figure 2.13: ATTILA demonstrator in the German-Dutch wind tunnel large low-speed facility (DNW LLF) 6x6m test section [34].

Furthermore, Table 2.4 summarizes the key parameters of this half-span wing whirl flutter model.

Parameter	Value
Number of blades	3
Diameter	2.5 m
Wing span	1.6 m

Table 2.4: Key parameters of the advanced testbed for tiltrotor aeroelastics (ATTILA) [34].

This demonstrator was built in order to characterize several critical modes that drive whirl

flutter instability, such as the pylon pitch and yaw modes, as well as the wing torsion, bending and chord modes. Moreover, the demonstrator is equipped with several leaf springs allowing the pitch and yaw pylon stiffnesses to be varied. This highlights the importance of both parameters for whirl flutter stability analysis.
The testbed also features a specific excitation system. The pitch angle of the blades can be periodically varied using linear sine sweeps and sine dwell signals in order to target a given dynamic mode [34].

Besides, the results show that the critical mode, i.e. the first mode to become unstable, depends on the tested configuration. For example, the pylon stiffness and the rotor power have a strong influence. The tests also revealed a non-negligible amplitude-dependent nonlinearity, corresponding to higher structural damping at low excitation levels. The nature of these nonlinearities has not been fully studied. Therefore, discrepancies with analytical predictions can emerge from this type of nonlinearity [34].

2.4 Existing numerical methods

Even if it is not the main objective of the present work, it is useful to be aware of the existing numerical methods used to predict the whirl flutter behaviour of a system, since they play a major role in current applications. The two methods presented in Sections 2.4.1 and 2.4.2 are multibody dynamics and the finite element method, respectively. Both methods are used to describe the structural and mechanical behaviour of the system, and they have to be coupled with an aerodynamic model in order to predict the complete aeroelastic response.

2.4.1 Multibody dynamics (MBD)

Multibody dynamics can be used to describe rotating rotor systems. This approach enables the behaviour of a system composed of several bodies connected by joints to be predicted. These joints restrict the relative motion between the bodies [35, 36]. The different bodies of the system can either be rigid or flexible, and several types of joints exist. Each of them corresponds to a specific kinematic constraint between two bodies [35].
The equations of motion are solved based on the mass, centre of mass, inertia tensor of each body, as well as interaction forces existing between the bodies. Additionally, forces from springs, dampers, friction, gravity, and external loads, such as aerodynamic forces, can be taken into account.
Initial conditions in velocity or position can also be considered. As outputs, the MBD analysis provides the reaction forces between the different parts of the system, as well as the motion of the bodies [36].

Moreover, due to the complexity associated with the computation of the constraint forces imposed by the joints, a specific formulation of the equations of motion is required for a multibody simulation. This can be achieved through several methods, such as discrete Euler-Lagrange formulation or recursive methods [35].

2.4.2 Finite element method (FEM)

The finite element method divides the structure into several small elements through a meshing process. Different types of elements exist, with different numbers of degrees of freedom, and they are connected to each other through specific points called nodes. Therefore, this method transforms a continuous model into a discrete one, leading to equations of motion written in matrix form [36]. It allows large deformations, as well as material and geometric nonlinearities to be taken into account, and can be used to perform modal analysis [37].
As an application, the Simcenter 3D solver of the Siemens NX is able to model cyclically symmetric rotating structures using the finite element method. In that case, the problem is solved using the Coleman transformation in order to obtain time-independent matrices in the fixed frame. This formulation can then be used to obtain, for example, Campbell diagrams, damping diagrams, critical speeds, and the oscillation frequencies of the system [38].

2.4.3 Finite element-based multibody dynamics codes

Both numerical methods can be coupled in finite-element-based multibody dynamics codes, such as Dymore, enabling the study of nonlinear flexible multibody systems [39].
Furthermore, the comprehensive analytical model of rotorcraft aerodynamics and dynamics (CAMRAD) II is an aeromechanics rotorcraft analysis code that allows the true geometry of the rotorcraft to be modelled. It combines several advanced modelling approaches, such as multibody dynamics, nonlinear finite elements and rotorcraft aerodynamics [40].

Another code of this type is the rotorcraft comprehensive analysis system (RCAS), which has an aerodynamic model comparable to that of CAMRAD II. It allows rotorcraft aerodynamics, performance, vibration, aeroelastic stability and control to be predicted. Several operating conditions, such as forward flight and hover, can be modelled, and this code relies on a finite element multibody dynamics approach to model rotor-body structures. In RCAS, the equations of motion are solved through direct integration in the time domain [40].

2.5 Conclusion

In conclusion, the experimental setups presented in this Section demonstrate the possibility of studying whirl flutter at different scales. Although they differ in terms of dimensions, objectives, and complexity, they all provide valuable insights into the physical mechanisms governing this aeroelastic instability.

In this context, the present work focuses on the preliminary design of a small-scale whirl flutter demonstrator. The objective is to provide an experimental setup that could be used to support the verification of a finite element-based numerical method currently under development at the University of Liège [12].

Chapter 3. Methodology

In this chapter, the methodology used to obtain the analytical results presented in Chapter 4 is described. First, the analytical method used to derive the equations of motion of the system is introduced. Then, the required transformation of the equations of motion to perform a classical eigenvalue analysis is explained. Finally, the methods used for post-processing the eigenvalues, i.e. whirl flutter mode identification and mode tracking, are presented. Additional theoretical concepts used for the interpretation of the results are also described.

3.1 Analytical method for flexible-blade propellers

The analytical model chosen to compute the dynamic behaviour of the system is taken from the thesis of Vincent de Gaudemaris [14]. It allows blade flexibility to be integrated in the equations of motion, in order to obtain a more realistic representation of the physical system. The main features and advantages of the method are presented in this section. The details of the mathematical developments are provided in its thesis, but are not repeated here. Moreover, the method was validated by its author through a comparison with the W-WING experimental case, which is presented in Section 2.3.2.

The selected analytical model considers a flexible-blade propeller using a quasi-steady aerodynamic model. Considering flexible blades is a realistic choice, even if they are much stiffer than the pylon. The thesis of V. de Gaudemaris states that blade flexibility significantly stabilizes the system, even for stiff blades, i.e. when the blade bending frequency is higher than four times the propeller rotational speed. Hence, assuming rigid blades could not be valid, even if the blades appear to be considerably stiff.

According to Vincent de Gaudemaris, the stabilizing influence of blade flexibility appears to be mainly driven by aerodynamic effects, rather than structural ones. Effectively, when the aerodynamic matrices are replaced by those of the rigid-blade case, while keeping the flexible-blade aerodynamic matrices, the whirl flutter stability boundaries remain very close to the case of a rigid-blade propeller. This suggests that the considered blade deformation produces negligible structural dynamic effects, while the associated variations in aerodynamic forces are sufficient to significantly stabilize the system.

Furthermore, the use of a quasi-steady aerodynamic model is a strong assumption. Nevertheless, this is still acceptable for the preliminary design of an experimental setup. Significant differences between the whirl flutter stability boundaries obtained with quasi-steady and unsteady aerodynamic models mainly appear for high values of pitch and yaw stiffness [14].

Main assumptions of the model, as well as the derivation of the analytical matrices are described in the next sections.

3.1.1 Method assumptions

This method of course relies on several approximations. This section lists all the assumptions taken into account by the analytical model.

The most straightforward assumption is to consider a propeller with identical blades, whose blades are made of a homogeneous material and equally distributed around the hub. This is not a restrictive assumption since it is the case for most of the conventional propellers.

Moreover, these blades are approximated as straight beams of variable cross-sections. The geometrical characteristics of the beams depend on whether the structural model or the aerodynamic model is considered. For the latter, blade element theory and blade element momentum theory respectively described in Sections 3.2.1 and 3.2.2 are used, and the twist of the blades is taken into account. For the aerodynamic matrices, the blade cross-section corresponds to the actual airfoil geometry.
In contrast, the beams are considered as untwisted for the structural mechanical model. This assumption allows for the in-plane and out-of-plane bending to be fully decoupled. Besides, the cross-sections are assumed rectangular, allowing the centre of gravity, as well as the geometrical centre to be on the elastic axis. The dimensions of the rectangular blades are defined by the geometry of the actual blades. In particular, the beams have variable cross-sections over the radius. For instance, the width and the thickness of the beam at one radial location are defined as the maximum thickness t and the chord c of the actual blade geometry at this location, respectively.
Figure 3.1 represents a drawing of the beam shape used for deriving the structural matrices, whereas the aerodynamic shape model corresponds to the actual airfoil profile of the tested propeller, defined in Section 4.1.1.

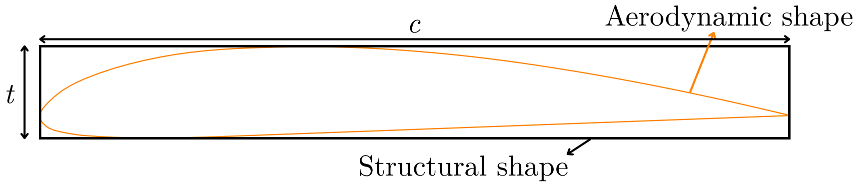

Figure 3.1: Beam approximation used to derive the structural matrices with t the maximum thickness and c the chord of the section, and the aerodynamic shape used in the BET and BEMT methods, adapted from the thesis [14].

Furthermore, the Euler-Bernoulli beam assumption is made. This approximation assumes that the beam cross-sections remain plane, rigid in their own plane and perpendicular to the elastic axis. In

general, using this beam theory minimizes the deflections, and the natural frequencies are overstated, because the effects of transverse shear deformation and rotary inertia are neglected [41]. This includes both small-displacement and small-rotation approximations. This means that the method only predicts linearly the onset of the instability, as the displacements and rotations cannot be considered as small once the instability is established.
Additionally, the shear centres of the blade sections define the elastic axis and are assumed to be located at the quarter chord of the blade profile. Moreover, the aerodynamic forces on the pylon are neglected, as well as the aerodynamic interaction between the pylon and the propeller. Besides, the connection between the pylon and the propeller is considered rigid.

3.1.2 Definition of the reference frames

Since the considered system involves rotating components and deformable blades, several reference frames must be defined.

The first frame, called the reference frame, has its origin O on an arbitrary point of the structure. It is fixed, and the equations of motion are written in this frame. Its mathematical formulation is given by:

$$R_1 = (O, \mathbf{x}_1, \mathbf{y}_1, \mathbf{z}_1) \,. \tag{3.1}$$

The second one is a moving frame whose origin is located at the propeller centre, denoted as C. It is used to describe the motion of the propeller centre induced by the pylon, as well as to visualize the blade deformations, as explained in Section 3.7. Its mathematical form is defined as follows:

$$R_2 = (C, \mathbf{x}_2, \mathbf{y}_2, \mathbf{z}_2) \,. \tag{3.2}$$

Figure 3.2 represents both frames R_1 and R_2 on a three-bladed propeller-pylon system.

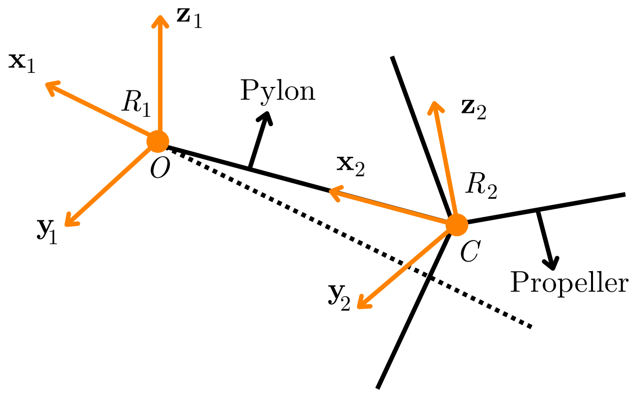

Figure 3.2: Representation of frames R_1 (fixed, with origin at an arbitrary point O of the structure) and R_2 (moving, centred at the propeller centre) on a three-bladed propeller-pylon system, adapted from the thesis [14].

Then, the frames associated with the blades can be defined. First, a rotating frame is associated with each undeformed blade, so that each blade has its own rotating frame. The origin of this frame is at the propeller centre C. Mathematically, it is written as:

$$R_{b_n} = (C, \mathbf{x}_{b_n}, \mathbf{y}_{b_n}, \mathbf{z}_{b_n}) . \tag{3.3}$$

Therefore, following the elastic axis assumptions defined in Section 3.1.1, the coordinates in the R_{b_n} frame of a point located on this axis at a distance r_P from the blade root are defined as $(0, r_P, 0)$.

Finally, a deformed frame is attached to each blade to describe its deformation. Its origin is located at an arbitrary point P' of the blade, associated with the point P previously defined in R_{b_n}. Mathematically, it comes:

$$\bar{R}_{b_n} = (P', \bar{\mathbf{x}}_{b_n}, \bar{\mathbf{y}}_{b_n}, \bar{\mathbf{z}}_{b_n}) . \tag{3.4}$$

These frames are represented on a blade model in Figure 3.4.

3.1.3 Background and principles of the analytical method

The entire analytical method is initially based on the principle of virtual power. Specifically, the equations of motion are derived from this principle.

Theoretically, the principle of virtual power is closely related to the principle of virtual work. Both rely on a similar variational formulation, the main difference being the use of a virtual velocity field instead of a virtual displacement field for the principle of virtual work [42]. According to this principle, for any virtual velocity field $\hat{\mathbf{y}}$, the sum of the virtual power of the internal and external forces, respectively

P_{int} and P_{ext}, is equal to the virtual power of the acceleration of the solid, denoted P_A. Mathematically, it comes [14]:

$$P_A\left(\hat{\mathbf{y}}\right) \;=\; P_{int}\left(\hat{\mathbf{y}}\right) \;+\; P_{ext}\left(\hat{\mathbf{y}}\right) \tag{3.5}$$

for any kinematically admissible virtual velocity field $\hat{\mathbf{y}}$.

Therefore, all these virtual powers are computed separately by distinguishing the contributions of the propeller and of the supporting structure, i.e. the pylon. They are derived with respect to the propeller-centre degrees of freedom, which are written in R_1 as:

$$\mathbf{u}_c \;=\; \begin{pmatrix} u_c^x \\ u_c^y \\ u_c^z \end{pmatrix} \qquad \text{and} \qquad \boldsymbol{\theta}_c \;=\; \begin{pmatrix} \varphi \\ \theta \\ \psi \end{pmatrix} \tag{3.6}$$

with u_c^x, u_c^y and u_c^z the translations of the propeller centre in the $\mathbf{x}_1-$, $\mathbf{y}_1-$ and $\mathbf{z}_1-$directions, respectively, and φ, θ and ψ the roll, pitch and yaw rotation angles of the propeller centre. Vector $\mathbf{u}_c$ represents the translation of the propeller plane, while vector $\boldsymbol{\theta}_c$ characterizes the change in orientation of the propeller plane.

Then, the three virtual powers are combined through Equation 3.5 to obtain the equations of motion. The virtual power formulation is established with respect to the R_1 frame, defined in Equation 3.1. Therefore, the equations are first derived from a virtual velocity field expressed with respect to R_1, before being projected onto the generalized coordinates. After this projection, the resulting matrix equations are no longer expressed in a purely geometrical frame, but in the generalized coordinate space associated with the system degrees of freedom.

As several matrices depend on the degrees of freedom, the obtained equations must be linearized around an equilibrium position with respect to the generalized coordinates, in order to use a classical linear resolution method. This position corresponds to the static deformation of the pylon-propeller system around which the vibrations occur. Therefore, this is not valid for large deformations, but it is still acceptable at the beginning of the whirl flutter instability, where the displacements and rotations are small [14].

All the details of the virtual power formulations are not repeated here, and are available in the thesis of Vincent de Gaudemaris [14].

Once the system matrices are written with respect to these coordinates, a coordinate change is performed, because these six generalized coordinates are not the actual degrees of freedom of the system considered in this work. Here, only the pitch θ and yaw ψ motions of the propeller centre are kept. Both retained degrees of freedom will be related to the initial six generalized coordinates in order to form the change-of-coordinates matrix.

3.1.4 Problem definition

The propeller of radius R_p, in rotation at a rotational speed Ω, is rigidly mounted on a pylon of length L_{pylon}. The pylon is supposed to be rigid, whereas the pitch and yaw motions are possible through the use of two torsion springs of stiffnesses K_θ and K_ψ. Two viscous dampers of damping coefficients C_θ and C_ψ are also added at the base of the pylon. This model provides a simplified but efficient representation of a propeller-pylon system mounted on a rigid wing, in which the pylon flexibility is modelled through equivalent pitch and yaw torsional springs.

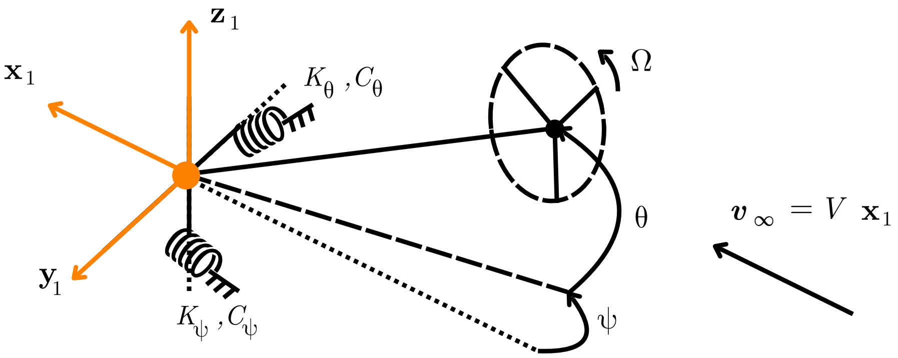

Figure 3.3: Analytical model used for the derivation of the equations of motion, consisting of a rigid pylon mounted on two rotational stiffnesses K_θ and K_ψ and dampers of coefficients C_θ and C_ψ, and with its tip attached to the propeller, adapted from the thesis [14].

The blades are supposed to be clamped at a distance r_0 from the propeller hub. Therefore, they have a length L equal to $L = R_p - r_0$. This is shown in Figure 3.4, where a blade is represented in both the deformed and the undeformed frames.

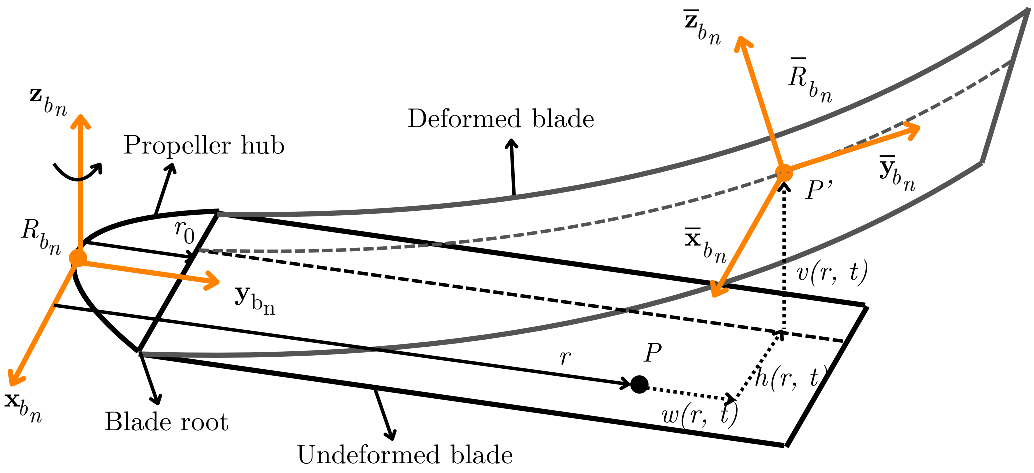

Figure 3.4: Representation of both frames associated with each blade: the undeformed frame R_{b_n}, centred at the propeller hub, and the deformed frame $\bar{R}_{b_n}$, whose origin is located at an arbitrary point P' of the deformed elastic axis. The blade model used to derive the equations of motion is shown without thickness for clarity. Adapted from the thesis [14]

The considered blade deformations are denoted h, w, v and θ_t referring to in-plane bending, traction, out-of-plane bending and torsion, respectively. In this approach, they are approximated using the Rayleigh-Ritz method, for which the shape functions must be kinematically admissible, i.e. they must respect the boundary conditions.

The Rayleigh-Ritz method is an improvement of the classical Rayleigh's method, for which the computation of only one natural frequency is possible. The Rayleigh-Ritz method allows the calculation of the higher natural frequencies. Following the definition of Ilanko et al., Rayleigh-Ritz method is widely used in continuous system applications for which the displacement distribution $f(x)$ is approximated as a sum of products between undetermined weighting coefficients and admissible displacement functions. In this work, these weighting coefficients are called the generalized coordinates, while the admissible displacements functions are named the shape functions [43].

Therefore, boundary conditions must be defined to be able to select admissible displacement shape functions. Since the blades are clamped on the propeller hub, they are approximated as cantilever beams. Therefore, the following boundary conditions are imposed:

$$h\left(r=r_0\right)=w\left(r=r_0\right)=v\left(r=r_0\right)=0 \tag{3.7}$$

for the displacements. Based on the small displacements assumption, stating that the rotation of the beam section can be approximated by the slope of the deflection curve, the rotation boundary conditions are

$$\theta_h\left(r=r_0\right)=\left.\frac{\partial h}{\partial r}\right|_{r=r_0}=\theta_v\left(r=r_0\right)=\left.\frac{\partial v}{\partial r}\right|_{r=r_0}=\theta_t\left(r=r_0\right)=0, \tag{3.8}$$

with θ_t the beam torsion angle.

A classical polynomial shape function ξ_i that satisfies these boundary conditions is either

$$\xi_i = \left(\frac{r - r_0}{R_p - r_0}\right)^i \qquad \text{or} \qquad \xi_i = \left(\frac{r - r_0}{R_p - r_0}\right)^{i+1}, \tag{3.9}$$

depending on the considered deformation. These functions vanish at the blade root, and, when required by rotation boundary conditions, their derivatives also vanish at the root.

Therefore, blade deformation distributions over the blade radius are given by:

$$h\left(r,t\right)=\sum_{i=1}^{N_h}\xi^{i+1}q_h^{(i)}(t)=\sum_{i=0}^{N_h}\left(\frac{r-r_0}{R_p-r_0}\right)^{i+1}q_h^{(i)}(t) \tag{3.10}$$

$$w\left(r,t\right)=\sum_{i=1}^{N_w}\xi^{i}q_w^{(i)}(t)=\sum_{i=0}^{N_w}\left(\frac{r-r_0}{R_p-r_0}\right)^{i}q_w^{i}(t) \tag{3.11}$$

$$v\left(r,t\right)=\sum_{i=1}^{N_v}\xi^{i+1}q_v^{(i)}(t)=\sum_{i=0}^{N_v}\left(\frac{r-r_0}{R_p-r_0}\right)^{i+1}q_v^{(i)}(t) \tag{3.12}$$

$$\theta_t\left(r,t\right)=\sum_{i=1}^{N_t}\xi^{i}q_t^{(i)}(t)=\sum_{i=0}^{N_t}\left(\frac{r-r_0}{R_p-r_0}\right)^{i}q_t^{(i)}(t) \tag{3.13}$$

where

- N_h, N_w, N_v and N_t are the number of shape functions used in the approximation of in-plane bending, traction out-of-plane bending and torsion, respectively. In other words, it is the approximation orders,
- $q_h^{(i)}$, $q_w^{(i)}$, $q_v^{(i)}$ and $q_t^{(i)}$ represent the generalized coordinates associated with in-plane bending, traction, out-of-plane bending and torsion, respectively.

In a matrix form expressed in R_{b_n}, this gives:

$$\mathbf{u}_n=\begin{pmatrix}h(r,t)\\ w(r,t)\\ v(r,t)\end{pmatrix}=\mathbf{\Phi}(r)\ \mathbf{q}_n(t) \qquad \text{and} \qquad \theta_t(r,t)=\mathbf{\Phi}_t(r)\ \mathbf{t}_n(t) \tag{3.14}$$

where $\mathbf{q}_n(t) = \left(q_{h,n}^{(1)},\ \ldots,\ q_{h,n}^{(N_h)}, q_{w,n}^{(1)},\ \ldots,\ q_{w,n}^{(N_w)},\ q_{v,n}^{(1)}, \ldots q_{v,n}^{(N_v)}\right)$ is the vector gathering all the generalized coordinates of blade n, except those associated with torsion and $\mathbf{t_n} = \left(q_{t,n}^{(1)},\ \ldots,\ q_{t,n}{}^{(N_t)}\right)$

contains all the torsional generalized coordinates of the n^{th} blade. The matrix $\mathbf{\Phi}$ gathers the shape functions associated with bending and traction, while torsion is described separately by $\mathbf{\Phi}_t$. Therefore, matrix $\mathbf{\Phi}$ is written as:

$$\begin{pmatrix} \mathbf{\Phi}_h & 0 & 0 \\ 0 & \mathbf{\Phi}_w & 0 \\ 0 & 0 & \mathbf{\Phi}_v \end{pmatrix}. \tag{3.15}$$

A similar notation is used for the torsional shape-function matrix $\mathbf{\Phi}_t$.

Additionally, the generalized coordinates are gathered in the vector $\mathbf{y}_c$, which is given by:

$$\mathbf{y}_c \;=\; \left(\mathbf{q}_1^T \; \mathbf{t}_1^T \; \ldots \; \mathbf{q}_N^T \; \mathbf{t}_N^T \; \mathbf{u}_c^T \; \boldsymbol{\theta}_c^T\right)^T. \tag{3.16}$$

As a reminder, the blade deformation coordinates $\mathbf{q}_n$ and $\mathbf{t}_n$ are associated with deformation fields expressed in the rotating blade frame R_{b_n}, while $\mathbf{u}_c$ and $\boldsymbol{\theta}_c$ describe the motion of the propeller centre with respect to R_1.

When deriving the structural matrices in the next sections, these shape functions are integrated over the entire blade length L. To this end, a change of variable can be defined in order to resolve the integrals. Defining $\xi = \frac{r-r_0}{R_p-r_0}$ as the new variable, the new integration domain can be defined. At the blade root, $r = r_0$ and $\xi = 0$, while at the tip of the blade $r = R$ and $\xi = 1$. Thus, it comes:

$$\int_{r_0}^{R_p} \left(\frac{r-r_0}{R_p-r_0}\right)^i dr = L\int_0^1 \xi^i \, d\xi \qquad \text{since} \qquad dr = \frac{d\xi}{R_p-r_0} = \frac{d\xi}{L}. \tag{3.17}$$

3.1.5 Definition of the rotation matrices

Since several frames are used, transfer matrices, also called rotation matrices, are defined to transform vector components from one frame to another. First, the rotation matrix is introduced in a general form and is then specialized to the present analytical model.

The developments below, taken from the work of Goldstein et al., are made under the small displacements and rotations assumptions [44].

Assuming $\mathbf{x}$ the undeformed vector and $\mathbf{x}'$ the deformed vector, the rotation matrix is given by:

$$\mathbf{R} = \mathbf{1} + \boldsymbol{\varepsilon} \qquad \text{because} \qquad \mathbf{x}' = (\mathbf{1} + \boldsymbol{\varepsilon})\; \mathbf{x} = \underbrace{\mathbf{1}\;\mathbf{x}}_{\mathbf{x}} + \boldsymbol{\varepsilon}\;\mathbf{x} = \mathbf{R}\;\mathbf{x}. \tag{3.18}$$

Matrix $\boldsymbol{\varepsilon}$ is called the infinitesimal rotation matrix and is given by:

$$\boldsymbol{\varepsilon} = \begin{pmatrix} 0 & d\Omega_3 & -d\Omega_2 \\ -d\Omega_3 & 0 & d\Omega_1 \\ d\Omega_2 & -d\Omega_1 & 0 \end{pmatrix} \tag{3.19}$$

where $d\Omega_1$, $d\Omega_2$, and $d\Omega_3$ are rotations around axis $\mathbf{m}_1$, $\mathbf{m}_2$ and $\mathbf{m_3}$, respectively. A generic rectangular body with these axes is represented in Figure 3.5.

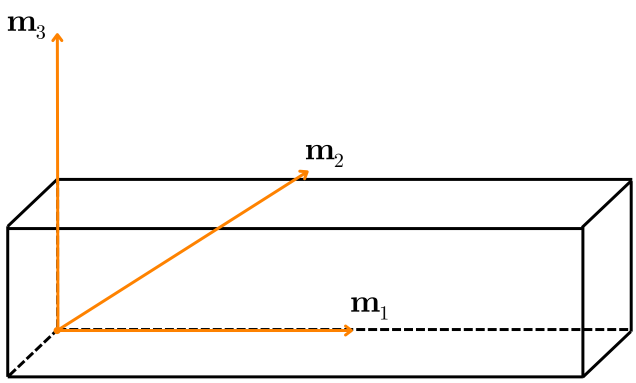

Figure 3.5: Generic body with its axes used for the definition of the general form of the rotation matrix, adapted from [44].

Two important properties of the rotation matrix are the inverse matrix property such as $\mathbf{R}\mathbf{R}^{-1} = \mathbf{I}$, as well as $\mathbf{R}^{-1} = \mathbf{R}^T$, leading to $\mathbf{R}\mathbf{R}^T = \mathbf{I}$ [45].

The objective is to build the transfer matrix between the frames defined in Section 3.1.2. First, the matrix expressing vector components from the undeformed blade frame to the deformed one is derived. Working in the undeformed blade frame R_{b_n} defined in Equation 3.3, $\mathbf{m}_1$, $\mathbf{m}_2$ and $\mathbf{m}_3$ of Figure 3.5 can be identified as $\mathbf{x}_{b_n}$, $\mathbf{y}_{b_n}$ and $\mathbf{z}_{b_n}$, respectively.
Therefore, $d\Omega_1$ corresponds to a rotation around $\mathbf{x}_{b_n}$, $d\Omega_2$ to a rotation around $\mathbf{y}_{b_n}$, and, finally, $d\Omega_3$ to a rotation around $\mathbf{z}_{b_n}$.

Under the small displacements and rotations assumptions, a rotation around $\mathbf{x}_{b_n}$ equals $\frac{\partial v}{\partial r} = \partial_r v$, while a rotation around $\mathbf{z}_{b_n}$ corresponds to $\frac{\partial h}{\partial r} = \partial_r h$. For the rotation around $\mathbf{y}_{b_n}$, it simply corresponds to the torsion angle θ_t. Following this, the rotation matrix between the undeformed R_{b_n}

and the deformed $\bar{R}_{b_n}$ frames becomes:

$$\mathbf{R}_{R_{b_n}\to\bar{R}_{b_n}} = \begin{pmatrix} 1 & -\partial_r h & -\theta_t \\ \partial_r h & 1 & \partial_r v \\ \theta_t & -\partial_r v & 1 \end{pmatrix}. \tag{3.20}$$

According to the inverse property of rotation matrices, the rotation matrix from the deformed frame to the undeformed one is written as:

$$\mathbf{R}_{\bar{R}_{b_n}\to R_{b_n}} = \mathbf{R}^T_{R_{b_n}\to\bar{R}_{b_n}} = \begin{pmatrix} 1 & \partial_r h & \theta_t \\ -\partial_r h & 1 & -\partial_r v \\ -\theta_t & \partial_r v & 1 \end{pmatrix}. \tag{3.21}$$

Therefore, to express a vector $\mathbf{x}$ from the undeformed frame R_{b_n} to the deformed one $\bar{R}_{b_n}$, and inversely, it comes:

$$\mathbf{R}_{R_{b_n}\to\bar{R}_{b_n}}\ \mathbf{x} = \mathbf{x} + \mathbf{\Lambda_x} \begin{pmatrix} \partial_r v \\ \theta_t \\ -\partial_r h \end{pmatrix} \qquad \text{and} \qquad \mathbf{R}_{\bar{R}_{b_n}\to R_{b_n}}\ \mathbf{x} = \mathbf{x} - \mathbf{\Lambda_x} \begin{pmatrix} \partial_r v \\ \theta_t \\ -\partial_r h \end{pmatrix}, \tag{3.22}$$

with $\mathbf{\Lambda_x}$ a matrix operator relative to an arbitrary vector $\mathbf{x} = (x_1,\ x_2,\ x_3)$ defined as:

$$\mathbf{\Lambda_x} = \begin{pmatrix} 0 & -x_3 & x_2 \\ x_3 & 0 & -x_1 \\ -x_2 & x_1 & 0 \end{pmatrix}. \tag{3.23}$$

Similarly, the matrix expressing vectors of frame R_2 in frame R_1 can be derived starting from the definition of rotation matrix of Equations 3.18 and 3.19 such as:

$$\mathbf{R}_{R_2\to R_1} = \begin{pmatrix} 1 & -\psi & \theta \\ \psi & 1 & -\varphi \\ -\theta & \varphi & 1 \end{pmatrix}. \tag{3.24}$$

In the same form as Equation 3.22, it comes:

$$\mathbf{R}_{R_1\to R_2}\ \mathbf{x} = \mathbf{x} + \mathbf{\Lambda_x}\ \boldsymbol{\theta}_c \qquad \text{and} \qquad \mathbf{R}_{R_2\to R_1}\mathbf{x} = \mathbf{x} - \mathbf{\Lambda_x}\ \boldsymbol{\theta}_c, \tag{3.25}$$

with $\boldsymbol{\theta}_c$ defined in Equation 3.6 and $\mathbf{\Lambda_x}$ introduced in Equation 3.23.

Furthermore, another important rotation matrix is the one expressing vector of frame R_{b_n} in R_2, denoted by $R_{R_{b_n} \to R_2}$. It can be derived from the scheme of Figure 3.6.

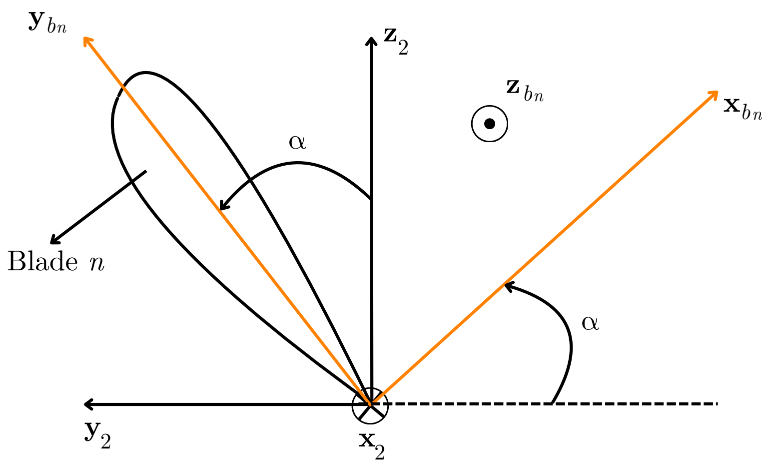

Figure 3.6: Propeller blade representation, with corresponding azimuthal angle α and undeformed R_{b_n} and R_2 frames, adapted from [14]. The blade is shown with $r_0 = 0$ for clarity.

The blade azimuthal angle $\alpha(t)$ of the nth blade, describing the azimuthal position of the blade at instant t, is defined as follows:

$$\alpha(t) = \underbrace{(n-1)\,\beta}_{\text{initial position of the blade at } t=0} + \underbrace{\Omega t}_{\text{change in position due to blade rotation}}, \tag{3.26}$$

where Ω is the propeller rotational speed and β the angular spacing between two consecutive blades. Since they are equally distributed over the propeller circumference, this angle is equal to:

$$\beta = \frac{2\pi}{N} = \frac{2\pi}{3} \tag{3.27}$$

for a three-bladed propeller.

Using trigonometric relations, the following relationships between vectors of R_{b_n} and R_2 can be obtained:

$$\begin{cases} \mathbf{x}_{b_n} = -\cos\alpha\ \mathbf{y}_2 + \sin\alpha\ \mathbf{z}_2 \\ \mathbf{y}_{b_n} = \sin\alpha\ \mathbf{y}_2 + \cos\alpha\ \mathbf{z}_2 \\ \mathbf{z}_{b_n} = -\mathbf{x}_2 \end{cases}. \tag{3.28}$$

In matrix form, it comes:

$$\begin{pmatrix} \mathbf{x}_{b_n} \\ \mathbf{y}_{b_n} \\ \mathbf{z}_{b_n} \end{pmatrix} = \underbrace{\begin{pmatrix} 0 & -\cos\alpha & \sin\alpha \\ 0 & \sin\alpha & \cos\alpha \\ -1 & 0 & 0 \end{pmatrix}}_{\mathbf{R}_{R_2 \to R_{b_n}}} \begin{pmatrix} \mathbf{x}_2 \\ \mathbf{y}_2 \\ \mathbf{z}_2 \end{pmatrix} = \mathbf{R}_{R_2 \to R_{b_n}} \begin{pmatrix} \mathbf{x}_2 \\ \mathbf{y}_2 \\ \mathbf{z}_2 \end{pmatrix}, \tag{3.29}$$

where $\mathbf{R}_{R_2 \to R_{b_n}}$ is the matrix expressing vectors of R_2 in frame R_{b_n}.
Hence, the matrix expressing vectors of R_{b_n} in R_2, noted as $\mathbf{R}_{R_{b_n} \to R_2}$ is given by:

$$\begin{pmatrix} \mathbf{x}_2 \\ \mathbf{y}_2 \\ \mathbf{z}_2 \end{pmatrix} = \underbrace{\begin{pmatrix} 0 & 0 & -1 \\ -\cos\alpha & \sin\alpha & 0 \\ \sin\alpha & \cos\alpha & 0 \end{pmatrix}}_{\mathbf{R}_{R_{b_n} \to R_2} \,=\, \mathbf{R}^T_{R_2 \to R_{b_n}}} \begin{pmatrix} \mathbf{x}_{b_n} \\ \mathbf{y}_{b_n} \\ \mathbf{z}_{b_n} \end{pmatrix} = \mathbf{R}_{R_{b_n} \to R_2} \begin{pmatrix} \mathbf{x}_{b_n} \\ \mathbf{y}_{b_n} \\ \mathbf{z}_{b_n} \end{pmatrix}, \tag{3.30}$$

verifying the inverse property of rotation matrices.

Additionally, the matrices expressing a vector of frame $\bar{R}_{b_n}$ in frame R_2, and a vector of frame $\bar{R}_{b_n}$ in frame R_1 are respectively given by:

$$\mathbf{R}_{\bar{R}_{b_n} \to R_2} = \mathbf{R}_{R_{b_n} \to R_2} \, \mathbf{R}_{\bar{R}_{b_n} \to R_{b_n}} \qquad \text{and} \qquad \mathbf{R}_{\bar{R}_{b_n} \to R_1} = \mathbf{R}_{R_2 \to R_1} \, \mathbf{R}_{\bar{R}_{b_n} \to R_2}. \tag{3.31}$$

Finally, the rotation matrix $\mathbf{R}_{R_{b_n} \to R_1}$ linking frames R_{b_n} and R_1 is written as:

$$\mathbf{R}_{R_{b_n} \to R_1} = \mathbf{R}_{R_2 \to R_1} \, \mathbf{R}_{R_{b_n} \to R_2}. \tag{3.32}$$

Note that, in the rest of this report, some transfer matrices are renamed such as $\mathbf{R}_n = \mathbf{R}_{R_{b_n} \to R_1}$, $\mathbf{P}_n = \mathbf{R}_{R_{b_n} \to R_2}$ and $\bar{\mathbf{R}}_n = \mathbf{R}_{\bar{R}_{b_n} \to R_1}$.

3.1.6 Derivation of the structural matrices

The structural matrices of the propeller and the supporting structure are derived separately, and are then assembled to form the system matrices. Additionally, they do not have the same size before assembly.
For the supporting structure, the matrices are directly written in the global coordinate space. Therefore, they are square and have a size equal to the total number of retained degrees of freedom after assembly. Therefore, they are of size $N\,(N_h + N_w + N_v + N_t) + q_{pylon}$, with q_{pylon} the number

of degrees of freedom of the pylon. Hence, it equals 2 in this case, as only the pitch θ and yaw ψ motions are considered. They all have the general following architecture:

$$\mathbf{X}_s = \begin{pmatrix} \mathbf{0} & \mathbf{0} \\ \mathbf{0} & \mathbf{X}_s^d \end{pmatrix}. \tag{3.33}$$

Indeed, since the matrices of the supporting structure refer to the pylon degrees of freedom θ and ψ, only their lower-right block $\mathbf{X}_s^d$ remains non-zero.

It is slightly different for the matrices of the propeller. Effectively, the equations of motion are derived by considering the propeller centre degrees of freedom $\mathbf{u}_c$ and $\boldsymbol{\theta}_c$, defined in 3.6. Therefore, they are square and have a size equal to the number of degrees of freedom of the system, before removing the degrees of freedom that are not retained in the final model. They are of size $N\left(N_h + N_w + N_v + N_t\right) + q_c$, with q_c the number of degrees of freedom of the propeller centre. Hence, it equals 6 in the present case, since u_c^x, u_c^y, u_c^z, φ, θ and ψ, all defined in 3.6, are used to derive the matrices. Therefore, the structural matrices of the propeller all have the following general architecture:

$$\mathbf{X} = \begin{pmatrix} \mathbf{X}_{blades} & \mathbf{X}_{blades,centre} \\ \mathbf{X}_{pylon,centre} & \mathbf{X}_{centre} \end{pmatrix}, \tag{3.34}$$

where $(\cdot)_{centre}$ designates the block associated with the propeller centre degrees of freedom. Additionally, $(\cdot)_{blades,centre}$ represents the interaction between the blade degrees of freedom and those of propeller centre.

These matrices are derived in Sections 3.1.7 and 3.1.8.

3.1.7 Supporting structure matrices

According to the architecture of the matrices of the supporting structure given in 3.33, only the lower-right matrix block must be defined. Additionally, it is important to note that, since the aerodynamic effects of the pylon are neglected, the supporting structure does not have any aerodynamic matrix. For the lower-right block of the damping matrix, it comes:

$$\mathbf{C}_s^d = \begin{pmatrix} C_\theta & 0 \\ 0 & C_\psi \end{pmatrix}. \tag{3.35}$$

Similarly, the block for the stiffness matrix is given by:

$$\mathbf{K}_s^d \;=\; \begin{pmatrix} K_\theta & 0 \\ 0 & K_\psi \end{pmatrix}. \tag{3.36}$$

Then, in order to model the coupling between the pitch and yaw motions of the pylon, a gyroscopic matrix is defined. If J_1^p describes the polar moment of inertia of the pylon about the pivot point, $J_1^p\,\Omega$ measures the intensity of this gyroscopic coupling. As stated in Section 2.1, the propeller rotation is responsible for a coupling between pitch and yaw motions. Therefore, if the propeller rotational speed Ω increases, the intensity of this coupling increases as well. Therefore, the gyroscopic matrix of the supporting structure is given by:

$$\mathbf{G}_s^d \;=\; \begin{pmatrix} 0 & -J_1^p\,\Omega \\ J_1^p\,\Omega & 0 \end{pmatrix}. \tag{3.37}$$

The polar moment of inertia J_1^p of the pylon depends on its actual geometry, which is discussed in Chapter 4.

Finally, the presence of the motor is taken into account in the mass matrix of the supporting structure. Attached at the end of the pylon, the motor plays a role in the dynamics, since its mass is not negligible. The integration of the motor into the model is described in Chapters 4 and 5. Since it precesses with the pylon, its inertia around the pivot point is included in the matrix. In order to compute it, the motor is assumed to be a concentrated mass placed at the end of the pylon, i.e. at a distance L_{pylon} from the pivot point. According to Meriam et al., the mass moment of inertia I of a mass m with a radius of gyration k equals [46]:

$$I \;=\; mk^2. \tag{3.38}$$

Thus, the mass matrix block is written as follows:

$$\mathbf{M}_s^d \;=\; \begin{pmatrix} J_2^p \;+\; m_{motor}\; L_{pylon}^2 & 0 \\ 0 & J_2^p \;+\; m_{motor}\; L_{pylon}^2 \end{pmatrix}, \tag{3.39}$$

where J_2^p denotes the transverse moment of inertia of the pylon, also discussed in Chapter 4.

Hence, once all the lower-right blocks are computed, the full matrices of the supporting structure can be derived. According to 3.33, the mass matrix of the supporting structure is given by:

$$\mathbf{M}_s = \begin{pmatrix} \mathbf{0} & \mathbf{0} \\ \mathbf{0} & \mathbf{M}_s^d \end{pmatrix}. \tag{3.40}$$

The gyroscopic, damping and stiffness matrices of the supporting structure, denoted respectively by $\mathbf{G}_s$, $\mathbf{C}_s$ and $\mathbf{K}_s$, have the same block structure.

3.1.8 Propeller structural matrices

As explained in Section 3.1.3, the propeller matrices are obtained from the principle of virtual power, stated in Equation 3.5. The virtual power of the external forces is responsible for the aerodynamic matrices of the propeller, while both remaining contributions lead to the structural propeller matrices.

Virtual power of acceleration of the propeller

First, the virtual power of acceleration of the propeller P_A is considered. As the hub is assumed to be rigid, the contributions of the flexible blades and the hub are separated such as:

$$P_A = P_A^{hub} + P_A^{blades} \tag{3.41}$$

On the one hand, the virtual power of acceleration of the hub P_A^{hub} is easily computed, since it is supposed to be rigid.
On the other hand, the virtual power of acceleration of the blades P_A^{blades} is developed in order to obtain the final expression of the linearized total virtual power of acceleration of the propeller P_A. The details of this derivation are given in the thesis of Vincent de Gaudemaris [14].

From this final expression, mass, gyroscopic and spin softening matrices, denoted respectively by $\mathbf{M}_c$, $\mathbf{G}_c$ and $\mathbf{N}_c$, are obtained by identification. The mass matrix $\mathbf{M}_c$ is, by definition, the matrix associated with the acceleration of the generalized coordinates vector, while the gyroscopic matrix $\mathbf{G}_c$ is associated with the velocity. The spin softening matrix $\mathbf{N}_c$ multiplies the generalized coordinates vector itself. The expression of the virtual power of acceleration of the propeller can be approximated as:

$$P_A \approx \mathbf{M}_c(t)\,\ddot{\mathbf{y}}_c + \mathbf{G}_c(t)\,\dot{\mathbf{y}}_c + \mathbf{N}_c(t)\,\mathbf{y}_c. \tag{3.42}$$

The mass matrix $\mathbf{M}_c(t)$ is given by:

$$\mathbf{M}_c(t) = \begin{pmatrix} \mathbf{M}_1^a & \mathbf{0} & ... & ... & \mathbf{0} & \mathbf{M}_1^b(t) \\ \mathbf{0} & \mathbf{M}_2^a & \ddots & & \vdots & \vdots \\ \vdots & \ddots & \ddots & \ddots & \vdots & \vdots \\ \vdots & & \ddots & \ddots & \mathbf{0} & \vdots \\ \mathbf{0} & \cdots & \cdots & \mathbf{0} & \mathbf{M}_N^a & \mathbf{M}_N^b(t) \\ \mathbf{M}_1^c(t) & \cdots & \cdots & \cdots & \mathbf{M}_N^c(t) & \mathbf{M}^d \end{pmatrix} \tag{3.43}$$

where

$$\mathbf{M}_n^a = \begin{pmatrix} \int_{r_0}^R \rho_b \; S(r) \; \mathbf{\Phi}^T \mathbf{\Phi} \; dr & \mathbf{0} \\ \mathbf{0} & \int_{r_0}^R \mathbf{\Phi}_t^T \; \mathbf{e}_y^T \mathbf{J}(r) \; \mathbf{e}_y \; \mathbf{\Phi}_t \; dr \end{pmatrix} \tag{3.44}$$

$$\mathbf{M}_n^b(t) = \begin{pmatrix} \int_{r_0}^R \rho_b \; S(r) \; \mathbf{\Phi}^T \mathbf{P}_n^T \; dr & -\int_{r_0}^R \rho_b \; S(r) \; r \; \mathbf{\Phi}^T \mathbf{\Lambda}_{\mathbf{e}_y} \mathbf{P}_n^T \; dr \\ \mathbf{0} & \int_{r_0}^R \mathbf{\Phi}_t^T \mathbf{e}_y^T \mathbf{J}(r) \; \mathbf{P}_n^T \; dr \end{pmatrix} \tag{3.45}$$

$$\mathbf{M}_n^c(t) = \mathbf{M}_n^b(t)^T \tag{3.46}$$

$$\mathbf{M}_d = \begin{pmatrix} m & 0 & 0 & 0 & 0 & 0 \\ 0 & m & 0 & 0 & 0 & 0 \\ 0 & 0 & m & 0 & 0 & 0 \\ 0 & 0 & 0 & J_1 & 0 & 0 \\ 0 & 0 & 0 & 0 & J_2 & 0 \\ 0 & 0 & 0 & 0 & 0 & J_2 \end{pmatrix} \tag{3.47}$$

with ρ_b the blade density, assumed constant along the blade, and $S(r)$ denoting the blade cross-section at a location r from the blade root. Moreover, vector $\mathbf{e}_y$ is defined as follows:

$$\mathbf{e}_y = \begin{pmatrix} 0 \\ 1 \\ 0 \end{pmatrix}. \tag{3.48}$$

Therefore, following the definition of $\mathbf{\Lambda}_{\mathbf{x}}$ for an arbitrary $\mathbf{x}$ vector, $\mathbf{\Lambda}_{\mathbf{e}_y}$ can be written as:

$$\mathbf{\Lambda}_{\mathbf{e}_y} = \begin{pmatrix} 0 & 0 & 1 \\ 0 & 0 & 0 \\ -1 & 0 & 0 \end{pmatrix}. \tag{3.49}$$

Additionally, as a reminder, matrix $\mathbf{P}_n$, defined in Section 3.1.2, is the matrix expressing the basis vector of frame R_{b_n} in frame R_2.

The propeller mass, including the hub, is denoted by m. J_1 and J_2 are the polar and transverse moments of inertia of the propeller, respectively, including the hub contribution and expressed at the propeller centre. They are given by [14]:

$$J_1 = N \int_{r_0}^{R} \rho_b \; S(r) \; r^2 \; dr \;\; + J_1^h \tag{3.50}$$

and

$$J_2 = \frac{N}{2} \int_{r_0}^{R} \rho_b \; S(r) \; r^2 \; dr \; + \; \frac{N}{2} \int_{r_0}^{R} \rho_b \; I_y(r) \; dr \; + \; J_2^h \tag{3.51}$$

considering that J_1^h and J_2^h are the polar and transverse moments of inertia of the hub. All of these terms are described in detail in Chapter 4, where the analytical model is applied to a real case. Following the Euler-Bernoulli assumption explained in Section 3.1.1, the geometric and gravity centres are placed on the elastic axis. Therefore, the moments of inertia associated with bending displacements are neglected. Hence the inertia matrix of the blade cross-sections $\mathbf{J}$, expressed at the shear centre, is defined as:

$$\mathbf{J}(r) \;\; = \begin{pmatrix} 0 & 0 & 0 \\ 0 & \rho_b \; I_y(r) & 0 \\ 0 & 0 & 0 \end{pmatrix}, \tag{3.52}$$

where $I_y(r)$ is the polar second moment of area of the blade cross-section located at a radial location r. Since the propeller blades are approximated as cantilever straight beams, $I_y(r)$ is equal to the sum of the second moment of area of a beam section about axis $\mathbf{x}_{b_n}$, denoted by I_x and the second moment of area of a beam section around axis $\mathbf{z}_{b_n}$, denoted by I_z. Both quantities characterize the resistance of the beam cross-section to bending about the corresponding axes and are given by [47]:

$$I_x(r) \;\; = \;\; \frac{c(r) \; t(r)^3}{12} \qquad \text{and} \qquad I_z(r) \;\; = \;\; \frac{c(r)^3 \; t(r)}{12}, \tag{3.53}$$

where $c(r)$ and $t(r)$ are the blade chord and maximum thickness at a location r from the blade root. Therefore, it comes:

$$I_y(r) \;\; = \;\; I_x(r) \; + \; I_z(r) \;\; = \;\; \frac{c(r) \; t(r)^3}{12} \; + \; \frac{c(r)^3 \; t(r)}{12}. \tag{3.54}$$

Now, the gyroscopic matrix can be established. Although the final matrices are written in the generalized coordinate space associated with $\mathbf{y}_c$, the blade deformations are expressed in the rotating undeformed blade frames R_{b_n}. Therefore, Coriolis effects have to be taken into account in the gyroscopic matrix. According to Goldstein et al., Coriolis effects occur when motion is described in a rotating frame. Their magnitude increases with the propeller rotational speed [44].

Additionally, due to the pylon motion, the orientation of the propeller plane changes, which introduces gyroscopic effects. These effects are also included in the gyroscopic matrix. Its expression is given by:

$$\mathbf{G}_c(t) = \Omega \begin{pmatrix} \mathbf{G}_1^a & \mathbf{0} & \dots & \dots & \mathbf{0} & \mathbf{G}_1^b(t) \\ \mathbf{0} & \mathbf{G}_2^a & \ddots & & \vdots & \vdots \\ \vdots & \ddots & \ddots & \ddots & \vdots & \vdots \\ \vdots & & \ddots & \ddots & \mathbf{0} & \vdots \\ \mathbf{0} & \cdots & \cdots & \mathbf{0} & \mathbf{G}_N^a & \mathbf{G}_N^b(t) \\ \mathbf{G}_1^c(t) & \cdots & \cdots & \cdots & \mathbf{G}_N^c(t) & \mathbf{G}^d \end{pmatrix} \tag{3.55}$$

where

$$\mathbf{G}_n^a = \begin{pmatrix} 2\int_{r_0}^{R} \rho_b \; S(r) \; \mathbf{\Phi}^T \mathbf{\Lambda}_{\mathbf{e}_z} \mathbf{\Phi} \; dr & \int_{r_0}^{R} \partial_r \mathbf{\Phi}^T \mathbf{\Lambda}_{\mathbf{e}_y}^T \mathbf{\Lambda}_{\mathbf{e}_z} \mathbf{J}(r) \; \mathbf{e}_y \mathbf{\Phi}_t \; dr \\ \int_{r_0}^{R} \mathbf{\Phi}_t^T \mathbf{e}_y^T \mathbf{J}(r) \; \mathbf{\Lambda}_{\mathbf{e}_z} \mathbf{\Lambda}_{\mathbf{e}_y} \; \partial_r \mathbf{\Phi} \; dr & \mathbf{0} \end{pmatrix} \tag{3.56}$$

$$\mathbf{G}_n^b(t) = \begin{pmatrix} \mathbf{0} & 2\int_{r_0}^{R} \rho_b \; S(r) \; r \; \mathbf{\Phi}^T \mathbf{\Lambda}_{\mathbf{e}_x} \mathbf{P}_n^T \; dr + \int_{r_0}^{R} \partial_r \mathbf{\Phi}^T \mathbf{\Lambda}_{\mathbf{e}_y}^T \mathbf{\Lambda}_{\mathbf{e}_z} \mathbf{J}(r) \; \mathbf{P}_n^T \; dr \\ \mathbf{0} & -\int_{r_0}^{R} \mathbf{\Phi}_t^T \mathbf{e}_y^T \mathbf{J}(r) \; \mathbf{\Lambda}_{\mathbf{e}_z} \mathbf{P}_n^T \; dr \end{pmatrix} \tag{3.57}$$

$$\mathbf{G}_n^c(t) = \begin{pmatrix} 2\int_{r_0}^{R} \rho_b \; S(r) \; \mathbf{P}_n \mathbf{\Lambda}_{\mathbf{e}_z} \mathbf{\Phi} \; dr & \mathbf{0} \\ 2\int_{r_0}^{R} \rho_b \; S(r) \; r \; \mathbf{P}_n \mathbf{\Lambda}_{\mathbf{e}_y} \mathbf{\Lambda}_{\mathbf{e}_z} \mathbf{\Phi} \; dr + \int_{r_0}^{R} \mathbf{P}_n \mathbf{J}(r) \; \mathbf{\Lambda}_{\mathbf{e}_z} \mathbf{\Lambda}_{\mathbf{e}_y} \; \partial_r \mathbf{\Phi} \; dr & \int_{r_0}^{R} \mathbf{P}_n \mathbf{\Lambda}_{\mathbf{e}_z} \mathbf{J}(r) \; \mathbf{e}_y \mathbf{\Phi}_t \; dr \end{pmatrix} \tag{3.58}$$

$$\mathbf{G}^d = \begin{pmatrix} 0 & 0 & 0 & 0 & 0 & 0 \\ 0 & 0 & 0 & 0 & 0 & 0 \\ 0 & 0 & 0 & 0 & 0 & 0 \\ 0 & 0 & 0 & 0 & 0 & 0 \\ 0 & 0 & 0 & 0 & 0 & -J_1 \\ 0 & 0 & 0 & 0 & -J_1 & 0 \end{pmatrix} \tag{3.59}$$

with J_1 defined in Equation 3.50. Additionally, matrices $\mathbf{\Lambda}_{\mathbf{e}_x}$ and $\mathbf{\Lambda}_{\mathbf{e}_x}$ can be derived similarly to $\mathbf{\Lambda}_{\mathbf{e}_y}$, written in 3.49, following the definition of 3.23.

Furthermore, vectors $\mathbf{e}_x$ and $\mathbf{e}_z$ are written as follows:

$$\mathbf{e}_x = \begin{pmatrix} 1 \\ 0 \\ 0 \end{pmatrix} \qquad \text{and} \qquad \mathbf{e}_z = \begin{pmatrix} 0 \\ 0 \\ 1 \end{pmatrix}. \tag{3.60}$$

Finally, the spin softening matrix can be introduced. Spin softening, also called centrifugal softening, is associated with the inertial effects induced by the propeller rotation. As the rotational speed increases, these effects can reduce the effective blade stiffness, and therefore decrease some of the natural frequencies [48].

The spin softening matrix is written as:

$$\mathbf{N}_c(t) = \begin{pmatrix} \mathbf{N}_1^a & \mathbf{0} & \dots & \dots & \mathbf{0} & \mathbf{0} \\ \mathbf{0} & \mathbf{N}_2^a & \ddots & & \vdots & \vdots \\ \vdots & \ddots & \ddots & \ddots & \vdots & \vdots \\ \vdots & & \ddots & \ddots & \mathbf{0} & \vdots \\ \mathbf{0} & \cdots & \cdots & \mathbf{0} & \mathbf{N}_N^a & \mathbf{0} \\ \mathbf{N}_1^c(t) & \cdots & \cdots & \cdots & \mathbf{N}_N^c(t) & \mathbf{0} \end{pmatrix} \tag{3.61}$$

with

$$\mathbf{N}_n^a = \begin{pmatrix} \displaystyle\int_{r_0}^{R} \rho_b \, S(r) \, \mathbf{\Phi}^T \mathbf{\Lambda}_{\mathbf{e}_z}^2 \mathbf{\Phi} \, dr + \int_{r_0}^{R} \partial_r \mathbf{\Phi}^T \mathbf{\Lambda}_{\mathbf{e}_y}^T \mathbf{\Lambda}_{\mathbf{e}_z} \mathbf{J}(r) \, \mathbf{\Lambda}_{\mathbf{e}_z} \mathbf{\Lambda}_{\mathbf{e}_y} \partial_r \mathbf{\Phi} \, dr & \mathbf{0} \\ \mathbf{0} & \mathbf{0} \end{pmatrix} \tag{3.62}$$

$$\mathbf{N}_n^c(t) = \begin{pmatrix} \displaystyle\int_{r_0}^{R} \rho_b \, S(r) \, \mathbf{P}_n \mathbf{\Lambda}_{\mathbf{e}_z}^2 \mathbf{\Phi} \, dr & \mathbf{0} \\ \displaystyle\int_{r_0}^{R} \rho_b \, S(r) \, r \, \mathbf{P}_n \mathbf{\Lambda}_{\mathbf{e}_z} \mathbf{\Lambda}_{\mathbf{e}_x} \mathbf{\Phi} \, dr + \int_{r_0}^{R} \mathbf{P}_n \mathbf{\Lambda}_{\mathbf{e}_z} \mathbf{J}(r) \, \mathbf{\Lambda}_{\mathbf{e}_y} \partial_r \mathbf{\Phi} \, dr & \mathbf{0} \end{pmatrix} \tag{3.63}$$

where $\mathbf{\Lambda}_{\mathbf{e}_z}^2$ represents the matrix product $\mathbf{\Lambda}_{\mathbf{e}_z} \ \mathbf{\Lambda}_{\mathbf{e}_z}$.

Virtual power of internal forces

The virtual power of internal forces can be decomposed into two contributions: one associated with the elastic deformation of the blades, and one associated with the mechanical energy dissipation, as follows:

$$P_{int} = P_{int}^{def} + P_{int}^{damp}. \tag{3.64}$$

On the one hand, the virtual power of the elastic deformations results from the four types of blade flexibility considered in this model, i.e. traction, torsion, in-plane and out-of-plane bending. On the other hand, the virtual power of mechanical energy dissipation comes from the viscous damping related to these blade deformations.

Similarly to the virtual power of acceleration, both contributions are computed separately, before being assembled in order to form the final expression of P_{int}^{prop}. From this final expression, the structural matrices are identified. The damping matrix is associated with the velocity of the generalized coordinate vector, while the stiffness matrix is associated with the vector itself. Moreover, this stiffness matrix is divided in two contributions, as shown in the following approximate linearized expression of the virtual power of internal forces of the propeller:

$$P_{int} \approx \mathbf{C}_c \, \dot{\mathbf{y}}_c + \left(\mathbf{K}_c + \mathbf{K}_p^c\right) \mathbf{y}_c. \tag{3.65}$$

The classical stiffness matrix $\mathbf{K}_c$ is given by:

$$\mathbf{K}_c = \begin{pmatrix} \mathbf{K}_1 & \mathbf{0} & \dots & \dots & \mathbf{0} & \mathbf{0} \\ \mathbf{0} & \mathbf{K}_2 & \ddots & & \vdots & \vdots \\ \vdots & \ddots & \ddots & \ddots & \vdots & \vdots \\ \vdots & & \ddots & \ddots & \mathbf{0} & \vdots \\ \mathbf{0} & \cdots & \cdots & \mathbf{0} & \mathbf{K}_N & \mathbf{0} \\ \mathbf{0} & \cdots & \cdots & \cdots & \mathbf{0} & \mathbf{0} \end{pmatrix} \tag{3.66}$$

with

$$\mathbf{K}_n = \begin{pmatrix} \int_{r_0}^{R} \left(E_b S(r) \, \partial_r \mathbf{\Phi}^T \mathbf{e}_y^T \mathbf{e}_y \partial_r \mathbf{\Phi} + E_b I_z(r) \, \partial_r^2 \mathbf{\Phi}^T \mathbf{e}_x^T \mathbf{e}_x \partial_r^2 \mathbf{\Phi} + E_b I_x(r) \, \partial_r^2 \mathbf{\Phi}^T \mathbf{e}_z^T \mathbf{e}_z \partial_r^2 \mathbf{\Phi} \right) dr & \mathbf{0} \\ \mathbf{0} & \int_{r_0}^{R} G_b I_y(r) \, \partial_r \mathbf{\Phi}_t^T \partial_r \mathbf{\Phi}_t \, dr \end{pmatrix} \tag{3.67}$$

The second moments of area $I_x(r)$ and $I_z(r)$, and the second polar moment of area $I_y(r)$ are respectively defined in Equations 3.53 and 3.54.

Moreover, E_b is the Young modulus of the blade material, whereas G_b denotes its shear modulus. It is written as [49]:

$$G_b = \frac{E_b}{2\,(1 + \nu_b)}, \tag{3.68}$$

with ν_b the Poisson ratio of the blade material.

The second contribution to the stiffness matrix is the prestress stiffness matrix, denoted by

$\mathbf{K}_p^c$. This matrix models the effect of the blade geometric stiffening, also called centrifugal stiffening. Indeed, when a blade is rotating, a centrifugal force is exerted in the axial direction of the blade, increasing the effective blade stiffness, compared with a non-rotating configuration [50].

This matrix is written as follows:

$$\mathbf{K}_p^c = \begin{pmatrix} \mathbf{K}_1^p & \mathbf{0} & ... & ... & \mathbf{0} & \mathbf{0} \\ \mathbf{0} & \mathbf{K}_2^p & \ddots & & \vdots & \vdots \\ \vdots & \ddots & \ddots & \ddots & \vdots & \vdots \\ \vdots & & \ddots & \ddots & \mathbf{0} & \vdots \\ \mathbf{0} & \cdots & \cdots & \mathbf{0} & \mathbf{K}_N^p & \mathbf{0} \\ \mathbf{0} & \cdots & \cdots & \cdots & \mathbf{0} & \mathbf{0} \end{pmatrix}. \tag{3.69}$$

where

$$\mathbf{K}_n^p = \begin{pmatrix} \int_{r_0}^{R} \left(\left(\int_{r}^{R} \rho_b \ S(x) \ x dx \right) \ \partial_r \mathbf{\Phi}^T \mathbf{e}_z \mathbf{e}_z^T \ \partial_r \mathbf{\Phi} \ + \ \partial_r \mathbf{\Phi}^T \mathbf{e}_x \mathbf{e}_x^T \ \partial_r \mathbf{\Phi} \right) dr & \mathbf{0} \\ \mathbf{0} & \int_{r_0}^{R} \left(\left(\int_{r}^{R} \rho_b \ S(x) \ x dx \right) \dfrac{I_y(r)}{S(r)} \ \partial_r \mathbf{\Phi}_t^T \partial_r \mathbf{\Phi}_t \right) dr \end{pmatrix} \tag{3.70}$$

Finally, the structural damping matrix $\mathbf{C}_c$ is given by:

$$\mathbf{C}_c = \begin{pmatrix} \mathbf{C}_1 & \mathbf{0} & ... & ... & \mathbf{0} & \mathbf{0} \\ \mathbf{0} & \mathbf{C}_2 & \ddots & & \vdots & \vdots \\ \vdots & \ddots & \ddots & \ddots & \vdots & \vdots \\ \vdots & & \ddots & \ddots & \mathbf{0} & \vdots \\ \mathbf{0} & \cdots & \cdots & \mathbf{0} & \mathbf{C}_N & \mathbf{0} \\ \mathbf{0} & \cdots & \cdots & \cdots & \mathbf{0} & \mathbf{0} \end{pmatrix} \tag{3.71}$$

with

$$\mathbf{C}_n = \begin{pmatrix} \int_{r_0}^{R} \left(C_{tract} \ \mathbf{\Phi}^T \mathbf{e}_y \mathbf{e}_y^T \mathbf{\Phi} \ + \ C_{flex} \ \mathbf{\Phi}^T \mathbf{e}_x \mathbf{e}_x^T \mathbf{\Phi} \ + \ C_{flex} \ \mathbf{\Phi}^T \mathbf{e}_z \mathbf{e}_z^T \mathbf{\Phi} \right) \ dr & \mathbf{0} \\ \mathbf{0} & \int_{r_0}^{R} C_{tor} \ \mathbf{\Phi}_t^T \mathbf{\Phi}_t \ dr \end{pmatrix}, \tag{3.72}$$

where C_{tract}, C_{flex} and C_{tor} are the damping coefficients associated with blade traction, bending and torsion, respectively.

3.1.9 Propeller aerodynamic matrices

As stated before, the aerodynamic matrices of the propeller are obtained via the computation of the virtual power of external forces. In the present model, the external forces exerted on the blades are aerodynamic forces, which are computed using a quasi-steady aerodynamic approach. The virtual power of the external forces acting on the complete propeller is defined as the sum of the virtual powers of external forces acting on each blade, as follows:

$$P_{ext} = \sum_{i=0}^{N} P_{ext}^{i}, \tag{3.73}$$

where N is the total number of blades.

Similarly to the structural matrices, the final linearized formulation of the virtual power is derived, from which the aerodynamic damping and stiffness matrices are identified. The aerodynamic damping matrix $\mathbf{C}_{ac}$ is associated with the velocity of the generalized coordinates vector, whereas the aerodynamic stiffness matrix $\mathbf{K}_{ac}$ is associated with the vector itself.
The calculation is performed in three steps. First, the loads are computed on the blade cross-sections at each radial position. Then, these cross-section loads are integrated along the blade span to obtain the loads acting on the entire blade. Finally, the contributions of all blades are combined to obtain the final expression of the virtual power of the external forces acting on the propeller.

The lift $\mathbf{f}_l$ and drag $\mathbf{f}_d$ forces acting on the blades are applied at the quarter-chord of the blade profile. At a given radial position, these forces depend on the blade relative velocity $\mathbf{u}$, the blade twist angle γ, as well as the inflow angle ϕ, defined as the angle between the relative velocity and the propeller plane, all evaluated at the considered radial location.
Figure 3.7 shows the aerodynamic forces and flow quantities associated with the rotating deformed blade.

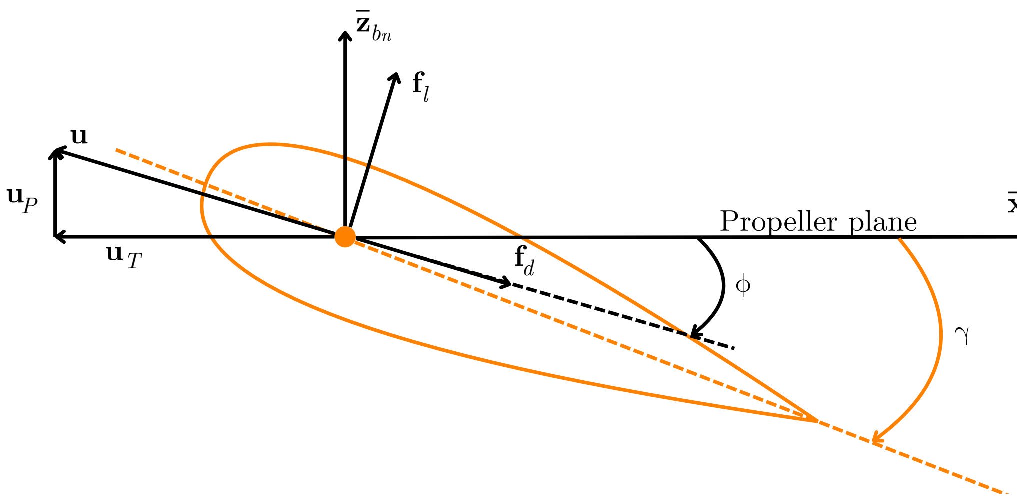

Figure 3.7: Blade representation in the deformed frame $\bar{R}_{b_n}$ with the lift force $\mathbf{f}_l$ and drag force $\mathbf{f}_d$, decomposition of the relative velocity $\mathbf{u}$ into two contributions $\mathbf{u}_P$ and $\mathbf{u}_T$, blade twist angle γ and inflow angle ϕ, adapted from [14].

The relative velocity of the blade in the deformed frame can be decomposed into two contributions as:

$$\mathbf{u} = \mathbf{u}_{flow} + \mathbf{u}_{blade}, \tag{3.74}$$

where $\mathbf{u}_{flow}$ comes from the incident velocity projected onto the deformed blade frame $\bar{R}_{b_n}$, whereas $\mathbf{u}_{blade}$ represents the velocity of the quarter-chord point induced by the blade motion, expressed in the $\bar{R}_{b_n}$ frame.

The expression of $\mathbf{u}_{flow}$ is given by:

$$\mathbf{u}_{flow} = -\bar{\mathbf{R}}_n^T \mathbf{v}_\infty + V_a\, \mathbf{e}_z + V_t\, \mathbf{e}_x, \tag{3.75}$$

where $\mathbf{v}_\infty$ is the free-stream velocity vector expressed in the fixed frame R_1, defined as:

$$\mathbf{v}_\infty = \begin{pmatrix} V \\ 0 \\ 0 \end{pmatrix}. \tag{3.76}$$

Additionally, the quantities V_a and V_t denote the axial and tangential propeller induced velocities generated by the propeller rotation in a flow. They are computed using the blade element momentum theory, as explained in Section 3.2.

After linearization, the components of the relative velocity vector $\mathbf{u}$ along $\bar{\mathbf{x}}_{b_n}$ and $\bar{\mathbf{z}}_{b_n}$ are respectively written as:

$$u_T = \mathbf{u} \cdot (-\mathbf{e}_x) = u_T^0 + u_T' \qquad \text{and} \qquad u_P = \mathbf{u} \cdot \mathbf{e}_z = u_P^0 + u_P', \tag{3.77}$$

with $u_P^0 = V + V_a$ and $u_T^0 = r\,\Omega - V_t$ denoting the steady parts of the out-of-plane and in-plane relative velocities of the blade cross-section, respectively. Moreover, u_P' and u_T' are called the disturbed velocities. Their detailed expressions are not repeated here and can be found in the thesis of Vincent de Gaudemaris [14].

The aerodynamic loads of each blade are first written using local aerodynamic variables. For the n^{th} blade, these variables are gathered in the vector $\mathbf{y}_n$. The corresponding blade-level aerodynamic matrices are therefore first obtained in this local aerodynamic variable space.
However, the equations of motion of the propeller are written in the generalized coordinate space associated with vector $\mathbf{y}_c$, defined in 3.16. Hence, the local aerodynamic variables of blade n must be expressed in terms of the generalized coordinates gathered in $\mathbf{y}_{n,c}$, which contains the generalized coordinates of blade n as well as the propeller-centre degrees of freedom.

This change of coordinates introduces the transformation matrices $\mathbf{T}_0(t)$, $\mathbf{T}_1(t)$, $\mathbf{T}_2(t)$ and $\mathbf{T}_3(t)$, leading to the blade-level aerodynamic matrices $\mathbf{C}_{n,c}$ and $\mathbf{K}_{n,c}$. Their detailed expressions are given in Appendix A. Only the expressions required to understand the assembly of the complete propeller matrices are developed here.

For the n^{th} blade, the transformed aerodynamic damping and stiffness contributions are respectively written as:

$$\mathbf{C}_{n,c}(t) = \mathbf{T}_2(t)\,\mathbf{C}_n + \mathbf{T}_2(t)\,\mathbf{K}_n\,\mathbf{T}_1(t). \qquad \text{and} \qquad \mathbf{K}_{n,c}(t) = \mathbf{T}_2(t)\,\mathbf{K}_n\,\mathbf{T}_0(t) + \mathbf{T}_3(t), \tag{3.78}$$

where $\mathbf{C}_n$ and $\mathbf{K}_n$ are the local aerodynamic damping and stiffness matrices of blade n, respectively. Their expressions are defined in Appendix A.
Although $\mathbf{K}_n$ is associated with the blade-level aerodynamic stiffness contribution, it also appears in the expression of $\mathbf{C}_{n,c}$. This comes from the coordinate transformation between the local aerodynamic variables and the generalized coordinates: the local variables depend on the generalized velocity vector through $\mathbf{T}_1(t)$. Consequently, part of the blade-level aerodynamic stiffness contribution becomes proportional to the generalized velocity vector and contributes to the aerodynamic damping matrix.

To assemble the aerodynamic matrices of the complete propeller, the blade-level matrices are decomposed into blocks separating the blade deformation degrees of freedom from the propeller-centre degrees of freedom. For the aerodynamic damping contribution of the n^{th} blade, this block decomposition is written as:

$$\mathbf{C}_{n,c} = \begin{pmatrix} \mathbf{C}_n^a & \mathbf{C}_n^b \\ \mathbf{C}_n^c & \mathbf{C}_n^d \end{pmatrix}. \tag{3.79}$$

The block $(\cdot)^a$ is a square block of size $N_q + N_t$ associated with the blade degrees of freedom. The blocks $(\cdot)^b$ and $(\cdot)^c$ describe the coupling between the blade and propeller-centre degrees of freedom, with respective sizes $(N_q + N_t) \times q_c$ and $q_c \times (N_q + N_t)$. Finally, the lower-right block $(\cdot)^d$ is a square block of size q_c associated with the propeller-centre degrees of freedom.

The computation of $\mathbf{C}_{n,c}$ requires several intermediate quantities, which are introduced in Appendix A. These quantities are not discussed individually, but are provided for the completeness of the aerodynamic matrices.

Finally, the aerodynamic damping matrix of the complete propeller is then obtained by assembling the block contributions of all blades:

$$\mathbf{C}_{ac} = -\begin{pmatrix} \mathbf{C}_1^a & \mathbf{0} & \dots & \dots & \mathbf{0} & \mathbf{C}_1^b \\ \mathbf{0} & \mathbf{C}_2^a & \ddots & & \vdots & \vdots \\ \vdots & \ddots & \ddots & \ddots & \vdots & \vdots \\ \vdots & & \ddots & \ddots & \mathbf{0} & \vdots \\ \mathbf{0} & \cdots & \cdots & \mathbf{0} & \mathbf{C}_N^a & \mathbf{C}_N^b \\ \mathbf{C}_1^c & \cdots & \cdots & \cdots & \mathbf{C}_N^c & \sum_{n=1}^{N} \mathbf{C}_n^d \end{pmatrix} \tag{3.80}$$

Similarly to the damping matrix, the block matrix elements of $\mathbf{K}_{ac}$ are obtained from the blade-level matrix $\mathbf{K}_{n,c}$, defined in 3.78, as follows:

$$\mathbf{K}_{n,c} = \begin{pmatrix} \mathbf{K}_n^a & \mathbf{K}_n^b \\ \mathbf{K}_n^c & \mathbf{K}_n^d \end{pmatrix} \tag{3.81}$$

Following the same procedure, the aerodynamic stiffness matrix $\mathbf{K}_{ac}$ is obtained by assembling the block decomposition of the blade-level stiffness contributions. Its general expression is given by:

$$\mathbf{K}_{ac} = - \begin{pmatrix} \mathbf{K}_1^a & \mathbf{0} & \dots & \dots & \mathbf{0} & \mathbf{K}_1^b \\ \mathbf{0} & \mathbf{K}_2^a & \ddots & & \vdots & \vdots \\ \vdots & \ddots & \ddots & \ddots & \vdots & \vdots \\ \vdots & & \ddots & \ddots & \mathbf{0} & \vdots \\ \mathbf{0} & \cdots & \cdots & \mathbf{0} & \mathbf{K}_N^a & \mathbf{K}_N^b \\ \mathbf{K}_1^c & \cdots & \cdots & \cdots & \mathbf{K}_N^c & \sum_{n=1}^{N} \mathbf{K}_n^d \end{pmatrix}. \tag{3.82}$$

After assembly, the final approximate linearized expression of the virtual power of the external forces acting on the entire propeller can be written as:

$$P_{ext}^{prop} \approx \mathbf{C}_{ac}(t)\,\dot{\mathbf{y}}_c + \mathbf{K}_{ac}(t)\,\mathbf{y}_c. \tag{3.83}$$

The matrices $\mathbf{C}_{ac}$ and $\mathbf{K}_{ac}$ are therefore identified as the aerodynamic damping and stiffness matrices of the propeller, respectively. All the matrices required to compute $\mathbf{K}_{ac}$ and $\mathbf{C}_{ac}$ are defined in Appendix A.

3.1.10 Derivation of the equations of motion

As a reminder, the virtual powers are derived using the blade degrees of freedom, as well as the propeller-centre ones, which are defined as: $\mathbf{u}_c = \begin{pmatrix} u_c^x \\ u_c^y \\ u_c^z \end{pmatrix}$ and $\boldsymbol{\theta}_c = \begin{pmatrix} \varphi \\ \theta \\ \psi \end{pmatrix}$. Nevertheless, the retained degrees of freedom in the present model are the blade degrees of freedom, as well as the pitch θ and yaw ψ motions of the pylon. Therefore, the propeller-centre degrees of freedom have to be expressed as functions of both retained degrees of freedom.

The pitch motion of the pylon has two contributions. First, the vertical translation of the propeller centre is related to a pitch motion of the pylon through the following relation:

$$u_c^z = L_{pylon}\,\theta. \tag{3.84}$$

Then, a pitch angle of the propeller centre θ results directly in a pitch motion θ of the pylon. Similarly, the yaw motion of the pylon induces a horizontal displacement of the propeller centre. It is given by:

$$u_c^y = -L_{pylon}\,\psi, \tag{3.85}$$

where the minus sign comes from the convention adopted in the present model. This can be visualized from Figures 3.2 and 3.3. The propeller-centre yaw angle is also directly equal to the pylon yaw angle. These relations are gathered in matrix $\mathbf{P}$, which links the propeller-centre degrees of freedom $\mathbf{u}_c$ and $\boldsymbol{\theta}_c$ to both retained pylon ones θ and ψ.

Therefore, the coordinate transformation matrix $\mathbf{P}_{tot}$ is given by:

$$\begin{pmatrix} \mathbf{q}_1 \\ \mathbf{t}_1 \\ \vdots \\ \mathbf{q}_N \\ \mathbf{t}_N \\ \mathbf{u}_c \\ \boldsymbol{\theta}_c \end{pmatrix} = \underbrace{\begin{pmatrix} \mathbf{I} & \mathbf{0} & \mathbf{0} & \mathbf{0} & \mathbf{0} \\ \mathbf{0} & \mathbf{I} & \mathbf{0} & \mathbf{0} & \mathbf{0} \\ \vdots & & \ddots & & \vdots \\ \mathbf{0} & \mathbf{0} & \mathbf{0} & \mathbf{I} & \mathbf{0} \\ \mathbf{0} & \mathbf{0} & \mathbf{0} & \mathbf{0} & \mathbf{P} \end{pmatrix}}_{\mathbf{P}_{tot}} \underbrace{\begin{pmatrix} \mathbf{q}_1 \\ \mathbf{t}_1 \\ \vdots \\ \mathbf{q}_N \\ \mathbf{t}_N \\ \theta \\ \psi \end{pmatrix}}_{\mathbf{y}} \quad \text{considering that} \quad \begin{pmatrix} \mathbf{u}_c \\ \boldsymbol{\theta}_c \end{pmatrix} = \underbrace{\begin{pmatrix} 0 & 0 \\ 0 & -L_{pylon} \\ L_{pylon} & 0 \\ 0 & 0 \\ 1 & 0 \\ 0 & 1 \end{pmatrix}}_{\mathbf{P}} \begin{pmatrix} \theta \\ \psi \end{pmatrix}, \tag{3.86}$$

where vector $\mathbf{q}_n$ gathers all the generalized coordinates of blade n, except those associated with torsion. Vector $\mathbf{t}_n$ contains the generalized coordinates associated with the torsion. Additionally, $\mathbf{y}$ gathers the generalized coordinates of all the blades, ordered by blades, as well as the retained propeller-centre degrees of freedom θ and ψ. These vectors are explained in Section 3.1.4.

The blade degrees of freedom remain unchanged, as shown by the identity matrices $\mathbf{I}$ placed on the diagonal blocks of $\mathbf{P}_{tot}$ related to the blade degrees of freedom.

Thus, as stated before, the equations of motion of the complete system are derived from the principle of virtual power, introduced in Equation 3.5. Hence, acceleration, internal forces and external forces contributions, respectively denoted by P_A, P_{int} and P_{ext}, are combined into one single expression, giving:

$$\mathbf{M}(t)\,\ddot{\mathbf{y}} + (\mathbf{C} + \mathbf{G}(t))\,\dot{\mathbf{y}} + (\mathbf{N}(t) + \mathbf{K} + \mathbf{K}_p)\,\mathbf{y} = -\mathbf{C}_a(t)\,\dot{\mathbf{y}} - \mathbf{K}_a(t)\,\mathbf{y}, \tag{3.87}$$

which is a time-dependent system of equations.

By taking into account the change in degrees of freedom, the system matrices are given by:

$$\mathbf{M}(t) = \mathbf{P}_{tot}^T\,\mathbf{M}_{\mathbf{c}}(t)\,\mathbf{P}_{tot} + \mathbf{M}_s \tag{3.88}$$

$$\mathbf{G}(t) = \mathbf{P}_{tot}^T\,\mathbf{G}_c(t)\,\mathbf{P}_{tot} + \mathbf{G}_s \tag{3.89}$$

$$\mathbf{C} \;=\; \mathbf{P}_{tot}^{T}\,\mathbf{C}_c\,\mathbf{P}_{tot} \;+\; \mathbf{C}_s \tag{3.90}$$

$$\mathbf{N}(t) \;=\; \mathbf{P}_{tot}^{T}\,\mathbf{N}_c(t)\,\mathbf{P}_{tot} \tag{3.91}$$

$$\mathbf{K} \;=\; \mathbf{P}_{tot}^{T}\,\mathbf{K}_c\,\mathbf{P}_{tot} \;+\; \mathbf{K}_s \tag{3.92}$$

$$\mathbf{K}_p \;=\; \mathbf{P}_{tot}^{T}\,\mathbf{K}_p^{c}\,\mathbf{P}_{tot} \tag{3.93}$$

$$\mathbf{C}_a(t) \;=\; \mathbf{P}_{tot}^{T}\,\mathbf{C}_{ac}(t)\,\mathbf{P}_{tot} \tag{3.94}$$

$$\mathbf{K}_a(t) \;=\; \mathbf{P}_{tot}^{T}\,\mathbf{K}_{ac}(t)\,\mathbf{P}_{tot} \;-\; \mathbf{K}_a^{stat} \tag{3.95}$$

with the structural matrices of the supporting structure $\mathbf{M}_s$, $\mathbf{G}_s$, $\mathbf{C}_s$ and $\mathbf{K}_s$ defined in Section 3.1.7. Additionally, $\mathbf{K}_a^{stat}$ represents the influence of a steady axial force applied on the propeller. This force modifies the effective stiffness of the system and $\mathbf{K}_a^{stat}$ is expressed as:

$$\mathbf{K}_a^{stat} \;=\; \begin{pmatrix} \mathbf{0} & \mathbf{0} \\ \mathbf{0} & \begin{pmatrix} L_{pylon}\; f_{c_x}^{stat} & 0 \\ 0 & L_{pylon}\; f_{c_x}^{stat} \end{pmatrix} \end{pmatrix} \tag{3.96}$$

where $f_{c_x}^{stat}$ represents the axial force applied on the propeller, for instance the propeller thrust.

Thus, Equation 3.87 indicates that the system is still time-dependent, making a classical eigenvalue analysis impossible. The system must therefore be transformed into a time-independent form. This can be performed through the multi-blade coordinates transformation.

3.1.11 Multi-blade coordinates (MBC) transformation

In this section, the MBC transformation is first theoretically introduced in a general form. It is then applied to the equations of motion obtained by the analytical method, in order to show how they can be modified to perform a classical eigenvalue analysis.

The multi-blade coordinates transformation, also called the Coleman-Feingold transform, has been introduced by Coleman and Feingold. This method is widely used for propeller and helicopter applications [51]. It allows the transformation of a system with time-periodic coefficients into a constant system. This transformation gets rid of the dominant periodic terms, while the remaining ones are sufficiently small to be considered as negligible. Nevertheless, this method is only applicable for three or more bladed propellers. Below three blades, the resulting system can still depend on time [14, 51].

The importance of this approach is critical. Specifically, it makes possible a classical eigenvalues resolution, leading to relevant modal and stability analyses [52].

For rotating systems such as the one considered in this work, both rotating and non-rotating frames can be defined, as discussed in Section 3.1.2. The MBC transformation projects the rotating blade degrees of freedom onto the fixed frame, while leaving the non-rotating coordinates unchanged. This allows the behaviour of the entire system to be studied in the fixed frame. Therefore, the MBC method can be interpreted as a coordinate transformation from the rotating blade coordinates to non-rotating multi-blade coordinates [52, 53].

The new MBC coordinates, gathered in vector $\boldsymbol{\xi}$, are built from linear combinations of all the rotating coordinates. Figure 3.8 illustrates the origin of the transformation. These new coordinates can be interpreted as the components, in the fixed non-rotating frame, of the collective deformation of the rotor obtained from the blade degrees of freedom initially expressed in the rotating frame.

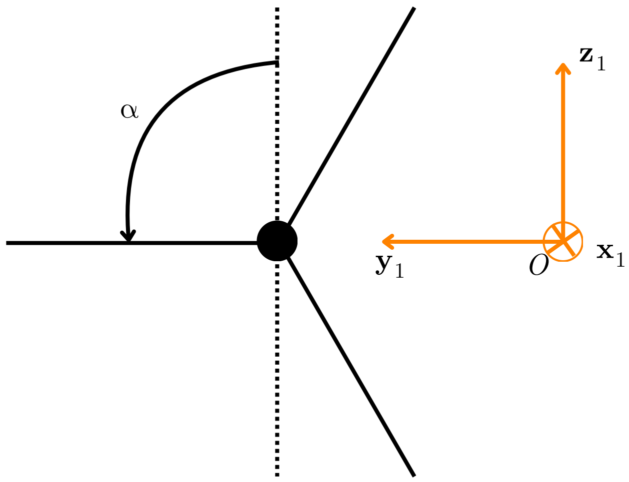

Figure 3.8: Three-bladed propeller represented in the fixed frame R_1 with the blade azimuthal angle.

For an N-bladed propeller, these new coordinates are expressed through the following relations [52, 53]:

$$\xi_0 = \frac{1}{N}\sum_{n=1}^{N} q_n \tag{3.97}$$

$$\xi_{ic} = \frac{2}{N}\sum_{n=1}^{N} q_n \cos\left(i\alpha_n\right) \tag{3.98}$$

$$\xi_{is} = \frac{2}{N}\sum_{n=1}^{N} q_n \sin\left(i\alpha_n\right) \tag{3.99}$$

$$\xi_{\frac{N}{2}} = \frac{1}{N}\sum_{n=1}^{N} q_n \left(-1\right)^n , \tag{3.100}$$

where q_n is one particular rotating generalized coordinate of the n^{th} blade and α_n the blade azimuthal angle of the $n^{th}-$blade, defined in 3.26.

It is also important to note that the $\xi_{\frac{N}{2}}$ MBC coordinate, called the differential coordinate, is only relevant when N is even. Additionally, the inverse transformation associated to blade n for a three-bladed propeller, required to recover the rotating blade coordinates, is given by [52]:

$$q_n \; = \; \xi_0 \; + \; \xi_{1c} \; \cos\alpha_n \; + \; \xi_{1s} \; \sin\alpha_n. \tag{3.101}$$

Furthermore, ξ_{ns} and ξ_{nc} are the sine and cosine cyclic multi-blade coordinates, respectively. They are important for the identification of the whirl flutter modes. According to Reed, these modes can couple with pylon modes and lead to whirl flutter instabilities. In contrast, the non-rotating degree of freedom ξ_0 does not couple with the pylon modes responsible for this type of instability [13]. Therefore, a mode for which ξ_{ns} and ξ_{nc} are negligible compared with the ξ_0 coordinates cannot be identified as a whirl flutter mode.

Additionally, the physical interpretation of the multi-blade coordinates gathered in $\boldsymbol{\xi}$ differs from that of the initial rotating blade coordinates. These coordinates can no longer be directly associated with individual blade motion. Instead, they represent, in the fixed frame, the behaviour that accounts for the cumulative motion of all the propeller blades.

For instance, G.Bir takes the example where q_n represents a blade out-of-plane deformation. In this case, the multi-blade coordinates correspond to motion of the complete propeller plane, instead of individual blade motions. In particular, ξ_{nc} describes the horizontal motion of the rotor centre of mass in the rotor plane, whereas ξ_{ns} represents the same motion, but vertically [52, 53].

In the present model, the rotating blade degrees of freedom are expressed in the undeformed blade frame, denoted by R_{b_n}. However, the degrees of freedom θ and ψ of the pylon are already expressed with respect to the non-rotating frame R_1. Therefore, these two are not transformed by the MBC transformation.

In order to understand this transformation, the generalized coordinate vector

$$\mathbf{y} \; = \; \left(\mathbf{q}_1^T \; \mathbf{t}_1^T \; \dots \; \mathbf{q}_N^T \; \mathbf{t}_N^T \; \theta \; \psi\right)^T \tag{3.102}$$

is first reordered. Instead of being sorted by blades, the generalized coordinates are grouped according to their associated shape functions. The resulting vector $\mathbf{y}_\xi$ is then given by:

$$\mathbf{y}_\xi \;=\; \left(q_1^1 \;\dots\; q_N^1 \;\dots\; q_1^{N_q} \;\dots\; q_N^{N_q} \; t_1^1 \;\dots\; t_N^1 \; t_1^{N_t} \;\dots\; t_1^{N_t} \; \theta \; \psi\right)^T, \tag{3.103}$$

and the vectors $\mathbf{y}$ and $\mathbf{y}_\xi$ are linked by a reordering matrix $\mathbf{Q}$, only made of zeros and ones such that $\mathbf{y} \;=\; \mathbf{Q}\,\mathbf{y}_\xi$.

Therefore, the first N coefficients of vector $\mathbf{y}_\xi$ correspond to the first generalized coordinate of each blade, i.e. the first coordinate associated with the first shape function.

Applied to the first N components of vector $\mathbf{y}_\xi$, the MBC transformation gives:

$$\boldsymbol{\xi}_q^1 \;=\; \mathbf{X}(t)^{-1} \begin{pmatrix} q_1^1 \\ \vdots \\ q_N^1 \end{pmatrix}, \tag{3.104}$$

with $\boldsymbol{\xi}_q^1 \;=\; (\xi_0 \; \xi_{1c} \; \xi_{1s})^T$ gathering the multi-blade coordinates associated with the corresponding initial generalized coordinates. Furthermore, for a three-bladed propeller, matrix $\mathbf{X}(t)$ is given by:

$$\mathbf{X}(t) \;=\; \begin{pmatrix} 1 & \cos\alpha_1 & \sin\alpha_1 \\ 1 & \cos\alpha_2 & \sin\alpha_2 \\ 1 & \cos\alpha_3 & \sin\alpha_3 \end{pmatrix}, \tag{3.105}$$

with $\alpha_n \;=\; (n \;-\; 1)\;\frac{2\pi}{3} + \Omega\, t$ the azimuthal angle of the n^{th} blade already introduced in Equation 3.26.

Applying the same principle for all the components of $\mathbf{y}_\xi$, it comes:

$$\mathbf{y}_\xi \;=\; \underbrace{\begin{pmatrix} \mathbf{X}(t) & & & \\ & \ddots & & \\ & & \mathbf{X}(t) & \\ & & & \begin{matrix} 1 & 0 \\ 0 & 1 \end{matrix} \end{pmatrix}}_{\mathbf{X}_{tot}} \underbrace{\begin{pmatrix} \boldsymbol{\xi}_q^1 \\ \vdots \\ \boldsymbol{\xi}_q^{N_q} \\ \boldsymbol{\xi}_t^1 \\ \vdots \\ \boldsymbol{\xi}_t^{N_t} \\ \theta \\ \psi \end{pmatrix}}_{\boldsymbol{\xi}}, \tag{3.106}$$

which corresponds to the inverse MBC transformation of the entire system since it relates $\mathbf{y}_\xi$ as a function of $\boldsymbol{\xi}$, which is expressed in the non-rotating frame R_1. Additionally, the final diagonal block of $\mathbf{X}_{tot}$ is an identity matrix, since the pylon degrees of freedom are not affected by the transformation. Thus, the relation between vectors $\mathbf{y}$ and $\boldsymbol{\xi}$ can be established as:

$$\mathbf{y} \;=\; \mathbf{Q}\;\mathbf{X}_{tot}\;\boldsymbol{\xi} \;=\; \mathbf{T}(t)\;\boldsymbol{\xi}, \tag{3.107}$$

with $\mathbf{T}(t)$ the MBC transformation matrix, defined as $\mathbf{T}(t) \;=\; \mathbf{Q}\;\mathbf{X}_{tot}(t)$.

Once the multi-blade coordinates are clearly defined, it is possible to integrate them into the new equations of motion, which are written as:

$$\mathbf{M}_{MBC}\;\ddot{\boldsymbol{\xi}} \;+\; \mathbf{C}_{MBC}\;\dot{\boldsymbol{\xi}} \;+\; \mathbf{K}_{MBC}\;\boldsymbol{\xi} \;=\; \mathbf{0}, \tag{3.108}$$

where $\mathbf{M}_{MBC}$, $\mathbf{C}_{MBC}$ and $\mathbf{K}_{MBC}$ are the mass, damping and stiffness matrices of the system, respectively, after the MBC transformation.
They are defined as:

$$\mathbf{M}_{MBC} \;=\; \mathbf{T}^T(t)\;\mathbf{M}(t)\;\mathbf{T}(t) \tag{3.109}$$

$$\mathbf{C}_{MBC} \;=\; 2\;\mathbf{T}^T(t)\;\mathbf{M}(t)\;\dot{\mathbf{T}}(t) \;+\; \mathbf{T}^T(t)\;\left(\mathbf{C} \;+\; \mathbf{G}(t) \;+\; \mathbf{C}_a(t)\right)\;\mathbf{T}(t) \tag{3.110}$$

$$\mathbf{K}_{MBC} \;=\; \mathbf{T}^T(t)\,\mathbf{M}(t)\,\ddot{\mathbf{T}}(t) + \mathbf{T}^T(t)\;\left(\mathbf{C} \;+\; \mathbf{G}(t) \;+\; \mathbf{C}_a(t)\right)\;\dot{\mathbf{T}}(t) + \mathbf{T}^T(t)\left(\mathbf{K} \;+\; \mathbf{N}(t) \;+\; \mathbf{K}_p \;+\; \mathbf{K}_a(t)\right)\;\mathbf{T}(t), \tag{3.111}$$

where $\dot{\mathbf{T}}(t)$ and $\ddot{\mathbf{T}}(t)$ respectively denote the first and second time derivatives of the MBC transformation matrix $\mathbf{T}(t)$. They are given by:

$$\dot{\mathbf{T}}(t) \;=\; \mathbf{Q}\;\dot{\mathbf{X}}_{tot} \qquad \text{and} \qquad \ddot{\mathbf{T}}(t) \;=\; \mathbf{Q}\;\ddot{\mathbf{X}}_{tot}. \tag{3.112}$$

First and second time derivatives of matrix $\mathbf{X}_{tot}$ are easily obtained by deriving the expression of $\mathbf{X}_{tot}$ given in 3.106. In particular, they are defined as:

$$\dot{\mathbf{X}}_{tot} \;=\; \begin{pmatrix} \dot{\mathbf{X}}(t) & & & \\ & \ddots & & \\ & & \dot{\mathbf{X}}(t) & \\ & & & 0 \;\; 0 \\ & & & 0 \;\; 0 \end{pmatrix} \qquad \text{and} \qquad \ddot{\mathbf{X}}_{tot} \;=\; \begin{pmatrix} \ddot{\mathbf{X}}(t) & & & \\ & \ddots & & \\ & & \ddot{\mathbf{X}}(t) & \\ & & & 0 \;\; 0 \\ & & & 0 \;\; 0 \end{pmatrix}, \tag{3.113}$$

considering that

$$\dot{\mathbf{X}}(t) \;=\; \Omega \begin{pmatrix} 0 & -\sin\psi_1 & \cos\psi_1 \\ 0 & -\sin\psi_2 & \cos\psi_2 \\ 0 & -\sin\psi_3 & \cos\psi_3 \end{pmatrix} \quad \text{and} \quad \ddot{\mathbf{X}}(t) \;=\; -\Omega^2 \begin{pmatrix} 0 & \cos\psi_1 & \sin\psi_1 \\ 0 & \cos\psi_2 & \sin\psi_2 \\ 0 & \cos\psi_3 & \sin\psi_3 \end{pmatrix}. \tag{3.114}$$

Once all of these expressions are assembled together via Equation 3.108, the equations of motion are expressed in the non-rotating frame R_1. Thanks to the MBC transformation, they are now time-independent and they can be transformed in the state-space form to conduct a classical eigenvalue analysis.
This gives:

$$\mathbf{M}_{MBC}\,\ddot{\boldsymbol{\xi}} \;=\; -\mathbf{C}_{MBC}\,\dot{\boldsymbol{\xi}} \;-\; \mathbf{K}_{MBC}\,\boldsymbol{\xi} \tag{3.115}$$

$$\Rightarrow \ddot{\boldsymbol{\xi}} \;=\; -\mathbf{M}_{MBC}^{-1}\,\mathbf{C}_{MBC}\,\dot{\boldsymbol{\xi}} - \mathbf{M}_{MBC}^{-1}\,\mathbf{K}_{MBC}\,\boldsymbol{\xi}, \tag{3.116}$$

with the associated following state-space representation of the system:

$$\begin{pmatrix} \ddot{\boldsymbol{\xi}} \\ \dot{\boldsymbol{\xi}} \end{pmatrix} = \underbrace{\begin{pmatrix} \mathbf{0} & \mathbf{I} \\ -\mathbf{M}_{MBC}^{-1}\,\mathbf{K}_{MBC} & -\mathbf{M}_{MBC}^{-1}\,\mathbf{C}_{MBC} \end{pmatrix}}_{\mathbf{A}} \begin{pmatrix} \dot{\boldsymbol{\xi}} \\ \boldsymbol{\xi} \end{pmatrix} \;=\; \mathbf{A} \begin{pmatrix} \dot{\boldsymbol{\xi}} \\ \boldsymbol{\xi} \end{pmatrix}. \tag{3.117}$$

As this state-space matrix is time-independent, a classical eigenvalue analysis of the system can be performed in order to conduct a stability analysis of the system. The eigenvalue computation is detailed in Section 3.3.

3.1.12 Method validation

Once the method is implemented, it has to be shown, through a test case, that it is done correctly. The test considered here is based on the analysis of the work of V. de Gaudemaris [14].
The validation is performed using stability maps, in which dimensionless parameters are varied. Depending on the map, prestress and aerodynamic effects are either included or neglected. Moreover, only one map considers all the blade flexibilities simultaneously. For the remaining maps, each blade flexibility is isolated. The non-dimensional parameters are defined as follows:

- the dimensionless stiffness $\bar{EI}_x \;=\; \frac{1.8751^4 EI_x}{(R-r_0)^4 \rho_b \; S \; \Omega^2}$,
- the flapping frequency ratio $\gamma_{\beta_1} \;=\; \sqrt{1 \;+\; \bar{EI}_x}$,

- the dimensionless stiffnesses $\bar{K}_{\theta,\psi} = \frac{\frac{K_{\theta,\psi}}{\frac{J_2^{tot}}{2}}}{\Omega^2}$,

- the dimensionless torsional stiffness: $\bar{GI_y} = \frac{\pi^2 \; GI_y}{4(R-r_0)^2 \rho_b \; I_y \; \Omega^2}$.

Table 3.1 summarizes the key parameters of this test case.

Parameter	Value
Number of shape functions for the in-plane bending N_h	4
Number of shape functions for the out-of-plane bending N_w	4
Number of shape functions for the traction N_v	2
Number of shape functions for the torsion N_t	3
Number of blades	4
Propeller radius R_p	1.2 m
Hub radius r_0	0 m
Propeller rotation speed Ω	157 rad/s
Free stream velocity V	150 m/s
Air density ρ_a	1.225 kg/m^3
Blade section static pitching moment m_0	0 N/m
Blade section zero lift incidence angle α_0	0 rad
Blade twist angle γ	$\arctan\left(\frac{V}{\Omega r}\right)$ rad
Blade section lift curve slope a_l	2π 1/rad
Propeller induced velocities V_a and V_t	0 m/s
Blade chord c	0.15 m
Blade section drag coefficient C_d	0
Pitch damping coefficient C_θ	0 N.m.s
Yaw damping coefficient C_ψ	0 N.m.s
Pitch stiffness coefficient K_θ	Variable
Yaw stiffness coefficient K_ψ	Variable
Blade linear mass $\rho_b \; S$	1.0715 kg/m
Blade section polar moment of inertia $\rho_b \; I_y$	$8.407 \cdot 10^{-4}$ kg.m
Out-of-plane bending stiffness EI_x	8000 N.m^2
In-plane bending stiffness EI_z	12000 N.m^2
Axial stiffness ES	$1.5 \cdot 10^8$ N
Torsional stiffness GI_y	800 N.m^2
Torsion structural damping coefficient C_{tor}	0.005 N.s
Bending structural damping coefficient C_{flex}	0 N.s/m^2
Traction structural damping coefficient C_{tract}	0 N.s/m^2

Table 3.1: Parameters of the test case used in the thesis, from V. de Gaudemaris [14].

When only the out-of-plane blade motion is retained, without the prestress effects but with aerodynamic effects, Figures 3.9a and 3.9b are obtained.

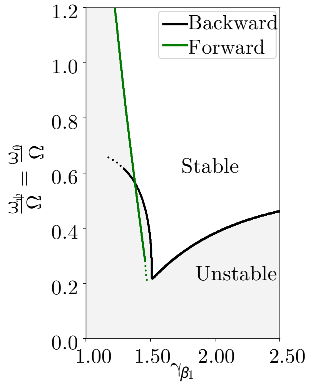

(a) Results obtained by V. de Gaudemaris [14].

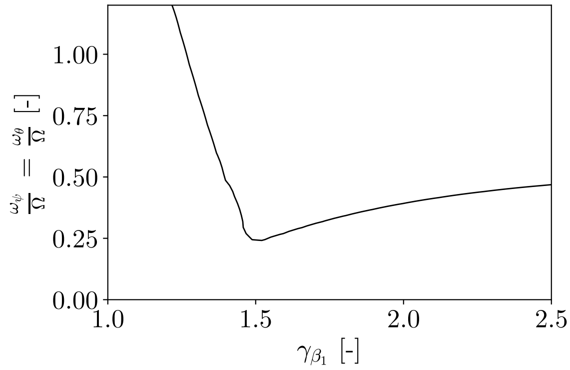

(b) Results obtained with considered implementation.

Figure 3.9: Comparison between the present implementation and the results of V. de Gaudemaris for the evolution of $\frac{\omega_{\theta,\psi}}{\Omega}$ as a function of γ_{β_1} with aerodynamic effects, without prestress effects and considering only out-of-plane blade motion.

Other verification plots are presented in Appendix B, for different cases. For the blade torsion, V. de Gaudemaris states that the system is stable for all stiffness configurations when aerodynamic effects are not considered. He does not provide any plot to compare but Figure B.9 verifies this statement, except for a small region near the origin, which can be considered as negligible.

3.2 Induced velocity computation

In Section 3.1.9, the importance of the computation of the induced velocities is highlighted for the computation of the propeller aerodynamic matrices. The present section explains how these velocities are computed.

First, the velocity triangle is introduced in order to define the blade relative-flow components. Figure 3.10 shows two velocity triangles corresponding to two different radial positions. These triangles relate the axial and tangential components of the absolute V and relative u velocities, if the radial component is assumed negligible. Additionally, the considered blade chord is assumed to be equal at both radial positions.

It is important to note that the velocity triangles are represented before the flow passes through the propeller, i.e. the flow is not yet modified by the propeller rotation. The purpose of Figure 3.10 is to identify the different contributions to the relative flow velocity seen by the blade.

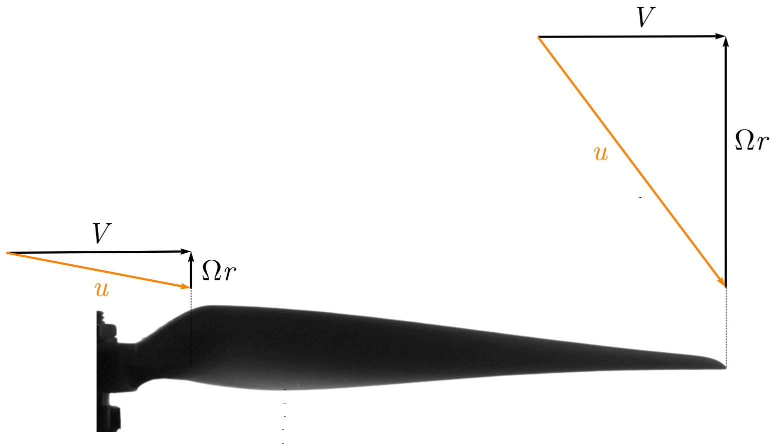

Figure 3.10: Representation of the velocity triangles for two different radii, adapted from Hillewaert K. [54].

From this Figure, it can be seen that blade angle of attack depends on the considered radius location. Indeed, the rotational speed at the spanwise location r equals Ωr. Therefore, as the radius increases, the tangential component of the relative velocity increases, which modifies both the magnitude and the direction of the relative flow seen by the blades.

However, due to propeller rotation, the airflow is deflected in both tangential and axial directions. In order to produce thrust, the propeller accelerates the flow, while the tangential induced velocity component comes from the rotation imposed on the flow by the propeller.
The computation of the induced velocities relies on both blade element method (BEM) and blade element momentum theory (BEMT), which are both briefly explained in Sections 3.2.1 and 3.2.2, respectively.

By denoting the axial and tangential induced velocities V_a and V_t, respectively, the magnitude of the relative flow seen by the rotating blade is given by:

$$u(r) = \sqrt{(V + V_a)^2 + (\Omega r - V_t)^2}, \tag{3.118}$$

where Ωr is the tangential velocity of the propeller at the spanwise location r.

3.2.1 Blade element theory (BET)

First introduced by Stefan Drzewiecki in 1920, the blade element theory, widely used for propeller aerodynamic computations, allows the blade-section loads to be calculated from geometric and aerodynamic parameters such as the blade twist angle, the blade section lift and drag coefficients, as well as the blade chord.

This theory has several advantages. In particular, it allows variable geometrical quantities along the blade radius, such as the blade twist angle and chord. It also enables the propeller torque to be computed. Nevertheless, since it is a two-dimensional method, the spanwise flow over the blade is neglected, as well as unsteady effects. Moreover, BET does not account for aeroelastic coupling by itself. Such coupling appears only when the aerodynamic loads are combined with a structural dynamic model. [55].

Another limitation of the BET is its reduced validity close to the blade hub. In this region, hub-induced aerodynamic effects are significant, and the blade geometry is usually thick and strongly three-dimensional in order to ensure a smooth transition from the hub to the aerodynamic part of the blade. Therefore, BET generally starts from approximately 20% to 30% of the total blade radius, depending on the blade geometry.

This method treats the blade as a collection of multiple blade elements, each represented as an independent two-dimensional airfoil. First, the differential lift and drag forces of one element are given by [55]:

$$df_l(r) \;=\; \frac{1}{2}\rho_a u^2(r)\; c(r)\; C_l(r)\; dr \qquad \text{and} \qquad df_d(r) \;=\; \frac{1}{2}\rho_a u^2(r)\; c(r)\; C_d(r)\; dr, \tag{3.119}$$

where $u(r)$ is the blade relative velocity, $c(r)$ the chord, ρ_a the density of the air and $C_l(r)$ and $C_d(r)$ the lift and drag coefficients of the blade airfoil section, respectively.

The axial force and moment generated by the blade element are then obtained by projecting these lift and drag contributions onto the directions of interest. In the deformed blade frame, the axial component created by the N blades is written as [14]:

$$df(r) \;=\; -\frac{1}{2}\rho_a u^2(r)N\; c(r)\;\; (C_l \cos\phi \;-\; C_d \sin\phi)\;\; dr, \tag{3.120}$$

and, similarly, the axial moment exerted by the blades is given by [14]:

$$dq(r) \;=\; \frac{1}{2}\rho_a u^2(r)N\; c(r)\;\; (C_l \sin\phi \;+\; C_d \cos\phi)\;\; rdr, \tag{3.121}$$

expressed at the propeller centre.

These expressions follow the sign convention of the deformed blade frame used in the present model [14].

The relative velocity $u(r)$ of these equations depends on the induced velocities, which BET cannot predict by itself. Therefore, the problem is not closed and another theory must be introduced in order to finally compute the blade loads and induced velocities. This additional theory is called the one-dimensional momentum theory. Section 3.2.2 presents a combined BET-momentum theory method, called the blade element momentum theory (BEMT).

3.2.2 Blade element momentum theory (BEMT)

The blade element momentum theory, also called the blade element method (BEM), was first introduced by Glauert in 1935 [23]. This theory is based on mass and momentum conservation principles and assumes a steady, inviscid and incompressible flow, as well as uniform in the circumference direction. Moreover, the coupling between radial sections is neglected. These assumptions define the framework of the method [22].

By applying Newton's second law, V. de Gaudemaris states that the axial rate of change of linear momentum in the annular streamtube equals the axial force applied to this streamtube by the blades. Similarly, the axial rate of change of angular momentum equals the axial moment applied to the streamtube by the blades [14]. This leads to a system of two equations, allowing the induced velocities V_a and V_t to be computed at each radial location. This system is expressed as [14]:

$$\begin{cases} 8\pi r V_a\,(V + V_a) = \left((V + V_a)^2 + (\Omega r - V_t)^2\right)\, Nc\,\left(C_l \cos\phi_0 - C_d \sin\phi_0\right) \\ 8\pi r V_t\,(V + V_a) = \left((V + V_a)^2 + (\Omega r - V_t)^2\right)\, Nc\,\left(C_l \sin\phi_0 + C_d \cos\phi_0\right) \end{cases} \tag{3.122}$$

with ϕ_0, denoting the inflow angle of a blade section, is given by:

$$\phi_0 = \arctan\left(\frac{V + V_a}{\Omega r - V_t}\right). \tag{3.123}$$

Therefore, this system of equations must be solved to each radius, in order to obtain the complete induced velocity radial distributions $V_a(r)$ and $V_t(r)$. The blade lift coefficient C_l is computed at an angle α given by:

$$\alpha = \gamma - \phi_0 - \alpha_0, \tag{3.124}$$

with γ the blade twist angle at the given location and α_0 the zero-lift incidence angle of the airfoil.

Algorithm 1 summarizes the procedure of the blade element momentum theory used to compute the radial distributions of the induced velocities, where k is the iteration number. The residual tolerance ε_{res} is set to 10^{-8}. Additionally, the induced velocity computation starts at 30% and finishes at 98% of the blade radius, because the complex shape near the blade root complicates the calculation [54]. Therefore, as a first approximation, the induced velocities for radii between the root and 0.3 R_p are assumed to be equal to the first computed value. Analogously, the velocities after 98%

of the radius are equal to the last computed value.

Algorithm 1 Nonlinear BEMT solver for the induced velocities

Require: V, Ω, blade geometry, airfoil polar data, residual tolerance ε_{res}
Ensure: Induced velocities $V_a(r)$ and $V_t(r)$
for each radial station r_i **do**
Find the corresponding chord c_i and twist angle γ_i
Computation of the Reynolds number Re to find the corresponding C_l and C_d
Define several initial guesses for (V_a, V_t):

$$(V_a^{\text{init}}, V_t^{\text{init}}), \quad (0,0), \quad (-0.1V, 0), \quad (0, 0.1\Omega r_i)$$

for each initial guess **do**
Solve the nonlinear BEMT system for (V_a, V_t) using a root-finding method:

$$\begin{cases} 8\pi r V_a\,(V + V_a) = \left((V + V_a)^2 + (\Omega r - V_t)^2\right) Nc\,\left(C_l \cos\phi_0 - C_d \sin\phi_0\right) \\ 8\pi r V_t\,(V + V_a) = \left((V + V_a)^2 + (\Omega r - V_t)^2\right) Nc\,\left(C_l \sin\phi_0 + C_d \cos\phi_0\right), \end{cases}$$

where

$$\phi_0 = \arctan\left(\frac{V + V_a}{\Omega r - V_t}\right) \qquad \text{and} \qquad \alpha = \gamma_i - \phi_0 - \alpha_0$$

Reject non-physical branches if $V + V_a \leq 0$ or $\Omega r_i - V_t \leq 0$
If the root-finding method converges, compute the residual norm $\|R(V_a, V_t)\|_2$
end for
Retain the converged solution with the smallest residual norm
Accept the solution only if

$$\|R(V_a, V_t)\|_2 < \varepsilon_{\text{res}}$$

Use the retained solution as initial guess for the next radial station
end for
return $V_a(r)$, $V_t(r)$

Additionally, in order to converge to physically relevant solutions, several initial guesses are tested. The system is solved for each of them, and the retained solution is the one associated with the smallest residual. Depending on the initial guess, some computations can lead to non-convergent solutions. These solutions are therefore not kept. Moreover, $R\,(V_a, V_t)$ is defined as the residual vector $\begin{pmatrix} R_1\,(V_a, V_t) \\ R_2\,(V_a, V_t) \end{pmatrix}$ with

$$R_1\,(V_a, V_t) = V_a - \frac{\left((V + V_a)^2 + (\Omega r - V_t)^2\right) Nc\,\left(C_l \cos\phi_0 - C_d \sin\phi_0\right)}{8\pi r_i\,(V + V_a)} \tag{3.125}$$

and

$$R_2\,(V_a, V_t) = V_t - \frac{\left((V + V_a)^2 + (\Omega r - V_t)^2\right) Nc\,\left(C_l \sin\phi_0 + C_d \cos\phi_0\right)}{8\pi r_i\,(V + V_a)}. \tag{3.126}$$

3.3 Eigenvalue analysis of a linear time-invariant system

As the equations of motion are time-independent, linear, and written under the state-space form, as introduced in 3.117, the stability of the system can be studied by looking at its eigenvalues.

For linear time-invariant systems, a classical eigenvalues analysis can be performed. Mathematically, an eigenvalue problem is defined by the following equation [56]:

$$(\mathbf{A} \;-\; \lambda \mathbf{I})\, \boldsymbol{\phi}_r \;=\; 0, \tag{3.127}$$

where λ is the complex eigenvalue associated by definition, with the non-zero vector $\boldsymbol{\phi}_r$, called the eigenvector. For instance, matrix $\mathbf{A}$ is the state-space system matrix introduced in Equation 3.117. Moreover, the eigenvalue is defined as:

$$\lambda \;=\; \underbrace{\sigma}_{\text{real part}} \;+\; \underbrace{i\,\omega}_{\text{imaginary part}}\;, \tag{3.128}$$

with ω the angular frequency of the mode. Linked to the period T, this pulsation equals:

$$\omega \;=\; \frac{2\,\pi}{T}. \tag{3.129}$$

Concerning the mode oscillation frequency f, it is given by:

$$f \;=\; \frac{\omega}{2\pi}. \tag{3.130}$$

The real part governs the stability of the mode. This is described in detail in Section 3.4.

Furthermore, if matrix $(\mathbf{A} - \lambda\mathbf{I})$ were invertible, Equation 3.127, by multiplying on both sides by the inverse, would become:

$$(\mathbf{A} - \lambda \mathbf{I})^{-1} (\mathbf{A} - \lambda \mathbf{I})\;\; \boldsymbol{\phi}_r \;=\; (\mathbf{A} - \lambda \mathbf{I})^{-1}\;\; \mathbf{0}, \tag{3.131}$$

leading to a zero eigenvector $\boldsymbol{\phi}_r = \mathbf{0}$. However, by definition, an eigenvector must be non-zero, meaning that matrix $(\mathbf{A} - \lambda\mathbf{I})$ is not invertible [56].
Therefore, Equation 3.127 allows a non-zero solution $\boldsymbol{\phi}_r$ if and only if matrix $(\mathbf{A} - \lambda\mathbf{I})$ is singular. Following the definition of a singular matrix, the eigenvalues of a system are obtained from [56]:

$$\det(\mathbf{A} \;-\; \lambda \mathbf{I}) \;=\; 0, \tag{3.132}$$

which is called the characteristic equation.

Furthermore, a matrix, denoted by $\mathbf{\Lambda}$, gathering all the eigenvalues of matrix $\mathbf{A}$ on its diagonal can be defined. Another matrix, denoted by $\mathbf{\Phi}_r$, is introduced to gather the corresponding right eigenvectors. In particular, each column of $\mathbf{\Phi}_r$ is one right eigenvector of $\mathbf{A}$. Thus, the relationship between $\mathbf{A}$, $\mathbf{\Lambda}$ and $\mathbf{\Phi}_r$ is written as [57]:

$$\mathbf{A}\mathbf{\Phi}_r = \mathbf{\Phi}_r\mathbf{\Lambda}. \tag{3.133}$$

This Equation is called the right eigenvalue problem of matrix $\mathbf{A}$ [57, 58], since the columns of $\mathbf{\Phi}_r$ are the right eigenvectors of matrix $\mathbf{A}$.
Similarly, the left eigenvalue problem of matrix $\mathbf{A}$ is defined as:

$$\mathbf{\Psi}^H\mathbf{A} = \mathbf{\Lambda}\mathbf{\Psi}^H \tag{3.134}$$

where each row of $\mathbf{\Psi}^H$ is one left eigenvector of $\mathbf{A}$. The exponent $(\cdot)^H$ denotes the Hermitian transpose, since the eigenvectors are complex.
The left and right eigenvectors can be normalized so as to satisfy the bi-orthogonality relation

$$\mathbf{\Psi}^H = \mathbf{\Phi}_r^{-1} \qquad \text{and} \qquad \mathbf{\Psi}^H\mathbf{\Phi}_r = \mathbf{I}. \tag{3.135}$$

Furthermore, matrix $\mathbf{A}$ can be diagonalized using the left and right eigenvectors as follows:

$$\mathbf{A} = \mathbf{\Phi}_r\mathbf{\Lambda}\mathbf{\Psi}^H. \tag{3.136}$$

However, this condition is not guaranteed when repeated eigenvalues are present, since the associated eigenvectors can not form a complete independent basis.

The interest of both right and left eigenvalue problem formulations is described in Section 3.6, for the modes tracking method.

3.4 Stability analysis overview

Once the eigenvalues of the system are obtained, they are used to conduct a stability analysis of the system.

An eigenvector $\boldsymbol{\phi}_r$ associated with the eigenvalue $\lambda = \sigma + i\,\omega$ gives a modal solution $\mathbf{q}(t)$ of the form [59]:

$$\mathbf{q}(t) \;=\; \underbrace{\boldsymbol{\phi_r}}_{\text{shape}}\;\underbrace{\mathrm{e}^{\sigma\ t}}_{\text{stability}}\;\underbrace{\mathrm{e}^{i\ \omega\ t}}_{\text{oscillatory motion}}\quad. \tag{3.137}$$

Therefore, the solution is governed by two contributions. On the one hand, the exponential $\mathrm{e}^{\sigma\ t}$ determines the stability of the response. If σ is positive, this term grows as time t increases, and the mode is unstable. If σ is negative, the response decreases with time, and the corresponding mode is stable.

On the other hand, the term $\mathrm{e}^{i\ \omega\ t}$ determines the oscillatory nature of the mode. Additionally, the eigenvector $\boldsymbol{\phi}_r$ gives information about the shape of the motion, because it contains the relative amplitudes, as well as the phase differences between each degree of freedom of the system.

If the time response of a particular degree of freedom ϕ_i is required, the corresponding component of the eigenvector $\boldsymbol{\phi}_r$ can be extracted. This component is denoted by ϕ_i. Applied to Equation 3.137, it gives:

$$\phi_i(t) \;=\; \phi_i\ \mathrm{e}^{\sigma\ t}\ \mathrm{e}^{i\ \omega\ t}. \tag{3.138}$$

As the eigenvector $\boldsymbol{\phi}_r$ is complex, the component ϕ_i is also a complex number, which can be written as:

$$\phi_i \;=\; A_i\ \mathrm{e}^{i\ \varphi_i}, \tag{3.139}$$

where $A_i \;=\; |\phi_i|$ is the amplitude of the complex number, and $\varphi_i \;=\; \arg\phi_i$ is its phase.

Therefore, 3.138 and 3.139 are combined to give the time response of the considered degree of freedom, written as:

$$\phi_i(t) \;=\; A_i\ \mathrm{e}^{i\ \varphi_i}\ \mathrm{e}^{\sigma\ t}\ \mathrm{e}^{i\ \omega\ t} \;=\; A_i\ \mathrm{e}^{\sigma\ t}\ \mathrm{e}^{i(\omega\ t\ +\ \varphi_i)}. \tag{3.140}$$

Since the physical response of the degree of freedom is real, the real part of 3.140 is retained, leading to:

$$\phi_i(t) \;=\; \underbrace{\mathrm{e}^{\sigma\ t}}_{\text{stability}}\;\underbrace{A_i\ \cos\left(\omega\ t\ +\ \varphi_i\right)}_{\text{oscillatory shape}}. \tag{3.141}$$

This development is useful for whirl flutter mode identification described in Section 3.5, where the considered components ϕ_i refer to the pylon pitch and yaw degrees of freedom θ and ψ, respectively.

3.5 Whirl flutter mode identification

Once the eigenvectors are obtained, it is necessary to identify both whirl flutter modes, if they exist, in order to conduct a proper whirl flutter analysis. The whirl flutter physical mechanism is explained in Section 2.1. Therefore, the identification criteria are based on the physical and dynamic characteristics of whirl flutter modes.

Firstly, the whirling nature of the mode is characterized. If both pitch K_θ and yaw K_ψ stiffnesses are assumed to be equal, the mode theoretically precesses as perfect circular motion. This mode circular motion can be identified through the phase difference Δ and the amplitude ratio R between the yaw ψ and pitch θ degrees of freedom. Effectively, for a circular motion of the pylon, the phase difference should be equal to $\Delta = \pm 90°$ and the amplitudes of the pitch and yaw components should be equal. With the definition

$$R = \frac{|\psi|}{|\theta| + |\psi|}, \tag{3.142}$$

R should be equal to 0.5.

Additionally, a phase difference equal to $\pm 90°$ means that, when one degree of freedom reaches its maximum amplitude, the other is zero, and inversely.

The phase difference between both degrees of freedom is defined as:

$$\Delta = \arg\psi - \arg\theta, \tag{3.143}$$

where the phases are computed from the corresponding complex components of the eigenvector. For instance, $\arg\psi = \arctan\left(\frac{\omega_i}{\sigma_i}\right)$ and similarly for the pitch degree of freedom.

Together, these two parameters characterize the whirling motion of the mode. The sign of Δ, combined with the propeller rotation direction, allows the mode to be classified as either a backward or forward whirling mode.

Secondly, the identified whirling modes must become unstable as the free-stream velocity V increases in order to classify them as whirl flutter modes. Therefore, if the real part of the corresponding eigenvalue increases and crosses the zero line at a particular velocity, called the critical speed V_{crit}, the aerodynamic effects have a destabilizing influence on the mode.

3.5.1 Aerodynamic influence on a mode

The aerodynamic influence on a mode can be analysed using an energetic approach. According to May M. et al., the global aerodynamic work over one cycle, i.e. from $t = 0$ to $t = T$ determines the direction of the energy exchange between the free-stream and the structure. This work, denoted by W_a, is defined as the work exerted by the structure on the free-stream over one period.

In particular, if W_a is positive, the energy is transferred from the free-stream to the structure, which has a destabilizing effect. Inversely, if W_a is negative, energy is transferred from the structure to the flow, which has a stabilizing effect [60]. The aerodynamic work associated with mode i is mathematically given by [61]:

$$W_a \;=\; \int_0^T \dot{\boldsymbol{\phi}}_i^T(t)\; \mathbf{F}_a^i(t)\; dt, \tag{3.144}$$

where $\mathbf{F}_a^i(t)$ is the aerodynamic forces vector associated with the mode i. Based on the equations of motion defined in Equation 3.87, this vector is given by:

$$\mathbf{F}_a^i(t) \;=\; -\mathbf{C}_a(t)\;\dot{\boldsymbol{\phi}}_i(t) \;-\; \mathbf{K}_a\;\boldsymbol{\phi}_i(t), \tag{3.145}$$

where $\mathbf{C}_a(t)$ and $\mathbf{K}_a(t)$ are the aerodynamic damping and stiffness matrices after the MBC transformation.

Additionally, the mean power of the aerodynamic forces, denoted by P_a, exerted on the mode is equal to [62]:

$$P_a \;=\; \frac{W_a}{T}. \tag{3.146}$$

3.6 Mode tracking method

When the evolution of a mode is studied with respect to a given parameter, it is essential to track the same mode over the entire range of analysis. Therefore, when parameters, such as free-stream velocity or pitch and yaw stiffnesses, are varied, mode tracking becomes one of the main challenges.

Indeed, over certain parameter ranges, several mode shapes and natural frequencies can evolve significantly and even cross each other. As a result, a robust mode tracking procedure is required to compare modal quantities consistently from one parameter value to another. An incorrect mode identification would lead to non-physical results.

The modal assurance criterion (MAC) between the right eigenvectors of two modes, $\boldsymbol{\phi}_i$ and $\boldsymbol{\phi}_j$, is defined as [63]:

$$\mathrm{MAC}\left(\boldsymbol{\phi}_i, \boldsymbol{\phi}_j\right) \;=\; \frac{\left|\boldsymbol{\phi}_i^H \boldsymbol{\phi}_j\right|^2}{\left(\boldsymbol{\phi}_i^H \boldsymbol{\phi}_i\right)\left(\boldsymbol{\phi}_j^H \boldsymbol{\phi}_j\right)}. \tag{3.147}$$

It can be used to quantify the similarity between mode shapes and thus perform mode tracking. Nevertheless, this approach presents several limitations when applied to aeroelastic systems. Particularly, small parameter increments are generally required to ensure accurate mode tracking. Additionally, right eigenvectors can lose orthogonality as the system approaches the critical speed, i.e. the speed above which the considered mode becomes unstable [58].

Therefore, a more robust approach is used in this thesis. This method, presented by Xiaochen

Hang and Qingguo Fei, relies on both left and right eigenvectors [58]. Indeed, their bi-orthogonal relation remains valid near the critical speed, as long as the parameter increment remains reasonable. Therefore, to track the modes between different parameter values, the bi-orthogonality relation given in Equation 3.135 is used.

Considering two consecutive states i and $i+1$, an eigendecomposition of the state-space matrix A can be performed. Thus, for both parameter states, Equation 3.136 becomes:

$$\mathbf{A}_i \;=\; \mathbf{\Phi}_{r,i}\ \mathbf{\Lambda}_i\ \mathbf{\Psi}_i^H \qquad \text{and} \qquad \mathbf{A}_{i+1} \;=\; \mathbf{\Phi}_{r,i+1}\ \mathbf{\Lambda}_{i+1}\ \mathbf{\Psi}_{i+1}^H, \tag{3.148}$$

with $\mathbf{\Phi}_r$ the matrix gathering the right eigenvectors of $\mathbf{A}$, whereas $\mathbf{\Psi}^H$ gathers the left eigenvectors. The modes tracking is performed using two orthogonality-check matrices, denoted by $\mathbf{S}$ and $\bar{\mathbf{S}}$. Between two consecutive parameter states i and $i+1$, these matrices must be diagonally dominant to ensure robust mode tracking. They are defined as:

$$\mathbf{S}_{i,i+1} \;=\; \mathbf{\Psi}_i^H\ \mathbf{\Phi}_{r,i+1} \qquad \text{and} \qquad \bar{\mathbf{S}}_{i,i+1} \;=\; \mathbf{\Phi}_{r,i}^H\ \mathbf{\Psi}_{i+1}. \tag{3.149}$$

It is important to note that, unlike the MAC matrix of Equation 3.147, the orthogonality-check matrices are not necessarily identity matrices, by definition.
This mode-tracking algorithm requires the computation of both the right and left eigenvectors at each parameter step. The workflow of the method is defined as follows.

First, at increment i, the left eigenvectors $\mathbf{\Psi}_i$ of matrix A_i are classically computed. The tracking method requires the modes to be initially sorted. For clarity, they are first sorted by increasing oscillation frequency.
Then, right eigenvectors $\mathbf{\Phi}_{r,i+1}$ of $\mathbf{A}_{i+1}$ are computed and mode identification can be performed. The columns of matrix $\mathbf{\Phi}_{r,i+1}$ are rearranged so that the orthogonality-check matrix $\mathbf{S}_{i,i+1}$ is diagonally dominant.
To track the mode at the next parameter increment $i+2$, the obtained reordered right eigenvectors matrix $\mathbf{\Phi}_{r,i+1}$ is used. Left eigenvectors $\mathbf{\Psi}_{i+2}$ of matrix $\mathbf{A}_{i+2}$ are computed, and the newly computed eigenvector matrix is reordered so that the corresponding orthogonality-check matrix becomes diagonally dominant.
Once all the products $\mathbf{\Psi}_i^H\ \mathbf{\Phi}_{r,i+1}$ or $\mathbf{\Phi}_{r,i}\ \mathbf{\Psi}_{i+1}^H$ have been computed for all modes, the columns of the newly computed eigenvector matrix, either $\mathbf{\Phi}_{r,i+1}$ or $\mathbf{\Psi}_{i+1}^H$, are then reordered to maximize the diagonal dominance of the associated orthogonality-check matrix. Therefore, the quality of the mode tracking is evaluated by analysing both $\mathbf{S}$ and $\bar{\mathbf{S}}$ matrices. Two indices can be defined for each eigen-

vector to quantify its similarity with the other modes.

The first one is the row index n_r, defined as the ratio between the diagonal term, associated with the tracked mode, the largest off-diagonal term in the corresponding row. It indicates if the identified mode is more strongly correlated with the tracked mode or with another mode at the new parameter step. The second one, called the column index n_c, is defined as the ratio between the diagonal term and the largest off-diagonal term in the corresponding column. A low column index would indicate that another previous mode is more strongly correlated with the identified mode than the tracked one. Therefore, high quality mode tracking requires both indices to remain sufficiently high, as follows:

$$n_r >> 1 \qquad \text{and} \qquad n_c >> 1. \tag{3.150}$$

Additionally, the frequency difference between two parameter increments must be considered. Indeed, if the increment is not significantly large, the frequency of a given mode is expected to vary only slightly between two successive states. Hence, the relative frequency difference between two successive states is defined as:

$$\left| \frac{f_i - f_{i+1}}{f_i} \right| \cdot 100 \ [\%]. \tag{3.151}$$

The mode association is obtained by solving an optimal matching problem based on a cost matrix constructed from the corresponding orthogonality-check matrix. This cost matrix is defined as the opposite of the absolute values of the orthogonality-check coefficients, so that minimizing the cost is equivalent to maximizing the modal correlation.

If the relative frequency difference between two candidate modes is higher than 20%, a large positive penalty is assigned to the corresponding cost matrix element. This allows this mode pair to be excluded from the assignment process. This assignment problem is solved using a modified version of the Jonker–Volgenant algorithm [64, 65].

In this thesis, the varied physical parameters are the free-stream velocity, as well as pitch and yaw stiffnesses. The nominal parameter increment is defined as 1. In parameter ranges where mode veering occurs, i.e. where the row and column indices are not significantly greater than one, the velocity step is adjusted in order to ensure high-quality mode tracking. This is further discussed in Chapter 4.

3.7 Blade deformation visualization

The visualization of blade deformations associated with a whirl flutter mode is useful for investigating the interaction between pylon and blade motions. These deformations are analysed in the R_2 frame defined in Figure 3.2, i.e. the frame moving with the propeller centre. Therefore, several mathematical operations are required to obtain the blade deformations from the mode shapes computed with the analytical method.

First, MBC transformation changes the generalized coordinate vector from the blade rotating-frame coordinates $\mathbf{y}$ to the multi-blade coordinates $\boldsymbol{\xi}$, as explained in Section 3.1.11. As a result, the physical meaning of the coordinates is modified. Before being projected onto the fixed frame R_2, the blade deformations must first be expressed in the undeformed rotating frame R_{b_n} of each blade. Therefore, the initial generalized coordinates have to be recovered. This is achieved using the inverse MBC transformation:

$$\mathbf{y} \ = \ \mathbf{T}(t)\ \boldsymbol{\xi}, \tag{3.152}$$

with matrix $\mathbf{T}(t)$ the transformation matrix defined in 3.107.

Once the inverse transformation has been performed, the components of the mode can be interpreted in a classical way, since the coordinates are now expressed in the blade undeformed frame R_{b_n}. Thus, radial distributions of the blade deformations can be recovered through the Rayleigh-Ritz approximation, defined in Equations 3.10, 3.11, 3.12 and 3.13 for the in-plane bending, traction, out-of-plane bending and torsion, respectively.
Therefore, the obtained $h(r)$, $w(r)$, $v(r)$ and $t(r)$ distributions are written in the blade undeformed frame R_{b_n} and must be projected into the R_2 frame to facilitate the interpretation of the blade deformations.

For clarity purposes, each blade is represented by a line extending from its root to its tip. In the undeformed blade frame R_{b_n}, a point located at the radial position r on the undeformed blade is mathematically expressed as:

$$\begin{pmatrix} x^0_{b_n} \\ y^0_{b_n} \\ z^0_{b_n} \end{pmatrix} = \begin{pmatrix} 0 \\ r \\ 0 \end{pmatrix}, \tag{3.153}$$

since the $\mathbf{y}_{b_n}$ axis corresponds to the longitudinal direction of the blade. This is illustrated in Figure 3.11, where the undeformed and deformed blades are represented in both frames R_{b_n} and R_2.

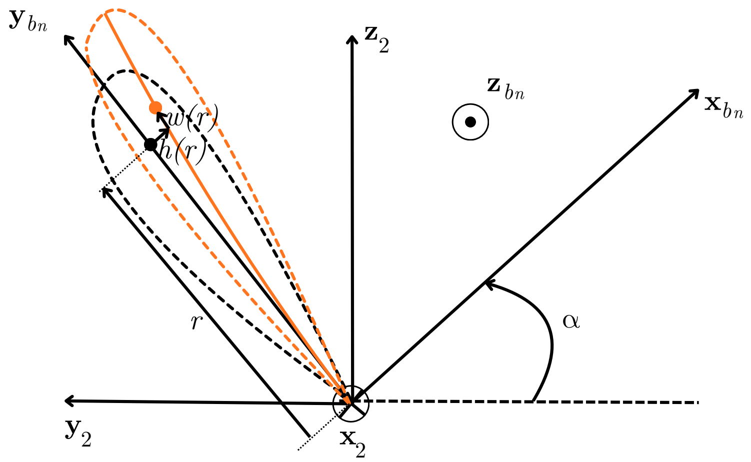

Figure 3.11: Undeformed (in black) and deformed (in orange) blades represented in both frames R_{b_n} and R_2. The blades are shown for $r_0 = 0$ for drawing clarity.

Traction simply corresponds to an elongation of the blade in the $\mathbf{y}_{b_n}-$direction. Therefore, the initial radial position r becomes $r + w(r)$, meaning that $w(r)$ represents the radial deformation. Concerning the out-of-plane bending, it corresponds to the deformation normal to the undeformed blade plane which is represented in Figure 3.11. It is therefore represented by the component $v(r)$ in the $\mathbf{z}_{b_n}-$direction at the radial location r.

Similarly, the in-plane bending is defined as a deformation perpendicular to the blade radial direction $\mathbf{y}_{b_n}$, but remaining in the undeformed propeller plane. Hence, it corresponds to the component $h(r)$ in the $\mathbf{x}_{b_n}$-direction at the radial location r.

As a summary, the point initially located at $(0,\ r,\ 0)^T$ in the undeformed blade frame R_{b_n} becomes, when blade deformation is taken into account:

$$\begin{pmatrix} x^d_{b_n} \\ y^d_{b_n} \\ z^d_{b_n} \end{pmatrix} = \begin{pmatrix} h(r) \\ r + w(r) \\ v(r) \end{pmatrix}. \tag{3.154}$$

This describes properly, in the undeformed frame R_{b_n}, the coordinates of all points of the deformed blade. Since the blade deformation must be finally represented in the R_2 frame, matrix $\mathbf{R}_{R_{b_n}\to R_2}$, which expresses the basis vectors of frame R_{b_n} in frame R_2 must be used. This matrix is defined in 3.30.

As a result, it comes:

$$\begin{pmatrix} x^d_2(r) \\ y^d_2(r) \\ z^d_2(r) \end{pmatrix} = \mathbf{R}_{R_{b_n}\to R_2} \begin{pmatrix} x^d_{b_n}(r) \\ y^d_{b_n}(r) \\ z^d_{b_n}(r) \end{pmatrix} = \begin{pmatrix} 0 & 0 & -1 \\ -\cos\alpha & \sin\alpha & 0 \\ \sin\alpha & \cos\alpha & 0 \end{pmatrix} \begin{pmatrix} h(r) \\ r + w(r) \\ v(r) \end{pmatrix}. \tag{3.155}$$

In equation form, it gives:

$$\begin{cases} x_2^d(r) &= -v(r) \\ y_2^d(r) &= -h(r)\,\cos\alpha + (r + w(r))\,\sin\alpha \\ z_2^d(r) &= h(r)\,\sin\alpha + (r + w(r))\,\cos\alpha \end{cases}, \tag{3.156}$$

and the deformed blades can then be easily represented in the frame attached to the propeller centre, denoted by R_2. As a reminder, $\alpha(t) = (n - 1)\,\beta + \Omega\,t$ of blade n is the blade azimuthal angle at time t, defined in 3.26.

Furthermore, the torsional deformation is directly obtained from the radial distribution $\theta_t(r)$. Unlike bending and traction displacements, it does not require a geometrical reconstruction of the blade centreline, since it is already expressed as a rotation angle along the blade span.

3.8 Cantilever beam static deflection

In the system configurations defined in Chapter 4, the pylon is loaded at its tip, mainly due to the presence of the propeller and the motor. As a result, it can experience a static deformation, which is not desirable for an actual experimental setup. Indeed, such a deformation would induce a static misalignment of the propeller plane with respect to its nominal orientation, therefore modifying the operating conditions of the experiment.
Under the linear Euler-Bernoulli beam assumption, a first approximation of the beam tip deflection δ and rotation θ can be obtained. Both quantities are given by:

$$\delta = \frac{FL^3}{3EI} + \frac{M_0L^2}{2EI} \qquad \text{and} \qquad \theta = \frac{FL^2}{2EI} + \frac{M_0L}{EI}. \tag{3.157}$$

All the analytical developments are described in Appendix C.

Chapter 4. Analytical modelling of the whirl flutter demonstrator

Once the analytical method has been correctly implemented, it can be used to perform the preliminary design of the small-scale whirl flutter demonstrator.
In this chapter, two different system configurations are first presented. They are then compared in terms of their advantages and drawbacks in order to assess their feasibility and highlight their differences.

The first step is the selection of a suitable propeller, which is common to both configurations. Then, the remaining geometrical parameters are discussed.
Due to experimental constraints, all the results presented in this chapter are computed for a propeller rotational speed Ω of 2000 rpm. At this operating condition, the maximum free-stream velocity that can be considered is 13 m/s, as shown in Table D.2 of Appendix D. This constitutes one limitation of the study.
Furthermore, all results are obtained assuming a structural damping ratio between 0.5% and 2% for both backward and forward whirl modes. This range is selected to provide a realistic representation of the damping levels expected in the experimental setup.
Moreover, the number of shape functions retained in the model is determined through a convergence analysis of the frequencies associated with the relevant backward and forward whirling modes. This leads to the following retained numbers of shape functions:

$$\begin{cases} N_h &= 6 \\ N_w &= 4 \\ N_v &= 6 \\ N_t &= 5 \end{cases} . \tag{4.1}$$

As a reminder, N_h, N_w, N_v, N_t denote the number of shape functions considered in the Rayleigh-Ritz approximation for in-plane bending, traction, out-of-plane bending, and torsion, respectively. This is described in detail in Section 3.1.4.

Additionally, Table 4.1 lists the general quantities used in all computations. The motor mass includes the motor and all other components located at the end of the pylon, excluding the propeller.

These components are described in Chapter 5.

Parameter	Value
Air density ρ_{air}	1.225 kg/m^3
Propeller rotational speed Ω	2000 rpm
Motor mass	0.8 kg
C_{tract}	1 N.s/m^2
C_{flex}	1.75 N.s/m^2
C_{tor}	0.2 N.s

Table 4.1: General definition of some parameters used for all the computations.

Concerning structural damping, only the pitch C_θ and yaw C_ψ coefficients differ between the two configurations.

4.1 Propeller description

A real propeller can be selected for the experimental setup. Its geometrical parameters, as well as performance data for several rotational and free-stream velocities are integrated into the analytical model, in order to assess the whirl flutter stability behaviour of the system.
In this section, the propeller geometry and performance data are presented, together with information regarding its manufacturing process.

The selected propeller is the APC 15.75x13-3, manufactured by APC Propellers [66]. Its main characteristics are presented in Sections 4.1.1 and 4.1.2.
As a general comment, *15.75* denotes the propeller diameter in inches, corresponding approximately to 400 mm, whereas *13* denotes the propeller pitch, also in inches. This corresponds to 330 mm. This means that the propeller would advance by 330 mm during one complete revolution. This three-bladed propeller is shown in Figure 4.1.

Figure 4.1: Selected APC 15.75x13-3 propeller.

The blades are identical and equally distributed over the propeller circumference. This leads to β, defined in Equation 3.27, being equal to $\frac{2\pi}{3}$.

APC Propellers is an American company based in California and founded in 1989. It manufactures a wide range of propellers, including multi-rotors, thin-electric, sport, aerobatic and racing propellers. The available diameters range from 102 mm to 686 mm, with different geometrical and aerodynamics characteristics. The company also provides geometry and performance data for its propellers, which is particularly useful for the present preliminary design [66].

The APC 15.75x13-3 propeller is selected as a compromise between geometry, blade flexibility and aerodynamic loading. Its relatively large diameter leads to more flexible blades than smaller propellers with similar design, while keeping the aerodynamic loading sufficiently significant for the present experimental setup.
Moreover, the data provided by the manufacturer allow the propeller geometry and performance to be directly integrated into the analytical model.

4.1.1 Propeller geometrical characteristics

The 15.75x13-3 APC propeller is uniformly made of a nylon composite. The relevant physical properties of this material are given in Table 4.2.

Parameter	Value
Young modulus E_b	19.3 GPa
Poisson ratio ν_b	0.34
Shear modulus G_b	7.2 GPa
Density ρ_b	1700 kg/m^3

Table 4.2: Relevant physical properties of the nylon composite propeller material required for the analytical computations [66].

The blade airfoil is the CLARK-Y profile, which is commonly used for this type of propeller. This airfoil profile is represented in Figure 4.2.

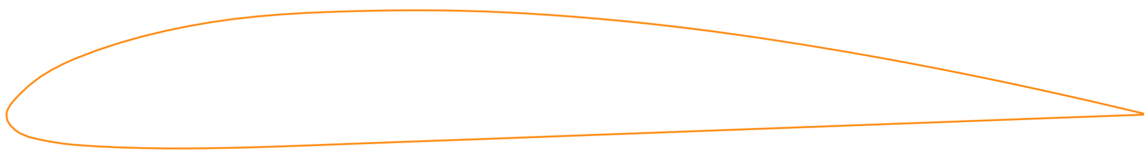

Figure 4.2: CLARK-Y airfoil profile of the propeller blades [67].

Furthermore, the main geometrical parameters of the selected propeller are summarized in Table 4.3.

Parameter	Value
Radius	0.2 m
Hub internal diameter	7.87 mm
Hub external diameter	38.1 mm
Hub thickness	16.25 mm
Mass	120 g
Volume	$7 \cdot 10^{-5}$ m^3
Pitch	330 mm

Table 4.3: Main geometrical parameters of the APC 15.75x13-3 propeller.

Figure 4.3 shows the radial distributions of the blade cross-sectional area, chord, twist angle and maximum thickness. The twist angle represented in Figure 4.3b denotes the angle measured between the local chord line and a reference flat bottom surface.
As a comment, the radial position is measured from the blade root, not from the propeller centre. In this work, the blade root is assumed to be located at the external hub radius. Therefore, the chord, twist angle, cross-sectional area, and maximum thickness are expressed as functions of the radial position along the blade.

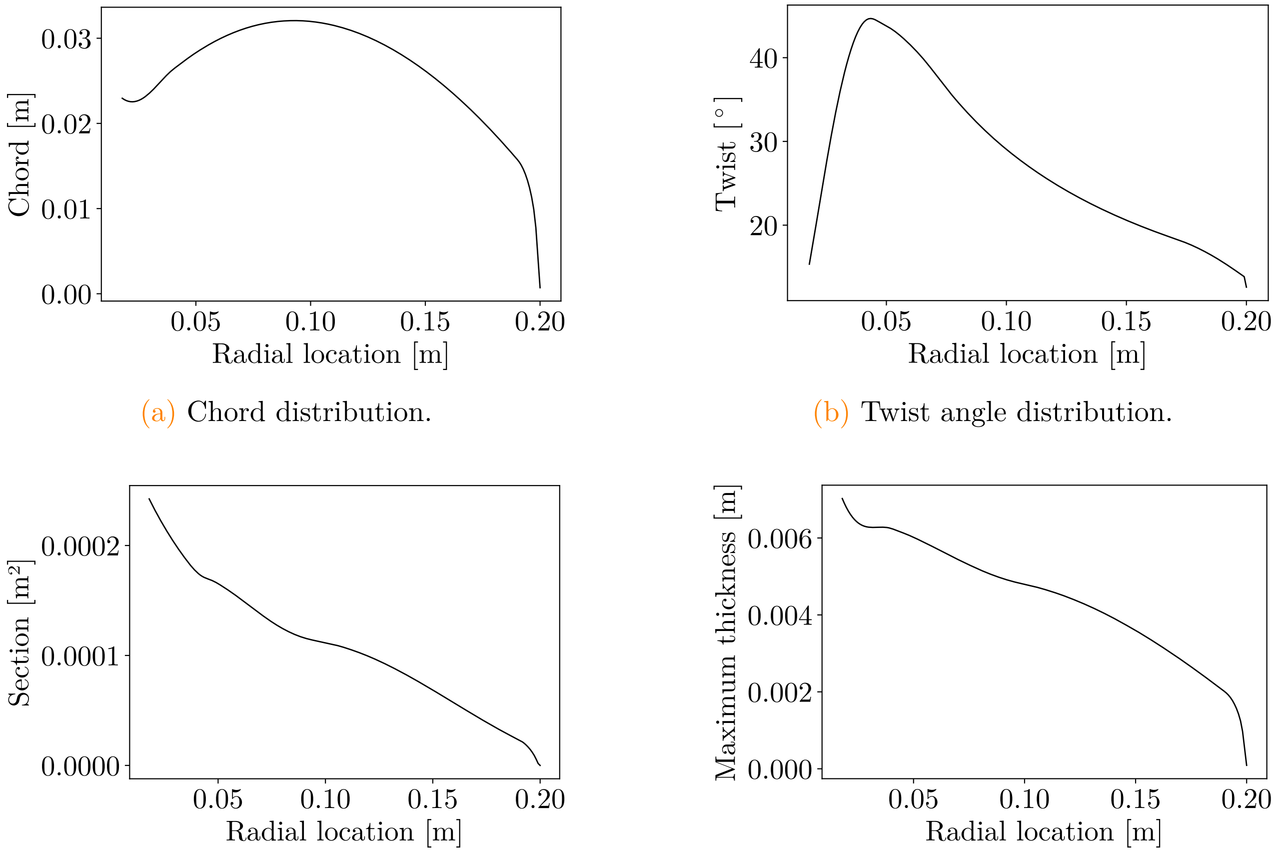

(a) Chord distribution.

(b) Twist angle distribution.

(c) Cross-sectional area distribution.

(d) Maximum thickness distribution.

Figure 4.3: Radial distributions of chord, twist angle, cross-sectional area, and maximum thickness for one blade of the selected APC 15.75x13-3 propeller.

From these geometrical data, the polar and transverse moments of inertia of the propeller, denoted by J_1 and J_2, respectively, can be computed. They are previously defined in Equations 3.50 and 3.51, respectively. The resulting propeller moments of inertia, expressed at the propeller centre, are provided in Table 4.4.

Inertia	Value
Polar moment of inertia J_1, expressed at the propeller centre	880.01 kg.mm^2
Transverse moment of inertia J_2, expressed at the propeller centre	446.32 kg.mm^2

Table 4.4: Polar and transverse moments of inertia J_1 and J_2 of the selected propeller, expressed at the propeller centre.

Additionally, the radial distributions of the second moments of area of the blade beam section $I_x(r)$, $I_y(r)$ and $I_z(r)$ are shown in Figure 4.4. As a reminder, these quantities are defined in Equations 3.53 and 3.54.

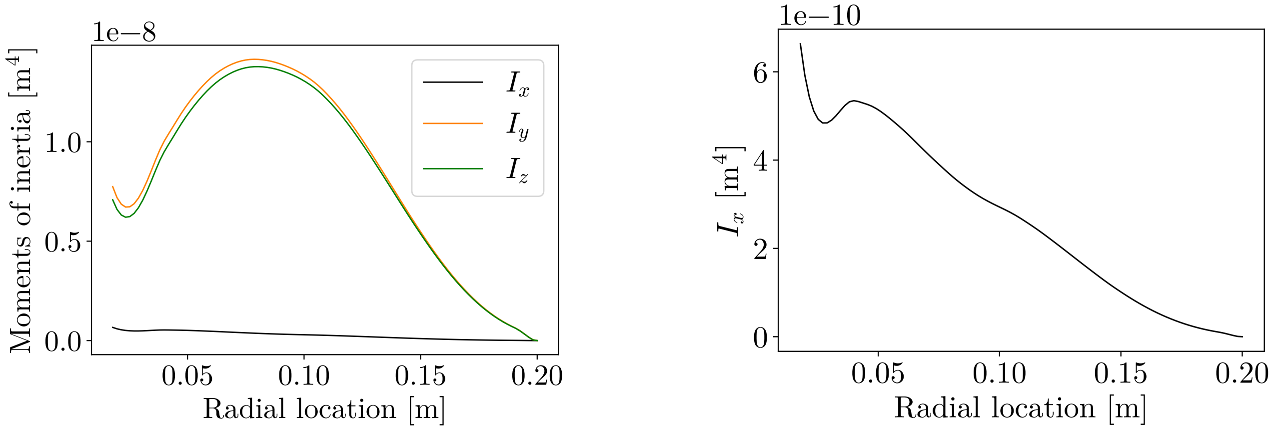

(a) $I_x(r)$, $I_y(r)$ and $I_z(r)$ distributions.

(b) $I_x(r)$ distribution.

Figure 4.4: Radial distributions of the second moments of area $I_x(r)$, $I_y(r)$ and $I_z(r)$ of the blade beam section, with a detailed view of I_x.

4.1.2 Propeller performance

APC Propellers uses its own computational software to provide propeller performance data. In particular, these data are based on vortex theory and are obtained from the actual geometry of the propeller. The thrust coefficient, torque coefficient, Mach number at the propeller tip, thrust, torque and Reynolds number at 75% of the span are provided for each 1000 rpm increment. The corresponding free-stream velocity values are limited to the operating range of the propeller for each rotational speed. The corresponding propeller performances for $\Omega = 1000$ rpm and $\Omega = 2000$ rpm are given in Appendix D.

Furthermore, the nominal direction of rotation of the APC 15.75x13-3 propeller is right-hand rotation. According to the usual propeller convention, this means that the propeller rotates counter-clockwise when viewed from the front.

In Figures 4.5a and 4.5b, the thrust and power coefficients are represented as functions of the advance ratio, which is defined as [54]:

$$J = \frac{V}{nD}, \tag{4.2}$$

with V the free-stream velocity, n the rotational speed in rev/s, and D the propeller diameter.

On the one hand, the thrust coefficient C_T decreases with increasing advance ratio J. For a fixed rotational speed, this is due to the reduction of the relative blade angle of attack. Indeed, as the advance ratio increases, the ratio of the axial velocity and the tangential velocity becomes larger. Hence, the relative blade angle of attack decreases, leading to a reduction in blade lift, and therefore in thrust.

On the other hand, the power coefficient C_P slightly increases until $J = 0.4$, before decreasing until

$J = 1$.

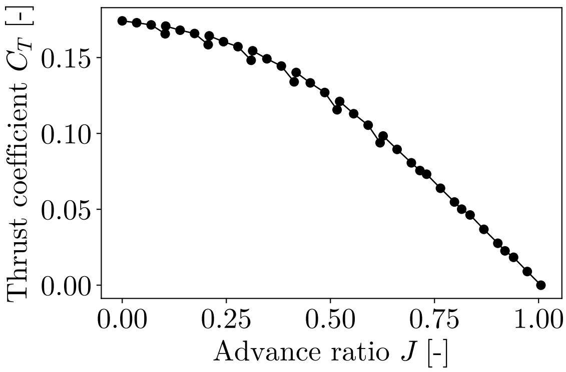

(a) Thrust coefficient C_T.

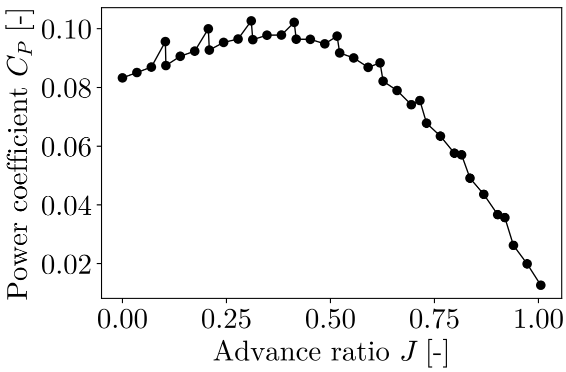

(b) Power coefficient C_P.

Figure 4.5: Thrust and power coefficients of the APC 15.75x13-3 propeller, denoted by C_T and C_P, respectively, as functions of the advance ratio J.

Finally, the torque required to rotate the propeller at given free-stream velocity and rotational speed conditions is also important for the experimental setup. It is considered in the motor selection, since the motor must be able to provide the required torque over the considered operating range. The corresponding torque values are given in Appendix D, while the motor selection is discussed in Section 5.3.

Airfoil aerodynamic performance

As discussed in Sections 3.1.9 and 3.2.2, blade section lift and drag coefficients, as well as lift curve slope must be extracted for different angles of attack and Reynolds numbers for the computation of the propeller aerodynamic matrices.

To do so, data are extracted from the Airfoil Tools software [67]. This software provides coefficient values obtained using XFOIL.

Created by Mark Drela in 1986, XFOIL is used for the study of isolated subsonic airfoil profiles. For different Mach and Reynolds numbers, it can provide lift and drag predictions, in addition to other aerodynamic parameters that are not required in this thesis. XFOIL is based on a viscous–inviscid interaction approach. The inviscid flow is computed using a linear-vorticity panel method, while viscous effects are modelled with an integral boundary-layer formulation. The lift coefficient is obtained from pressure integration, whereas the drag coefficient is computed from the wake momentum thickness using the Squire-Young formula [68].

The coefficients are extracted for different Reynolds numbers, and they are then interpolated to obtain the relevant coefficient values at each considered Reynolds number. Moreover, interpolation is also performed with respect to the angle of attack. For instance, the airfoil polar at Re $=$ 50000 is given in Figure 4.6.

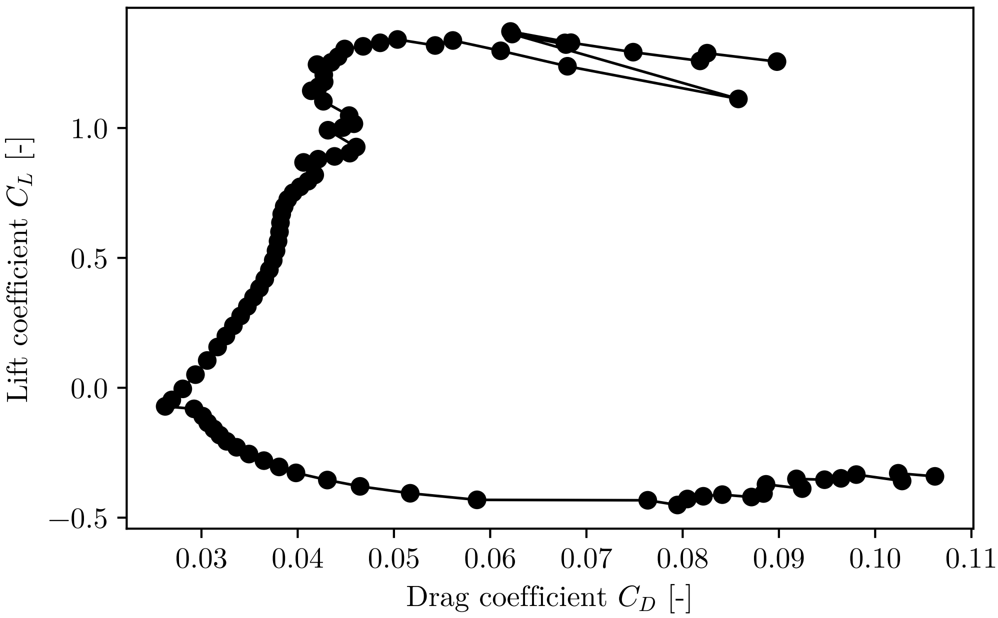

Figure 4.6: Lift coefficient C_L as a function of the drag coefficient C_D for angles of attack ranging from -8.5° to 14.75°, considering a Reynolds number Re $= 5 \cdot 10^4$ [67].

The irregular behaviour observed around $C_D = 0.09$ and $C_L = 1.1$ can be due to a loss of accuracy in the polar prediction of the solver, possibly associated with the approach to airfoil stall. This corresponds approximately to angles of attack higher than 11.5° [67]. Such behaviour is consistent with the known limitations of XFOIL when dealing with separated flow and post-stall conditions. However, this range of angles of attack is not reached in the present analytical computations and therefore does not affect the results.

Additionally, for all the considered Reynolds numbers, the zero-lift angle of the airfoil α_0, defined in 3.124, is approximated as 4° [67] and the finite blade length correction factor C_{3D}, defined in Equation A.6, is equal to 0.77.

Furthermore, the lift-curve slope of the blade section is identified from the evolution of the lift coefficient as a function of the angle of attack for a given Reynolds number. The static pitching moment of a blade section, m_0, introduced in Equation A.8, is computed from the moment coefficient C_m given by XFOIL. Both quantities are related as [69]:

$$m_0(r) \;=\; C_M(r)\, \frac{1}{2}\, \rho_a\, u^2(r)\, c^2(r). \tag{4.3}$$

4.2 Introduction of the configurations

As previously mentioned, two configurations are analytically investigated. The first one is the flexible pylon configuration, while the second one is the rigid pylon configuration. They are both described in Sections 4.3 and 4.4, respectively. The main conceptual difference between the two configurations lies in the origin of the system flexibility, which is provided either by the pylon itself or by linear springs, depending on the considered case.

In Section 3.1, where the analytical method is theoretically described, two stiffness quantities are introduced for the pitch and yaw motions of the pylon, respectively K_θ and K_ψ. Thus, their definition will be different for both configurations.

However, some general design guidelines are common to both configurations. According to Reed, a system with equal pitch and yaw stiffness is more susceptible to whirl flutter instability [10]. Therefore, imposing symmetry in pitch and yaw stiffnesses K_θ and K_ψ is consistent with the objective of favouring the occurrence of whirl flutter.

4.2.1 Model requirements

For both configurations, the model must allow whirl flutter to occur. Therefore, in the flexible pylon configuration, the dimensions and geometry of the pylon have to be selected so that the system is flexible enough. As a reminder in the rigid pylon configuration, the required flexibility is instead introduced by the linear springs.

However, in both cases, the pylon must not experience excessive static deformation due to the mass located at its tip. For instance, the propeller and other components, described in Chapter 5, are located at the tip of the propeller.

Therefore, the static deflection and rotation angle at the pylon tip must remain limited. Otherwise, the equilibrium position would be modified, which could affect its dynamic behaviour. Excessive static deflection could induce a significant mass unbalance, potentially leading to mechanical failure of the setup in some cases. Additionally, the deflection angle at the pylon tip directly modifies the orientation of the propeller plane, which could introduce unwanted aerodynamic effects.

These quantities, referred to as the static tip deflection δ_{tip} and static tip rotation angle θ_{tip}, are computed from 3.157 in Section 3.8 for a cantilever beam loaded at its tip.

In the present case, for both configurations, the propeller is assumed to be located at a distance L_{motor} of the pylon tip, as seen in Figure 4.7, where L_{motor} denotes the motor length.

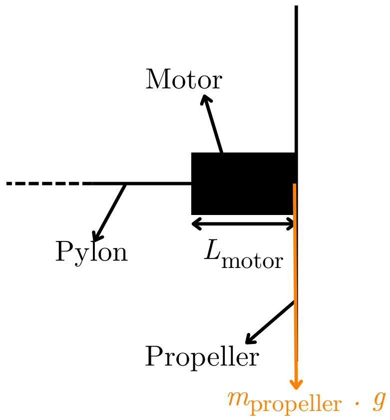

Figure 4.7: Simplified model configuration with the pylon, the motor and the propeller.

Hence, the moment applied at the tip of the pylon is given by:

$$M_0 = m_{propeller}\ g\ L_{motor}, \tag{4.4}$$

with $m_{propeller}$ the mass of the propeller and $g = 9.81$ m/s^2 the gravitational acceleration.
In Section 4.3 and 4.4, the static tip deflection δ_{tip} and static tip rotation angle θ_{tip} are discussed for both configurations.

Furthermore, some requirements are related to the transverse moment of inertia of the pylon J_2^p, defined in 3.39. Indeed, if this transverse moment of inertia is too high, the gyroscopic coupling induced by the rotating propeller can not be sufficient to generate a significant precession motion of the pylon. This coupling depends on the polar moment of inertia of the propeller J_1 and on its rotational speed Ω, as introduced in the expression of the propeller gyroscopic matrix in 3.55. Therefore, to compare the gyroscopic effect with the transverse inertia of the pylon, a relevant design ratio can be defined as:

$$\frac{J_1}{J_2^p}, \tag{4.5}$$

with J_1 the polar moment of inertia of the propeller.
The goal of this ratio is to provide an indication of the susceptibility of the system geometry to whirl flutter, without accounting for the propeller rotational speed. It can therefore be interpreted as a structural design indicator, giving qualitative information on the ability of the rotating propeller to induce a precession motion of the pylon.
If this ratio is significantly low, the transverse inertia of the pylon is large compared with the polar inertia of the propeller. In that case, the pylon is more difficult to set into precession, and a higher propeller rotational speed would be required for the gyroscopic coupling to become significant.

When this ratio is sufficiently high, the polar inertia of the propeller is large compared with the transverse inertia of the pylon. The gyroscopic effect induced by the propeller rotation can then more easily drive the pitch-yaw coupled motion of the pylon.

As a conclusion regarding the inertias, whirl flutter is favoured by a lightweight pylon, i.e. a small-size pylon and/or made of low-density material. If the pylon has to be flexible, as discussed in Section 4.3 for one of the two configurations, a trade-off has to be found. Indeed, in addition to a relatively low transverse inertia, the pylon has to be flexible enough. The first condition requires a compact pylon, whereas the second one rather involves a larger length, while remaining acceptable concerning the static deflection and rotation angle. Therefore, the final design results from a compromise between transverse inertia, flexibility, and static deformation constraints.

4.3 Flexible pylon model

The flexible pylon model considers a flexible pylon clamped at the pivot location. In this configuration, the pitch and yaw stiffness coefficients K_θ and K_ψ are derived directly from the pylon geometry. They are obtained from equivalent stiffness formulas for a cantilever beam such that the rotational springs introduced in the analytical method are represented by the equivalent rotational stiffnesses of the beam structure. Both beam equivalent rotational springs are given by [70]:

$$K_\theta = \frac{E_{pylon}\, I_{pylon,\theta}}{L_{pylon}} \qquad \text{and} \qquad K_\psi = \frac{E_{pylon}\, I_{pylon,\psi}}{L_{pylon}}, \tag{4.6}$$

where $E_{pylon}\, I_{pylon,\theta}$, $E_{pylon}\, I_{pylon,\psi}$ denote the pylon flexural stiffness in pitch and yaw, respectively, and L_{pylon} denotes the pylon length. These quantities are further discussed in Sections 4.3.1 and 4.3.2, dedicated to the pylon shape and material, respectively.

Furthermore, the flexible pylon configuration is schematically illustrated in Figure 4.8.

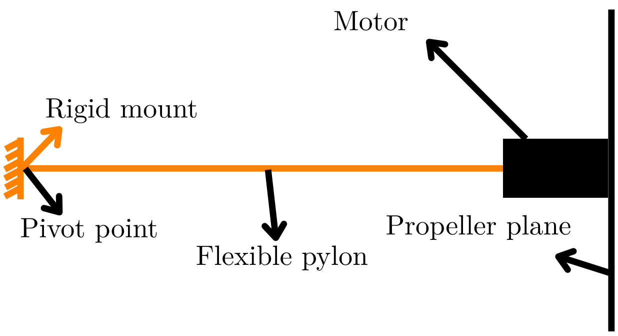

Figure 4.8: Flexible pylon analytical model.

4.3.1 Pylon shape

In order to achieve equal pitch and yaw stiffnesses K_θ and K_ψ, the pylon is chosen as a tube with circular cross-section. Indeed, for this geometry, $I_{pylon,\theta} = I_{pylon,\psi} = I_{pylon}$. This cross-section is also simple, well-known, and can be easily characterized analytically. Moreover, compared with a solid circular cylinder of the same external dimensions, the hollow circular tube reduces both the polar and transverse inertias of the pylon.

Hence, J_1^p is the polar mass moment of inertia of circular tube around its longitudinal axis, and is given by [71]:

$$J_1^p = \frac{1}{2}\, m_{pylon} \left(R_{ext}^2 + R_{int}^2\right) \tag{4.7}$$

Furthermore, the transverse mass moment of inertia of the tube-like pylon, expressed about the pivot location, i.e. about one end of the tube, is given by: as [72]:

$$J_2^p = \underbrace{\frac{1}{12}\, m_{pylon} \left(3\, \left(R_{ext}^2 + R_{int}^2\right) + L_{pylon}^2\right)}_{J_{2_a}^p} + \underbrace{m_{pylon} \left(\frac{L_{pylon}}{2}\right)^2}_{J_{2_b}^p}. \tag{4.8}$$

On the one hand, $J_{2_a}^p$ is the transverse mass moment of inertia of a hollow cylinder around its centre of mass. On the other hand, $J_{2_b}^p$ is the transport term, resulting from the parallel-axis theorem, stated in Equation 3.38. As a reminder, this theorem states that the mass moment of inertia of a body around an arbitrary axis parallel to an axis passing through its centre of mass is equal to the mass moment of inertia about the centre of mass, added to a transport term equal to the mass of the body multiplied by the square of the distance between the two axes [72].

4.3.2 Pylon material selection

Another important parameter is the pylon material. Indeed, for a given shape and given dimensions, the pylon must be sufficiently flexible, while not being excessively deformable in order to limit the static deformation induced by the tip mass. Additionally, the material should be easy to manufacture or easily available.

Therefore, the pylon material should combine a relatively low Young's modulus with a relatively low density. Based on Figure 4.9, the polymer material family appears to be a good candidate.

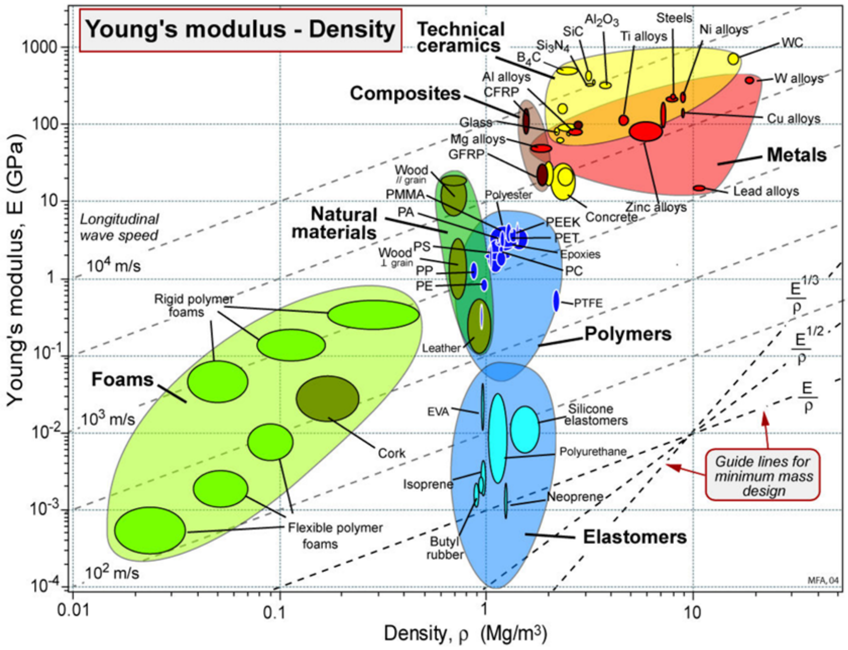

Figure 4.9: Material chart of Young's modulus E as a function of density ρ, used for pylon material selection [73].

One well-known polymer is rigid polyvinyl chloride (PVC). Depending on the sources, slightly different mechanical properties can be found. Table 4.5 lists the main properties of rigid PVC selected for this study.

Parameter	Value
Young's modulus E_{pylon}	2.8 GPa
Density ρ_{pylon}	1450 kg/m^3
Softening point	90°

Table 4.5: Young's modulus, density and softening point of the polyvinyl chloride (PVC) [74, 75].

4.3.3 Pylon dimensions

Once the pylon shape and material have been determined, its main dimensions have to be defined. These dimensions must both favour the onset of whirl flutter phenomenon and ensure an acceptable static behaviour under the mass located at the pylon tip. Moreover, the pylon must be easy to manufacture, which requires considering existing standard dimensions.
The easiest pylon geometrical parameter to vary is the pylon length. Therefore, the external diameter and wall thickness are chosen to be fixed, while only the length is varied during the stability analysis. Indeed, the pylon length is a key parameter influencing both the moments of inertia and the stiffnesses of the system.

For all the reasons stated previously, an external diameter of 10 mm with a wall thickness of

1 mm are chosen, leading to a 8 mm internal diameter. This configuration allows whirl flutter to be observed under well-defined operating conditions, while ensuring that the static tip deflection and rotation angle remain acceptable within a given range of pylon lengths.

For these geometrical parameters, Figure 4.10 shows the evolution of the pylon static tip deflection as a function of its length. Length below 0.05 m are not considered because such a setup would not be feasible in practice, and because they are not relevant from an aeroelastic point of view.

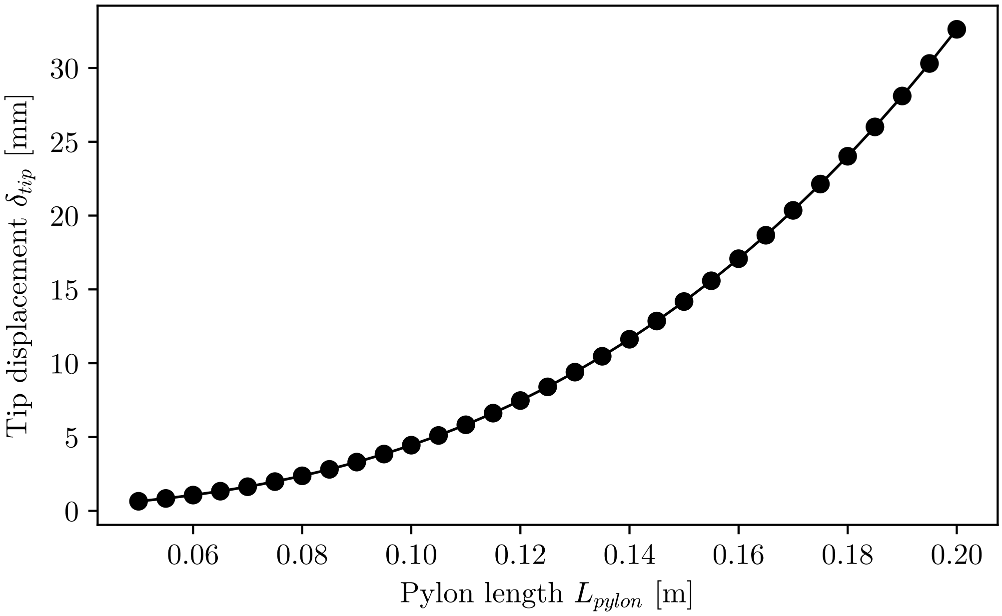

Figure 4.10: Evolution of the pylon static tip deflection δ_t as a function of its length L_{pylon} for the flexible pylon configuration, using a PVC pylon with external and internal diameters of 10 mm and 8 mm, respectively.

As expected, the pylon tip deflection increases with the pylon length, since the deflection is the sum of a contribution proportional to L^2 and another proportional to L^3, as established in Section 3.8. Additionally, the tip rotation angle can also be computed over the same length range. Figure 4.11 shows this evolution.

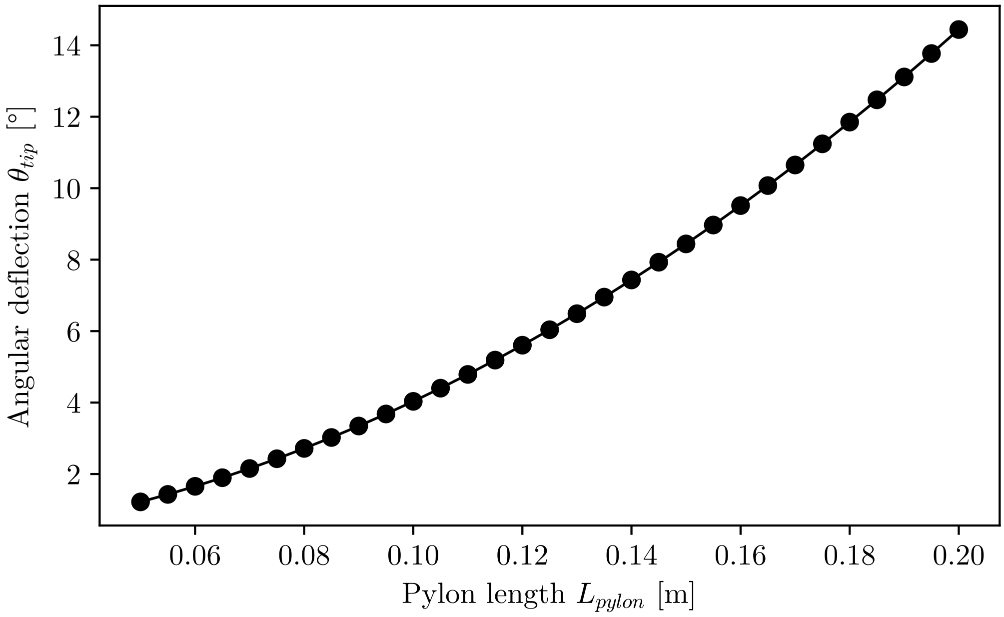

Figure 4.11: Evolution of the static rotation at the pylon tip θ_t as a function of the pylon length L_{pylon} for the flexible pylon configuration, using a PVC pylon with external and internal diameters of 10 mm and 8 mm, respectively.

This trend was also expected, based on the developments of Section 3.8, since the tip rotation angle θ_{tip} contains two contributions. The first one is proportional to L^2, while the second is proportional to L.

Based on Figures 4.10 and 4.11, an acceptable pylon length range can be defined between 0.05 m to 0.14 m. Within this range, the static tip deflection and rotation angle do not exceed 10.5 mm and 7.3°, respectively. The critical speed V_{crit}, defined as the free-stream velocity above which whirl flutter occurs, can therefore be computed over this length range in order to identify the most suitable pylon length.

Figure 4.12 shows the evolution of the critical speed as a function of the pylon length. The selected pylon length range, [0.11, 0.14] m, is highlighted in orange.

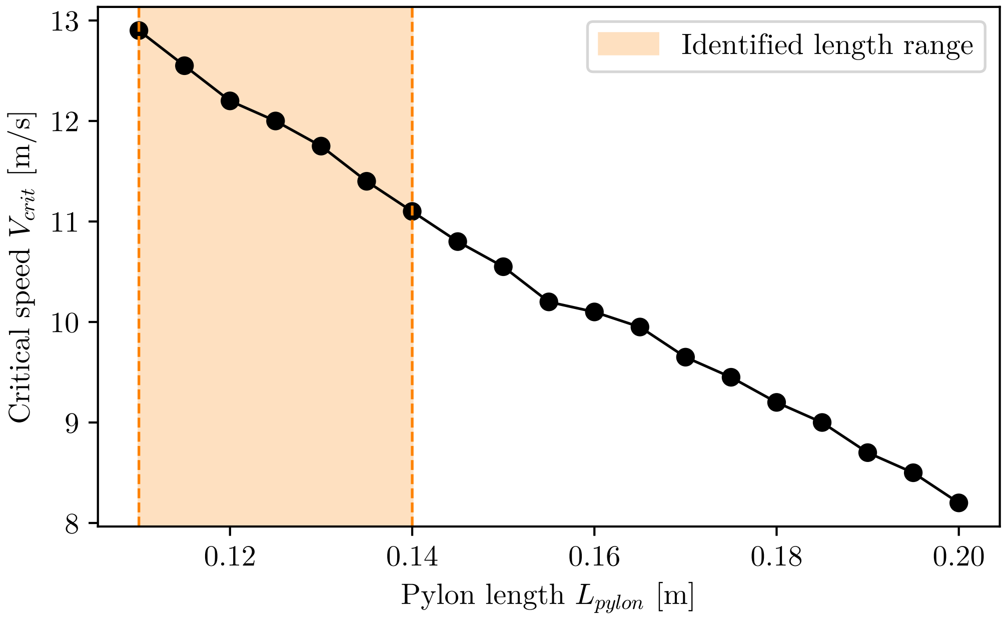

Figure 4.12: Evolution of the whirl flutter critical speed V_{crit} as a function of the flexible pylon length L_{pylon} for a propeller rotational speed Ω equal to 2000 rpm.

As a further comment, length values below 0.11 m are excluded from the analysis, since the system is stable with respect to whirl flutter for these configurations. This can be observed in Figure 4.13, where the real part of the backward whirling mode is represented as a function of the free-stream velocity V for $L_{pylon} = 0.06$ m. The real part of the mode remains negative over the entire free-stream velocity range, meaning that the mode remains stable. This case is representative of all configurations with a pylon length L_{pylon} below 0.11 m.

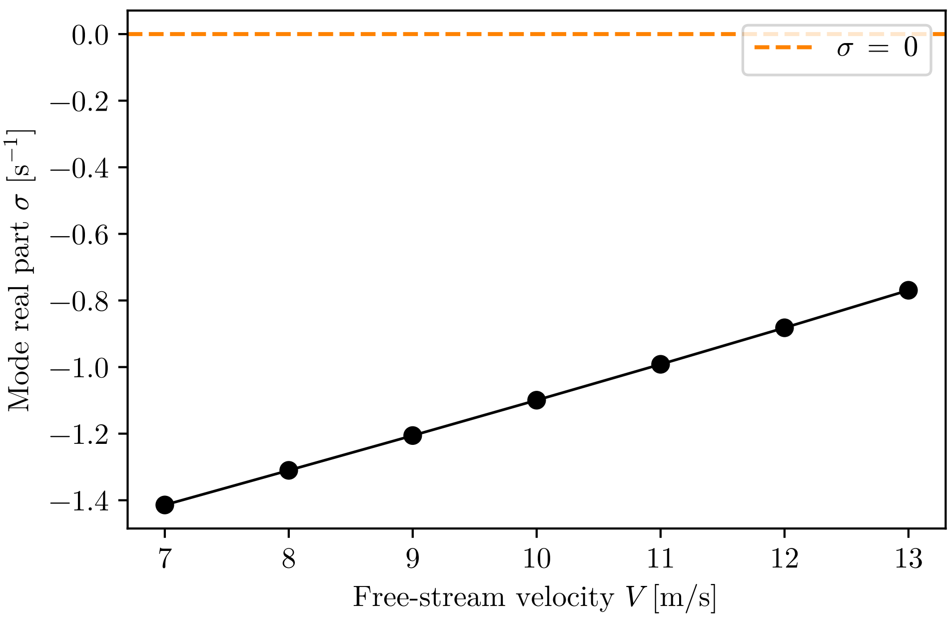

Figure 4.13: Variation of the real part σ of the backward whirl flutter mode as a function of the free-stream velocity V for $L_{pylon} = 0.06$ m and $\Omega = 2000$ rpm.

Based on Figures 4.10, 4.11 and 4.12, an acceptable pylon length is selected as 0.135 m. Table 4.6 summarizes the resulting characteristics of the flexible pylon.

Parameter	
Material	Polyvinyl chloride (PVC)
External diameter	10 mm
Internal diameter	8 mm
Thickness	1 mm
Length	0.135 m
Mass	5.53 g
Polar mass moment of inertia J_1^p	0.1135 kg.mm^2
Transverse mass moment of inertia J_2^p	33.68 kg.mm^2
Bending inertia I_{pylon}	289.81 mm^4
Pitch and yaw equivalent rotational stiffness K_θ and K_ψ	6.01 N.m/rad
Static tip deflection δ_{tip}	10.329 mm
Static tip rotation angle θ_{tip}	6.846 °
$C_\theta \ = \ C_\psi$	0.01 N.s/m^2

Table 4.6: Main characteristics of the pylon used for the flexible pylon configuration.

The inertia ratio defined in Equation 4.5 is equal to 26.13 for the selected configuration. This value indicates that the pylon transverse inertia remains sufficiently low compared with the propeller polar inertia, which is favourable for the occurrence of whirl flutter.

Furthermore, it is useful to compute the oscillation frequency of the independent pitch and yaw modes, i.e. when the rotational speed Ω is set to 0 rpm, in order to assess the influence of the gyroscopic coupling. Since the pylon is symmetric, both frequencies are equal. They can be estimated from the approximation of the first natural frequency of a cantilever beam of mass m_b with a tip mass m. In the present case, the tip mass corresponds to the combined mass of the propeller and the motor. According to Reyes et al., this frequency is given by [76]:

$$f \ \approx \ \frac{1}{2\pi}\sqrt{\frac{3 \ E_{pylon} \ I_{pylon}}{L^3 \ (m \ + \ 0.2409 \ m_b)}}. \tag{4.9}$$

This leads to:

$$f_{pitch} \ = \ f_{yaw} \ = \ 5.22 \text{ Hz}. \tag{4.10}$$

4.3.4 Whirl flutter analysis

Once the pylon geometry is fully defined, the characteristics of both whirling modes can be analysed in detail in order to determine if they can lead to whirl flutter. The theoretical principles of the analysis are introduced in Section 3.5.

First, the forward mode remains stable over the considered velocity range, as shown in Figure 4.14a. In this case, the increase in free-stream velocity tends to stabilize the mode. Therefore, it is not identified as a whirl flutter mode, but only as a forward whirling mode.

Nevertheless, studying it remains useful, since it helps to understand why this mode remains stable and confirms the existence of the forward whirling branch. Additionally, it enables a comparison with the backward whirling mode, for instance in terms of oscillation frequency.

The frequency evolution of this forward mode is represented in Figure 4.14b. It ranges from 3.51 Hz to 3.74 Hz within the relevant free-stream velocity interval, which is lower than the initial independent pitch and yaw modes frequencies identified in 4.10.

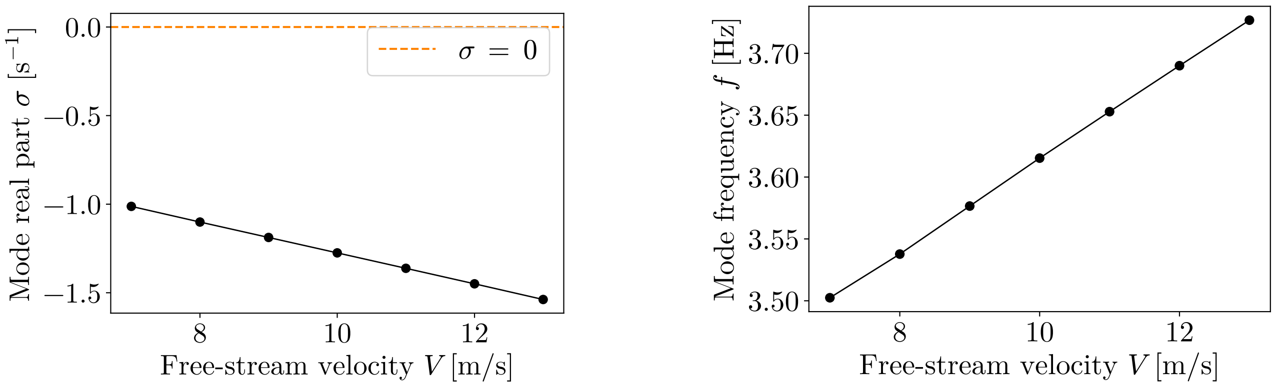

(a) Real part σ.

(b) Frequency f.

Figure 4.14: Evolutions of the frequency f and real part σ of the forward mode as functions of the free-stream velocity V for the final flexible pylon geometry.

The stabilizing effect of the free-stream velocity, through the aerodynamic forces, can also be partially understood by computing the aerodynamic work over one period and the corresponding mean aerodynamic power, both projected onto the considered mode. The two quantities are introduced in Section 3.5.1. Their evolution with the free-stream velocity is shown in Figures 4.15a and 4.15b, respectively.

On the one hand, the work is negative over the whole velocity range, meaning that the aerodynamic forces stabilize the mode. On the other hand, the work decreases as the free-stream velocity increases, indicating that the stabilizing influence becomes stronger.

Since the aerodynamic work remains negative over the whole velocity range, energy is extracted from the structural motion during each oscillation period. As the free-stream velocity increases, this extracted energy becomes larger, which explains the progressive stabilization of the mode observed in Figure 4.14a.

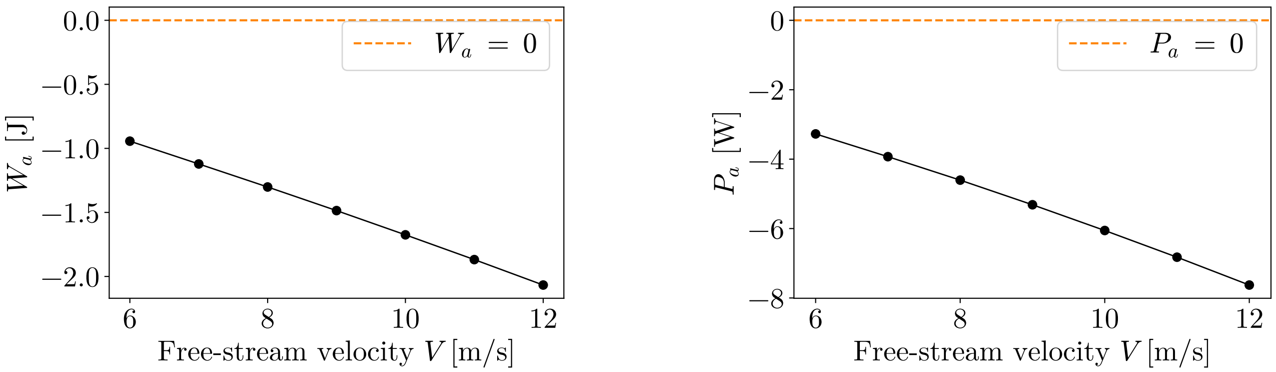

(a) Aerodynamic work over one period W_a.

(b) Aerodynamic power over one period P_a.

Figure 4.15: Evolutions of the work W_a and power P_a over one period exerted by the aerodynamic forces on the forward mode as functions of the free-stream velocity V for the final flexible pylon geometry.

Additionally, the whirling nature of the mode can be verified through the amplitude ratio and the phase difference between the yaw and pitch motions of the pylon, as explained in Section 3.5. The evolution of both quantities is studied over the entire free-stream velocity range to verify that the mode preserves its whirling characteristics. Their variation as functions of the free-stream velocity are shown in Figures 4.16a and 4.16b, respectively.

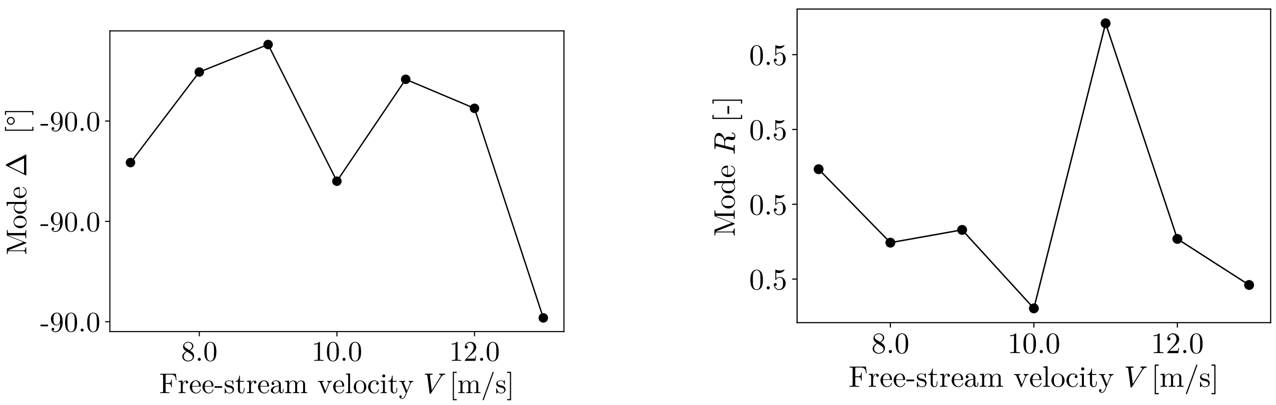

(a) Phase difference $\Delta = \arg\psi - \arg\theta$.

(b) Amplitude ratio $R = \frac{x_{tip}}{z_{tip}}$.

Figure 4.16: Evolutions of the phase difference Δ and the amplitude ratio R of the forward mode as functions of the free-stream velocity V for the final flexible pylon geometry.

The phase difference and amplitude ratio of the forward mode remain equal to -90° and 0.5, respectively, over the entire free-stream velocity range. This confirms that the mode preserves its whirling nature. Furthermore, the sign of the phase difference can be interpreted by analysing the motion of the pylon tip. The oscillatory part of this motion is shown in Figure 4.17a, while the time evolution of the pylon tip motion from $t = 0$ to $t = 20\ T$, with T the period of the mode, is represented in Figure 4.17b. These results are presented for a free-stream velocity equal to 13 m/s.

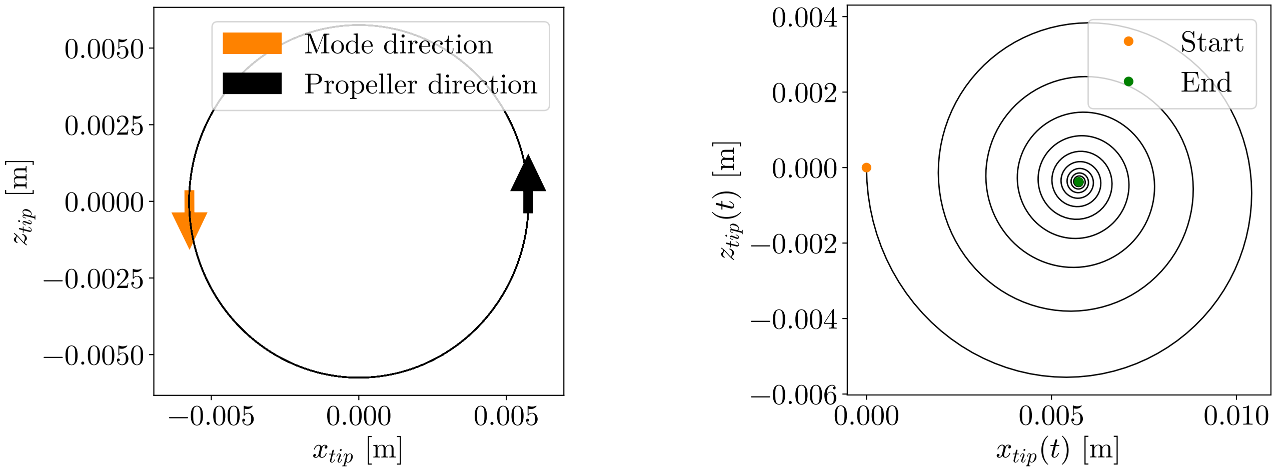

(a) Oscillatory trajectory, with the orange arrow indicating the direction of the oscillations.

(b) Tip displacements time evolution between $t\ = 0$ and $t\ =\ 20\ T$.

Figure 4.17: Oscillatory trajectory and time evolution between $t\ = 0$ and $t\ =\ 20\ T$ of the pylon tip displacements of the forward mode for the final flexible pylon geometry.

This confirms the direction of the oscillatory motion of the mode. The pylon precesses in the same direction as the propeller rotation, which corresponds to the forward whirling mode. Additionally, Figure 4.17b illustrates the stable behaviour of the mode, since the pylon tip starts from its initial position and progressively converges towards a well-defined point. The spiral does not diverge. Therefore, this mode cannot be considered as a flutter mode, since it remains stable over the considered velocity range.

Second, the backward whirling mode, responsible for the instability, is investigated in the same way as the forward mode. In contrast to the forward mode, the aerodynamic forces destabilize the mode, which becomes unstable above a certain free-stream velocity, called the critical speed V_{crit}. This critical speed can be identified in Figure 4.18, where the real part of the backward whirl flutter mode is represented as a function of the free-stream velocity.

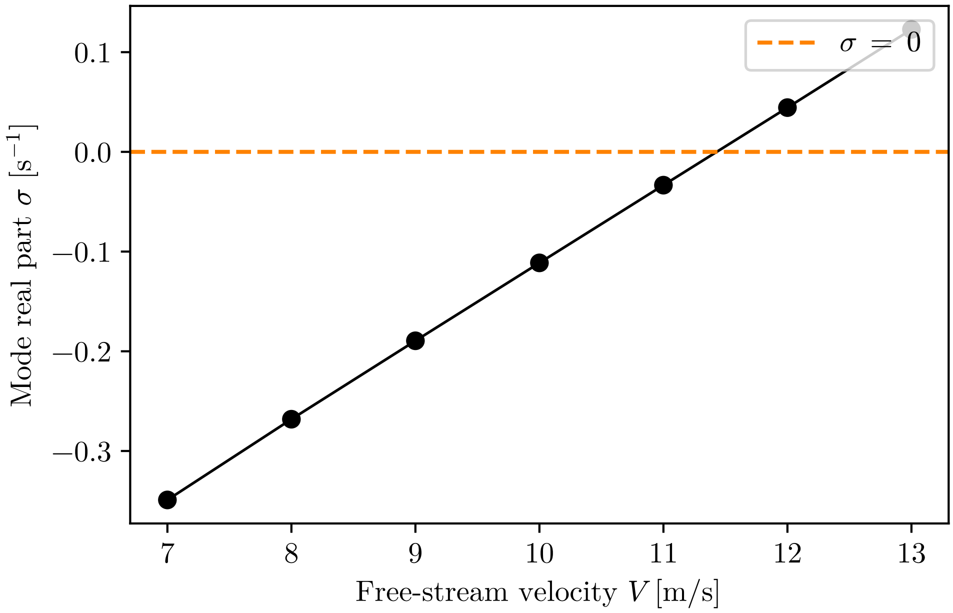

Figure 4.18: Evolution of the real part σ of the backward mode as a function of the free-stream velocity V for the final flexible pylon geometry.

Based on this evolution, the critical whirl flutter velocity is identified as 11.4 m/s. This behaviour differs from that of the forward mode, since the real part becomes positive above this critical value. It can also be understood through the aerodynamic work over one period and the corresponding mean aerodynamic power, both projected onto the considered mode. Both evolutions as functions of the free-stream velocity are represented in Figure 4.19.

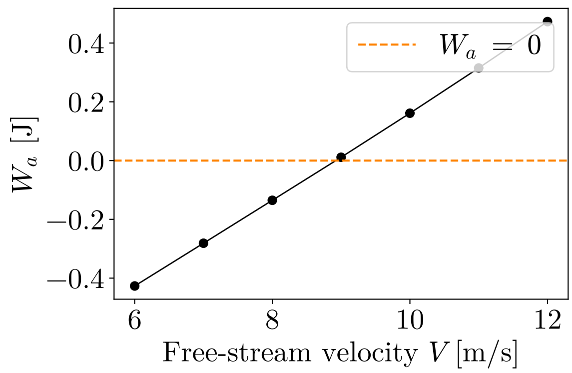

(a) Aerodynamic work over one period W_a.

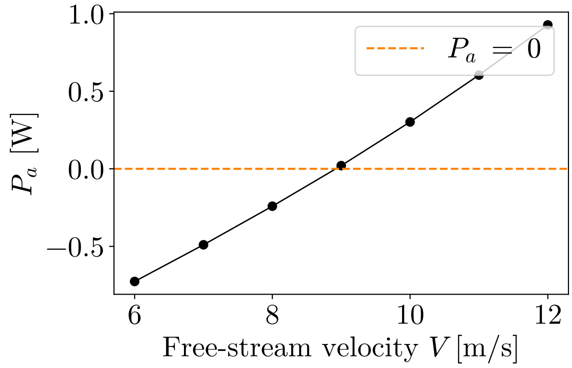

(b) Aerodynamic power over one period W_a.

Figure 4.19: Evolutions of the work W_a and power P_a over one period exerted by the aerodynamic forces on the backward mode as functions of the free-stream velocity V for the final flexible pylon geometry.

In contrast to the forward whirling mode, the aerodynamic work becomes positive for the backward mode. This means that the aerodynamic forces transfer energy to the structural motion during each oscillation period. Since both the aerodynamic work and the mean aerodynamic power increase with the free-stream velocity, the destabilizing effect of the aerodynamic forces becomes progressively stronger, confirming the evolution observed in Figure 4.18, where the real part of the backward mode increases with V. Below the critical velocity, the mode remains stable because the aerodynamic energy input remains too limited to produce a divergent modal response. However, as the free-stream velocity increases, this energy input becomes large enough to change the stability of the backward mode, leading to the onset of whirl flutter instability at $V_{crit} = 11.4$ m/s.

The frequency evolution over the free-stream velocity range follows the same trend as for the forward mode. As shown in Figure 4.20, the frequency f increases with the free-stream velocity V.

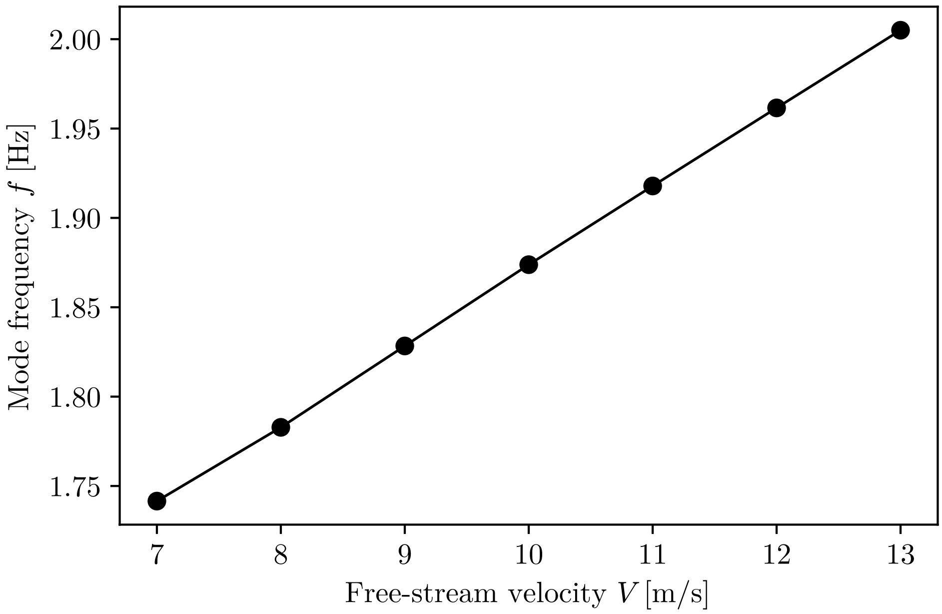

Figure 4.20: Evolution of the frequency f of the backward whirl flutter mode as a function of the free-stream velocity V for the final flexible pylon geometry.

Additionally, it confirms the statement of Section 2.1, according to which the frequency of the forward whirling mode is higher than the frequency of the backward mode. This is observed throughout the entire free-stream velocity range. Indeed, the frequency of the backward whirl flutter mode ranges from 1.74 Hz to 2.1 Hz, whereas the frequency of the forward mode ranges from 3.51 Hz to 3.74 Hz. Moreover, the frequency of the backward whirl flutter mode remains lower than the approximation of the independent pitch and yaw modes frequencies, meaning that both coupled whirling modes have lower frequencies than the independent pitch and yaw modes.

Finally, similarly to the forward mode, the whirling nature of the backward mode is analysed over the free-stream velocity range by considering its phase difference and amplitude ratio. The corresponding results are shown in Figure 4.21.

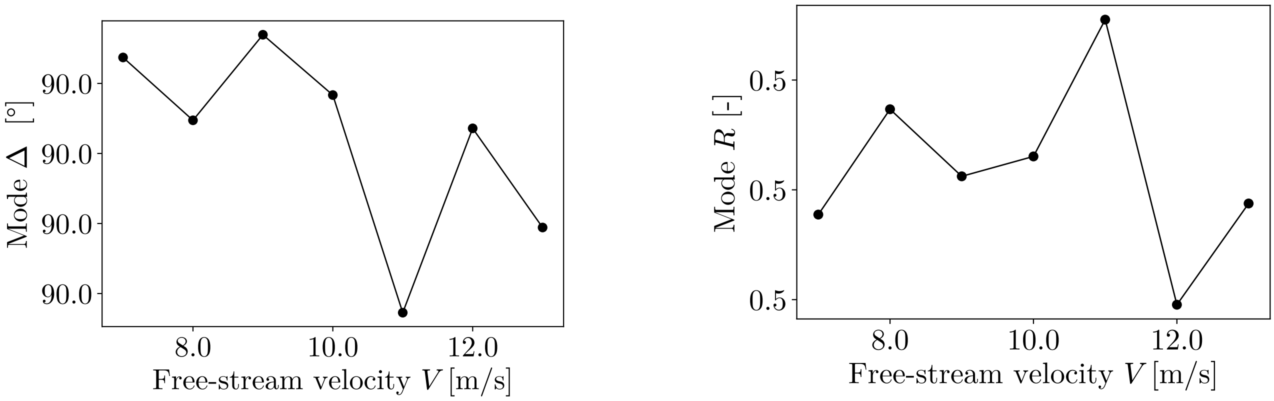

(a) Phase difference $\Delta = \arg\psi - \arg\theta$.

(b) Amplitude ratio $R = \frac{x_{tip}}{z_{tip}}$.

Figure 4.21: Evolutions of the phase difference Δ and the amplitude ratio R of the backward mode as functions of the free-stream velocity V for the final flexible pylon geometry.

The phase difference $\Delta_{backward}$ is opposed to $\Delta_{forward}$ and is equal to 90°, meaning that both modes whirl in opposite directions. Combined with an amplitude ratio equal to 0.5, this indicates that the mode theoretically describes a circular motion, as expected from the symmetry of the pylon geometry. This is verified in Figure 4.22, which shows the oscillatory motion of the pylon, and the time evolution of the pylon tip displacement between $t = 0$ and $t = 20\ T$, starting from an initial position. These results are again computed for a free-stream velocity equal to 13 m/s.

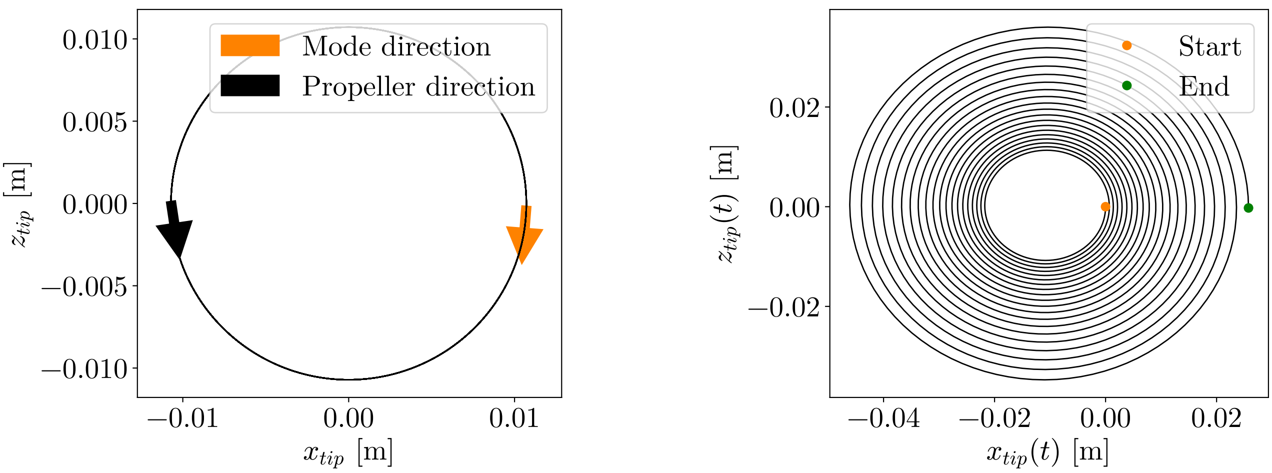

(a) Oscillatory trajectory, with the orange arrow indicating the direction of the oscillations.

(b) Tip displacements time evolution between $t = 0$ and $t = 20\ T$.

Figure 4.22: Oscillatory trajectory and time evolution between $t = 0$ and $t = 20\ T$ of the pylon tip displacements of the backward mode for the final flexible pylon geometry.

On the one hand, Figure 4.22b shows the unstable behaviour of the backward mode. It deviates from the initial position and diverges, i.e. the spiral described by the pylon tip does not converge to a single point. On the other hand, Figure 4.22a confirms the precession direction of the backward whirl flutter mode. The pylon is whirling in the opposite direction than the rotational direction of the propeller.

Finally, it is useful to analyse the blade deformations associated with this backward whirl flutter mode. The procedure used to obtain these deformations is developed in Section 3.7. The blade deformations in the three planes of frame R_2 are shown in Figure 4.23, for an arbitrary time instant $t = 10$ s and a free-stream velocity V equal to 13 m/s.

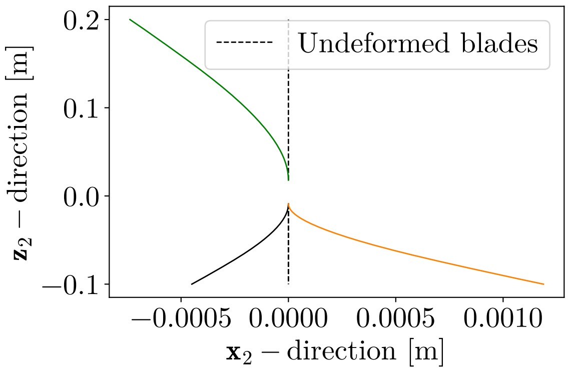

(a) Plane $\mathbf{x_2 z_2}$, enables visualization of the out-of-plane motion and the traction.

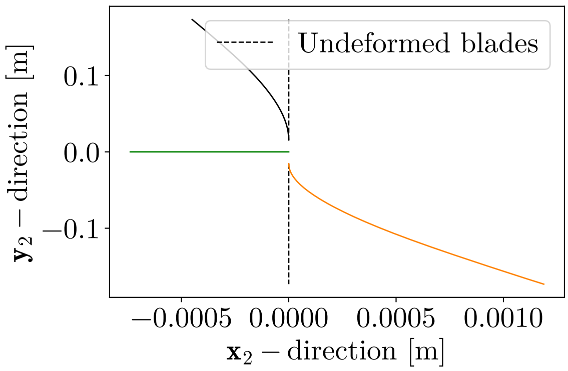

(b) Plane $\mathbf{x}_2\mathbf{y}_2$, enables visualization of the out-of-plane motion and the traction.

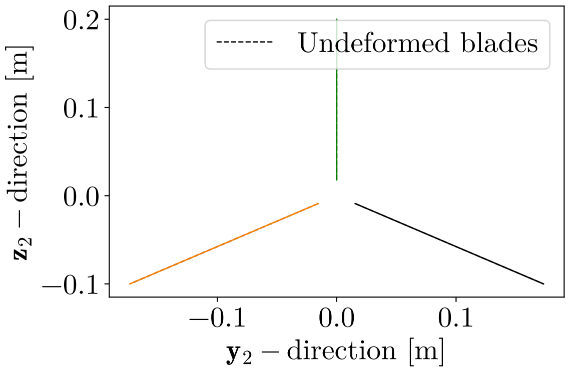

(c) Plane $\mathbf{y}_2\mathbf{z}_2$, enables visualization of the in-plane blade motion.

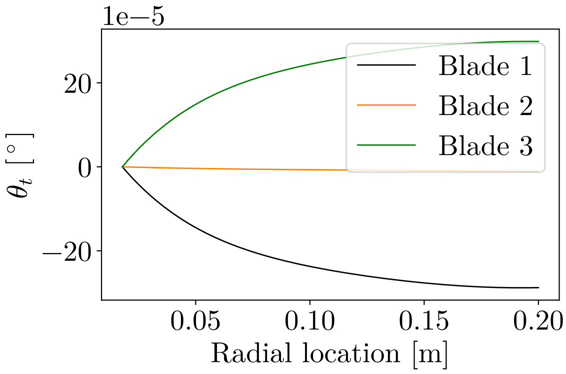

(d) Radial distribution of the torsion angle.

Figure 4.23: Blade deformation in the $\mathbf{x_2 z_2}$, $\mathbf{y}_2\mathbf{z}_2$ and $\mathbf{x}_2\mathbf{y}_2$ planes, as well as the radial distributions of the torsion of the blades for the backward whirl flutter mode.

It can be observed that the blade deformations do not contribute with the same amplitude. In particular, the out-of-plane deformation is significantly larger than the in-plane deformation. Its radial distribution shows a deformation that increases with the radial position. This behaviour is analogous to the deformation shape associated with the first bending mode of a cantilever beam, for which the displacement is generally larger near the free end. This out-of-plane motion modifies the orientation of the blade sections with respect to the incoming flow, which can affect the local aerodynamic forces. Concerning torsion, the blade sections located at larger radii experience a larger variation in local twist angle, since the torsion angle directly contributes to this quantity. However, for one of the blades, the torsion angle remains negligible compared with the two others.

It is important to note that the amplitudes shown in the modal deformation Figures should not be interpreted as absolute physical deformation values. As for the other modal visualizations, the amplitudes depend on the chosen mode-shape normalization. In this case, the mode has been normalized by its maximum amplitude, so that the figure is used only to visualize the relative deformation components. A direct comparison with the hub motion would be required to assess the actual contribution of the blade deformations to the complete system motion.

Furthermore, the column and row indices defined in 3.150 are shown in Figure E.1 of Appendix E as functions of the free-stream velocity for the tracking procedure of the backward whirl flutter mode.

4.4 Rigid pylon model

In this configuration, the pylon is assumed to be rigid and is therefore no longer responsible for the system flexibility. Instead, linear springs are attached to pylon at a distance d from the pivot point. In this case, the pylon is not rigidly clamped at the pivot point. Instead, it is connected to a flexible mount located at the pivot point, in order to allow pitch and yaw motions.
Two linear traction springs are used for the pitch motion, with a stiffness coefficient k_z, and two additional linear traction springs are used for the yaw motion, with stiffness coefficient k_x. This configuration is shown in Figure 4.24.

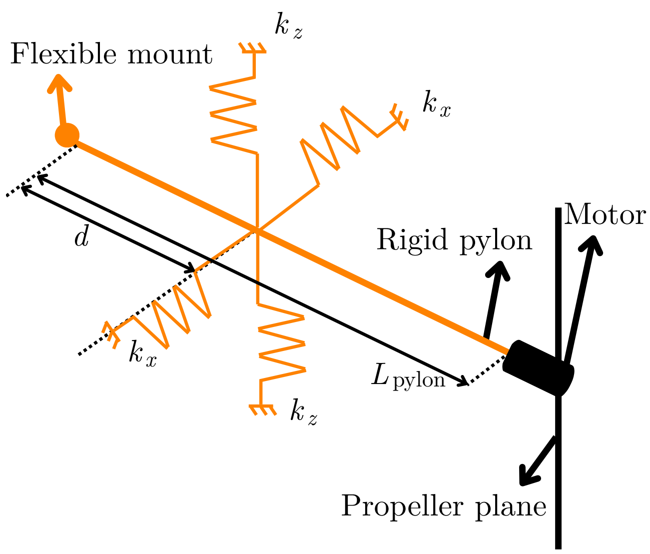

Figure 4.24: Rigid pylon analytical model.

Additionally, traction springs are selected because they can be easily attached to the rigid pylon, as they are equipped with hooks.

However, using tractions springs require an initial elongation. Without any pre-elongation, when one pitch spring is further elongated during the motion, the opposite spring would tend to be compressed. This is not physically possible for a traction spring. The same reasoning applies to the pair of traction springs used for the yaw motion.

Therefore, initial elongations must be applied to the four springs in order to allow the pitch and yaw oscillatory motions associated with whirl flutter.

If the lower pitch spring is initially pre-elongated, it remains in tension even when the upper pitch spring is further elongated during the motion. Therefore, the initial elongation must be large enough to keep all springs under tension throughout the oscillatory motion. This condition ensures that each spring remains active during the whole motion, so that the effective stiffness of the system is not modified by a temporary loss of tension. At the same time, the maximum total elongation achieved during the motion must remain within the linear operating range of the springs, i.e. below the maximum admissible elongation.

For the yaw springs, an initial elongation $x_0^{yaw} = 10$ mm is selected as a general design value. This value obviously depends on the expected oscillation amplitude. However, the situation is different for the pitch springs, because the weights of the pylon, motor, and propeller also contribute to the static elongation of the vertical springs. This static elongation modifies the equilibrium position of the system and therefore the static orientation of the propeller plane. Hence, the initial elongation of the pitch springs is taken as the sum of a motion-related contribution, $x_{0,motion}^{pitch} = 10$ mm, previously defined for the yaw springs, and a static-weight contribution, denoted by $x_{0,weight}^{pitch}$. This contribution is discussed later.

The linear springs are introduced into the analytical model through equivalent rotational stiffnesses. Therefore, the linear spring stiffnesses have to be determined from the required rotational stiffnesses K_θ and K_ψ. To do so, a relationship between linear k and rotational K stiffnesses must be established.

In the analytical model introduced in Section 3.1, the pitch and yaw stiffnesses K_θ and K_ψ are defined as rotational stiffnesses located at the pivot point. In the present configuration, these rotational stiffnesses are provided by linear springs attached to the pylon at a distance d from the pivot point. According to Hooke's law, the force F generated by a linear spring is given by [77]:

$$F = k\,x, \tag{4.11}$$

where k denotes the linear spring stiffness and x denotes the spring elongation.

If the linear springs are placed at a distance d from the rotational spring, the small displacements and angles assumptions lead to $x = d\,\theta_s$, with θ_s the rotation of the equivalent rotational spring. Hence, the restoring moment M generated by the two linear spring forces is given by:

$$M = 2\;F\;d = 2\;k\;x\;d = 2\;k\;(d\theta_s)\;d = 2\;k\;\theta_s\;d^2. \tag{4.12}$$

Additionally, the stiffness coefficient K of a rotational spring is defined as [78]:

$$K = \frac{M}{\theta_s}. \tag{4.13}$$

Combining this definition with Equation 4.12, it comes:

$$K = 2\;k\;d^2 \qquad \Rightarrow \qquad k = \frac{K}{2\;d^2}. \tag{4.14}$$

Therefore, the closer the linear springs are placed to the pivot point, the higher the required linear spring stiffness coefficient. In contrast, placing the springs farther from the pivot point reduces the required linear stiffness.

For instance, if the springs are placed at the pylon tip, the equivalent rotational stiffness would be four times higher than if they were placed at the middle of the pylon. Nevertheless, motor, propeller and other components described in Chapter 5 are already located at the pylon tip. In order not to disturb this assembly, the springs are chosen to be placed at the middle of the pylon, such that $d = \frac{L_{pylon}}{2}$. This leads to:

$$k_x = k_z = \frac{K_\theta}{2\;d^2} = \frac{K_\psi}{2\;d^2}, \tag{4.15}$$

since symmetry between pitch and yaw stiffnesses is still preferred. The factor 2 comes from the fact that two identical linear springs are used for each motion. Therefore, the required equivalent rotational stiffness is provided by two equal spring contributions.

Since the pylon is assumed to be rigid, its static tip deflection and rotation angle are negligible. Nevertheless, another static effect must be taken into account. As stated previously, the vertical linear springs can experience a static elongation due to the weight of the motor, propeller and pylon. If this elongation is significant, it can induce an initial rotation of the propeller plane, therefore modifying the equilibrium position and the dynamics of the system.

As mentioned previously, this issue can be solved by applying an additional initial elongation to the vertical springs, denoted by $x_{0,weight}^{pitch}$, in addition to the motion-related initial elongation, denoted by $x_{0,motion}^{pitch}$. If the static elongation of the vertical springs due to the system weight is denoted by x_{stat}, the following condition must be satisfied:

$$x_0^{pitch,up} \; - \; x_0^{pitch,down} \; = \; x_{stat}, \tag{4.16}$$

so that the static orientation of the propeller plane vanishes. The quantities $x_0^{pitch,up}$ and $x_0^{pitch,down}$ denote the total static elongations of the upper and lower pitch springs, respectively.
By satisfying this condition, the static effect of the system weight is compensated by the difference between the initial elongation of the upper and lower pitch springs. At the same time, both vertical springs remain pre-elongated, which allows them to contribute to the whirl flutter motion.

The required weight-related static elongation can now be computed.
Starting from the rotational spring stiffness defined in 4.13, and considering that the moment around the pivot point due to the system weight is given by $M_{stat} \; = \; m_{system} \; g \; l$, where l is the distance between the pivot point and the system centre of mass, the static rotation angle is obtained as:

$$\theta_{stat} \; = \; \frac{M_{stat}}{K} \; = \; \frac{m_{system} \; g \; l}{K}. \tag{4.17}$$

Due to the relatively low mass of the pylon compared to the motor-propeller assembly, the system centre of mass is assumed, as a first approximation, to be located at the pylon tip. Hence, $l \; = \; L_{pylon}$. Using the small-displacement and small-rotation assumptions, the relationship between K and k, given in 4.14, and considering that the linear springs are placed at the middle of the pylon, the following expressions are obtained:

$$x_{stat} \; = \; d \; \theta_{stat} \; = \; d \; \frac{m_{system} \; g \; L_{pylon}}{2 \; k \; d^2} \; = \; \frac{m_{system} \; g}{k} \qquad \text{and} \qquad \theta_{stat} \; = \; \frac{2 \; m_{system} \; g}{L_{pylon} \; k}. \tag{4.18}$$

These expressions show that the system mass directly influences the static elongation of the pitch springs, even if the pylon mass is assumed to remain small compared with the motor-propeller assembly. Additionally, no static force or moment is applied to the yaw springs, leading to zero static elongation for these springs.

Therefore, once the spring location has been fixed for mechanical reasons, the stability study is performed by varying the intrinsic stiffness of the linear springs. In the following analysis, pitch and yaw stiffness symmetry is imposed, so that $k \; = \; k_x \; = \; k_z$.

4.4.1 Pylon material selection

For this configuration, material selection criteria differ from those of the flexible pylon configuration, since the pylon is assumed to be rigid. Therefore, a high Young's modulus is required, while a moderate density remains preferable in order to limit the static elongation of the pitch linear springs.

Based on Figure 4.9, the metal material family appears to be a suitable choice. Specifically, one aluminium alloy is selected as the pylon material for this configuration. The 6082 aluminium alloy is selected because it is commonly used and can be easily manufactured. Table 4.7 lists the main properties of this material.

Parameter	Value
Young's modulus E_{pylon}	70 GPa
Density ρ_{pylon}	2700 kg/m^3

Table 4.7: Young's modulus and density of the 6082 aluminium alloy [79].

Moreover, the choice of this material is consistent with the discussion concerning the inertia ratio introduced in Equation 4.5. Selecting steel as the pylon material would lead to a significantly higher pylon mass and transverse inertia J_p^2. This would reduce the inertia ratio and would therefore be less favourable for the occurrence of whirl flutter. It would also increase the static elongation of the pitch springs.

4.4.2 Pylon shape and geometry

The goal of this configuration is to keep the same pylon shape and dimensions as in the flexible pylon configuration, in order to allow a direct comparison between both cases. Only the material is changed in order to increase the rigidity of the pylon, as discussed in Section 4.4.1. Therefore, the pylon is selected as a hollow circular tube, which preserves the symmetry between pitch and yaw stiffnesses.

The polar and transverse mass moments of inertia, denoted by J_1^p and J_2^p, respectively, have been previously defined in Equations 4.7 and 4.8.

Additionally, based on the selected material and geometry, the static tip deflection and rotation angle of the pylon can be computed. Both quantities are provided in Table 4.8.

Parameter	Value
Tip deflection δ_{tip}	0.274°
Tip rotation angle θ_{tip}	0.413 mm

Table 4.8: Static tip deflection and rotation angle for the rigid pylon configuration.

These values are negligible, confirming that the pylon remains sufficiently rigid under the weight of the motor-propeller assembly.

Besides, once the material and geometry are defined, the main pylon characteristics can be computed. These quantities are summarized in Table 4.9.

Parameter	
Material	6082 aluminium alloy
External diameter	10 mm
Internal diameter	8 mm
Thickness	1 mm
Length	0.135 m
Mass	10.31 g
Polar mass moment of inertia J_1^p	0.2113 kg.mm^2
Transverse mass moment of inertia J_2^p	62.71 kg.mm^2
Bending inertia I_{pylon}	289.81 mm^4
$C_\theta = C_\psi$	0.015 N.s/m^2

Table 4.9: Main characteristics of the pylon for the rigid pylon configuration.

For the selected configuration, the inertia ratio is therefore equal to 14.03. Although lower than for the flexible pylon configuration, this value still indicates a favourable inertial balance between the rotating propeller and the rigid pylon.

4.4.3 Linear spring stiffnesses

First, the static weight-related elongation of the vertical springs has to be determined. Figure 4.25 shows the initial elongation required for the upper vertical spring under the system weight as a function of stiffness k_z. Therefore, it represents the required static pre-elongation $x_{0,weight}^{pitch}$ to compensate for the weight-induced rotation and to keep the free-stream velocity aligned with the propeller axis. Stiffness values above 3.3 N/m are not considered, since it will be shown that they lead to a stable system, and are therefore not relevant for the present application.

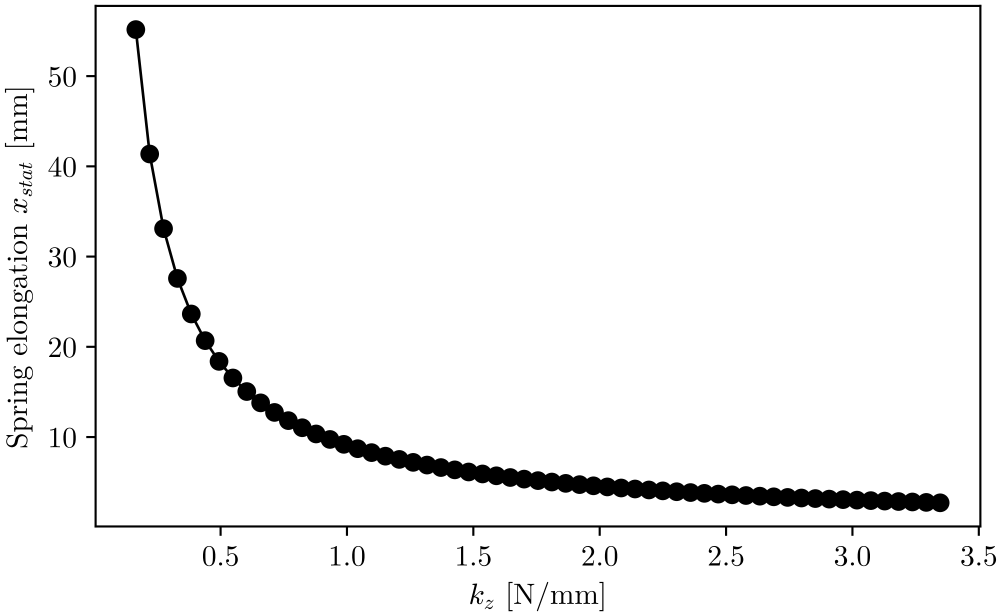

Figure 4.25: Static elongation of the vertical spring as a function of its stiffness coefficient k_z, for the rigid pylon configuration.

Additionally, as the vertical springs are located at $\frac{L_{pylon}}{2}$, the static elongation can be related to the static rotation angle as:

$$x_{stat} = \frac{L_{pylon}}{2} \theta_{stat}. \tag{4.19}$$

This angle correspond to the rigid rotation of the pylon induced by the static elongation of the vertical springs. Figure 4.26 shows the evolution of θ_{stat} as a function of the vertical spring stiffness.

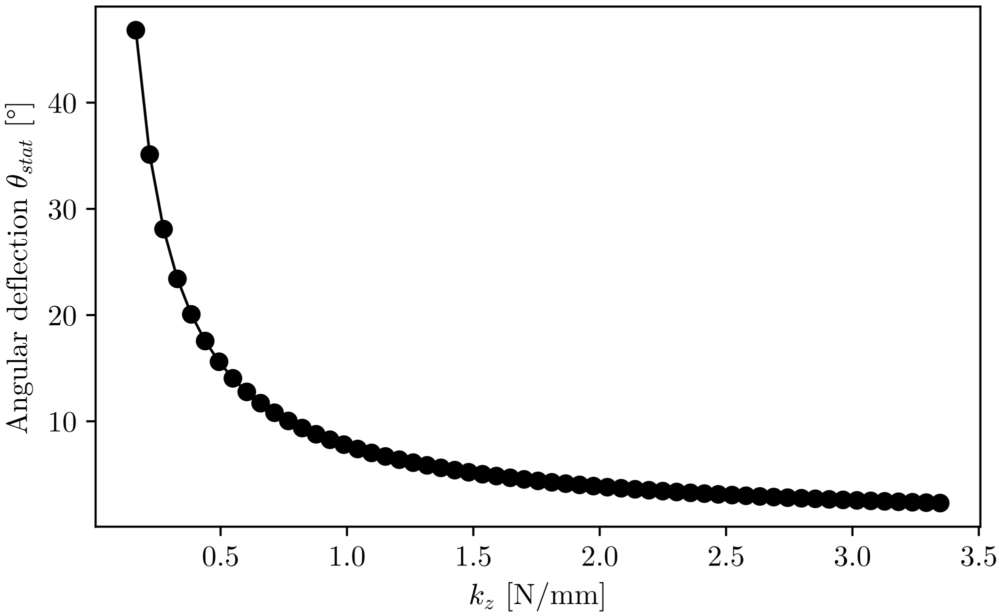

Figure 4.26: Static pylon tip rotation angle θ_{stat} as a function of the vertical spring stiffness k_z for the rigid pylon configuration.

This highlights the importance of applying an additional initial elongation to the upper vertical spring, since θ_{stat}, which represents the static orientation angle of the propeller plane, can remain significant even for relatively high stiffness values.

Therefore, by applying an initial elongation to the vertical springs, a wide range of pitch stiffness values can be investigated, as long as the springs remain within their linear operating range. This makes it possible to study the influence of the pitch stiffness on the stability behaviour of the system.

The stability of the backward whirl flutter mode with respect to the pitch and yaw linear stiffnesses, k_z and k_x, respectively, is now investigated. Figure 4.27 shows the evolution of the real part of the backward mode as a function of the linear stiffnesses, for four different free-stream velocities. Additionally, the stiffness step is adapted within the considered stiffness range in order to improve the efficiency and robustness of the mode tracking procedure, as described in Section 3.6.
The forward whirling mode is not analysed here, since it remains stable over the entire considered stiffness range.

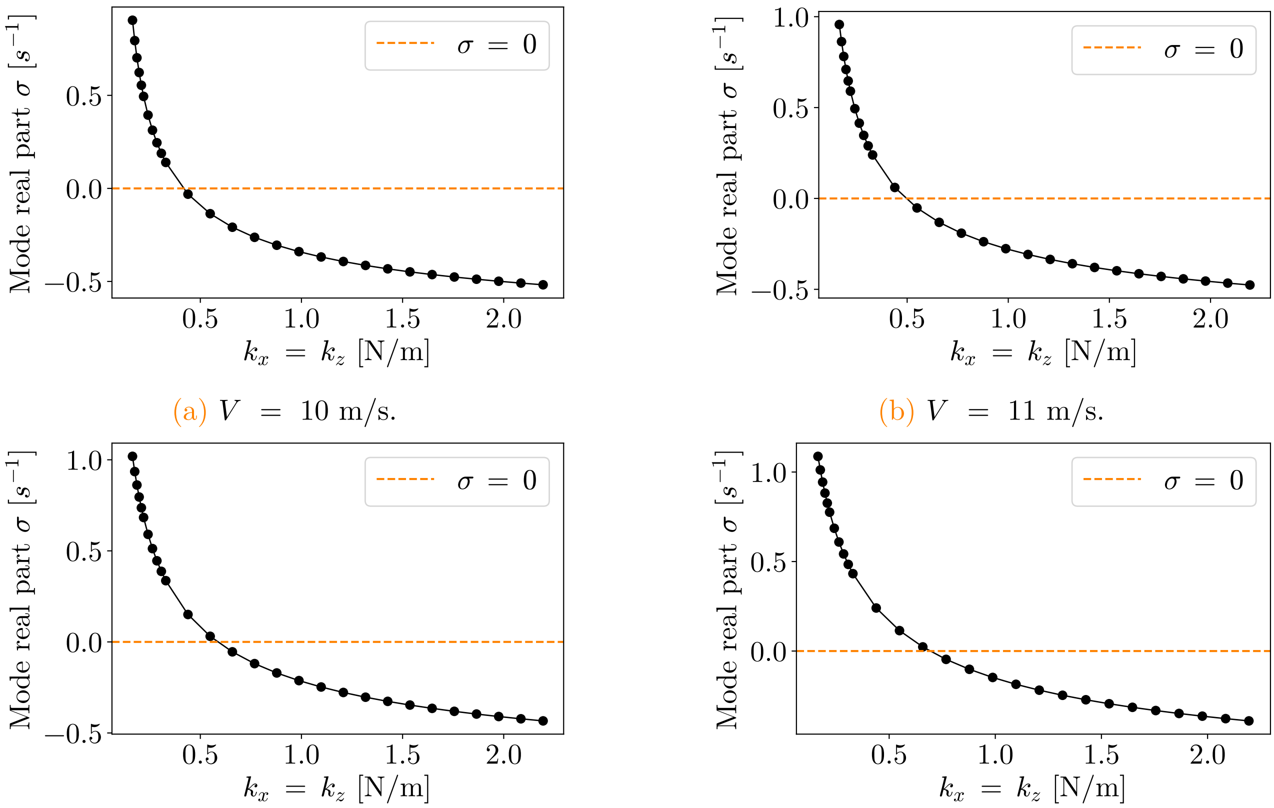

(a) $V = 10$ m/s. (b) $V = 11$ m/s.

(c) $V = 12$ m/s. (d) $V = 13$ m/s.

Figure 4.27: Evolution of the real part σ of the backward whirl flutter mode as a function of the linear stiffnesses k_x and k_z for the rigid pylon configuration at $V = 10$ m/s, $V = 11$ m/s, $V = 12$ m/s and $V = 13$ m/s.

As expected, for a given free-stream velocity V, decreasing the stiffnesses k_x and k_z makes the system less stable. In contrast, when the stiffnesses become too high, the system is no longer sufficiently flexible, and the backward mode remains stable. The same trend is observed for all the considered free-stream velocities, although the stability level depends on the velocity. For instance, for a given stiffness value, increasing the free-stream velocity increases the real part of the mode. This is consistent with the behaviour observed in Figure 4.18 for the flexible pylon configuration.

Additionally, frequency evolution of the mode is shown in Figure 4.28 as a function of the spring stiffness, for the same free-stream velocities as those considered in Figure 4.27.

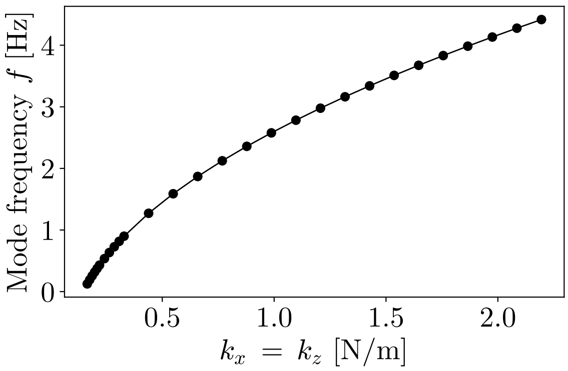

(a) $V = 10$ m/s.

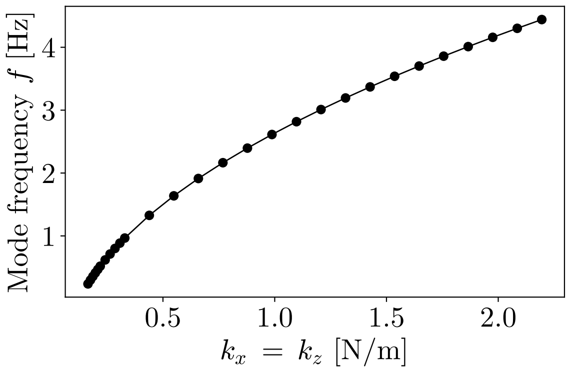

(b) $V = 11$ m/s.

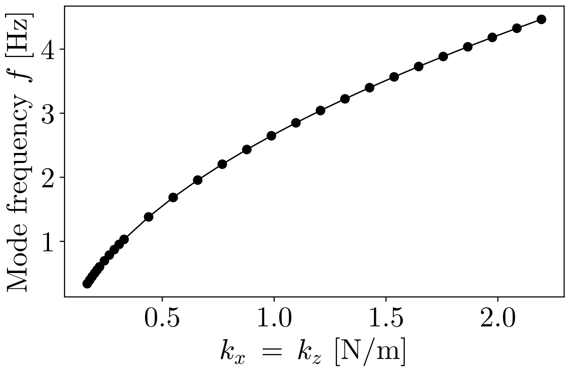

(c) $V = 12$ m/s.

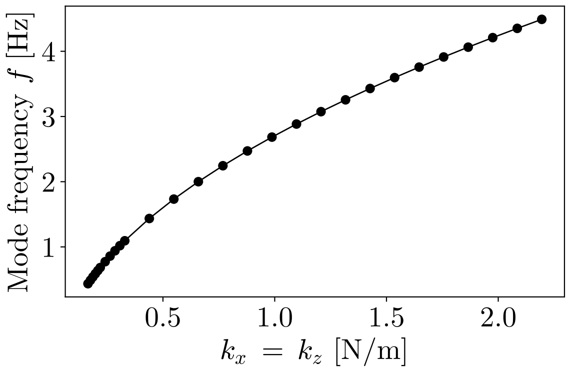

(d) $V = 13$ m/s.

Figure 4.28: Evolution of the frequency f of the backward whirl flutter mode as a function of the linear stiffnesses k_x and k_z for the rigid pylon configuration at $V = 10$ m/s, $V = 11$ m/s, $V = 12$ m/s and $V = 13$ m/s.

On the one hand, the same trend as for the flexible pylon configuration, shown in Figure 4.20, is observed. For a given stiffness value, the mode frequency slightly increases with the free-stream velocity. This variation remains weak, but the trend can still be identified.

On the other hand, for a given free-stream velocity, the mode frequency increases with the spring stiffness, which is the expected behaviour. This observation can be understood by analogy with an undamped one-degree-of-freedom mass–spring oscillator in free vibration. In that case, the oscillation frequency $f_{1\ \text{dof}}$ is given by [80]:

$$f_{1\ \text{dof}} = \frac{1}{2\pi}\sqrt{\frac{k}{m}}, \tag{4.20}$$

where k and m are the stiffness and mass of the system, respectively.

Therefore, if the stiffness of the one-degree-of-freedom oscillator increases, its oscillation frequency also increases. A similar trend is observed for the rigid pylon-propeller system considered here, even though it is a coupled aeroelastic system with several degrees of freedom.

A detailed whirl flutter analysis similar to the one performed for the flexible pylon configuration is not repeated for the rigid pylon configuration, since the results obtained for both configurations are close. The main trends are similar, as well as the physical mechanisms governing the instability.

As a conclusion, based on Figure 4.27, the system can become unstable under well defined conditions, which would not be possible if the flexibility were only provided by the rigid pylon. A comparison between the flexible and rigid pylon configurations can now be performed.

4.5 Comparison of the two configurations

A first comparison between both configurations can be made by analysing the origin and magnitude of the equivalent rotational stiffnesses involved in each case.

For the selected rigid pylon geometry and material, the equivalent rotational stiffness of the pylon can be computed from Equation 4.6, as for the flexible pylon configuration. This leads to equal pitch and yaw equivalent stiffnesses, $K_\theta = K_\psi = 150.27$ N.m/rad, which correspond to the stiffnesses of the rigid pylon alone, without the linear springs.

For the linear springs, the equivalent rotational stiffnesses are computed from Equation 4.15. For $k_x = k_z = 500$ N/m, which leads to an unstable system over the considered free-stream velocity range, as shown in Figure 4.27, the corresponding equivalent rotational stiffnesses K_θ and K_ψ are equal to 18.23 N.m/rad.

This value significantly lower, than the stiffness directly provided by the pylon, by almost one order of magnitude. It highlights the usefulness of this configuration because achieving this stiffness would not lead to whirl flutter for the flexible pylon configuration without springs. Therefore, the springs allow a rigid pylon system to become unstable in whirl flutter.

Considering now the flexible pylon configuration, the instability was obtained for lower equivalent pylon stiffnesses $K_\theta = K_\psi = 6.01$ N.m/rad. For equivalent rotational stiffnesses higher than 10 N.m/rad, the flexible pylon configuration would not allow whirl flutter to be observed with the present geometry.

Therefore, the rigid pylon configuration with linear springs extends the range of equivalent rotational stiffnesses for which whirl flutter can be obtained. This is possible because the equivalent stiffness governing the instability is mainly imposed by the springs, rather than by the pylon deformation. This highlights the main interest of this configuration: the flexibility required to obtain whirl flutter can be introduced by the springs, while keeping the pylon itself much stiffer.

Both configurations have their own advantages and drawbacks. The flexible pylon configuration is more difficult to design, because the pylon rigidity and system flexibility cannot be tuned independently. If the length is increased, the system becomes more flexible, which is favourable for the occurrence of whirl flutter. Nevertheless, this also decreases the static rigidity of the pylon, possibly leading to significant tip deflection and rotation. Therefore, a trade-off has to be found with respect to the dimensions, shape and material of the pylon, which can be restrictive for a real experimental setup.
In contrast, the rigid pylon configuration allows the system flexibility and pylon rigidity to be designed completely independently. Thus, the pylon tip deflection and rotation can be made negligible, while the system can still become unstable thanks to the flexibility introduced by the linear springs. This is one of the advantages of this configuration. However, the initial elongations of the springs have to be computed carefully, and the springs must remain within their linear operating range. In particular, the vertical spring pre-elongation must be properly adjusted to maintain the nominal orientation of the propeller plane.

Additionally, from an experimental point of view, the flexible pylon can be more difficult to assemble with the motor-propeller system. The connection between the motor and the pylon, called the motor support, can be more complicated to design and to integrate into the setup. This design component is discussed in Chapter 5. Nonetheless, one of the advantages of this configuration is that the length of the pylon can be varied easily. Therefore, the system flexibility can be modified by adjusting the pylon length, while still accounting for the resulting tip deflection and rotation. However, changing the pylon length also modifies other quantities, such as the pylon mass, transverse inertia, and static behaviour. As a result, the flexibility cannot be adjusted independently from the other design parameters.
Concerning the rigid pylon model, the flexibility can also be modified by changing the spring attachment position or by selecting different springs. In this case, the system flexibility is mainly controlled by the springs, without requiring a modification of the pylon geometry. This makes the configuration more modular and easier to tune experimentally. Furthermore, the motor support can be fixed more easily than for the flexible pylon configuration, since the pylon is rigid and made of a material that

can be easily modified and assembled. Despite this, this configuration requires additional design considerations concerning the actual choice of the springs, their attachment to the pylon, and the flexible mount located at the pivot point. In contrast, a classical PVC tube rigidly clamped at the pivot point remains simpler from a conceptual and manufacturing point of view.

Chapter 5. Experimental setup

The flexible pylon configuration introduced in Section 4.3 is selected for the experimental setup. This chapter does not present wind tunnel experimental results. Instead, it describes how the setup can be built in practice, by presenting its main components. Moreover, the experimental procedures are also described.

5.1 Wind tunnel description

The experimental setup is supposed to be tested in the wind tunnel facilities of the University of Liège, which has its own subsonic wind tunnel in the Sart-Tilman site since 1999 [81].

Table 5.1 summarizes the main characteristics of the test section 1, which is used in the scope of this experimental campaign. This test section is mainly dedicated to aeronautical applications.

Parameter	Value
Speed range in close loop	2 - 60 m/s
Speed range in open loop	2 - 40 m/s
Turbulence level	0.15 %
Width	2 m
Height	1.5 m
Length	5 m

Table 5.1: Main characteristics of the test section 1 of the University of Liège wind tunnel capabilities [81].

This test section has a boundary layer suction device, allowing the uniformity of the incident flow near the ground. First, this device takes the boundary layer near the floor. Then, it releases it downstream of the test section.

5.2 Overview of the experimental setup

The experimental setup consists of a tubular pylon, on which the motor and the propeller are mounted. The propeller is described in detail in Section 4.1, while the pylon characteristics are defined in Table 4.6.

Additionally, the propeller and the motor are assembled through a specific connection, presented in Section 5.4.1. The connection between the tubular pylon and the motor, referred to as the motor support, is described in Section 5.4.2. A CAD representation of the experimental setup is shown in Figure 5.1, where the propeller is represented by a generic three-bladed model.

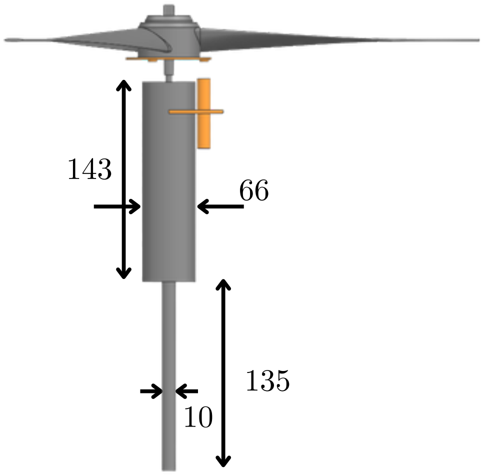

(a) Top view with key dimensions shown in mm.

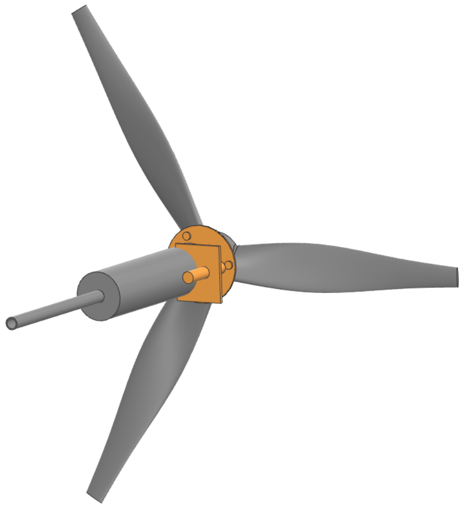

(b) Back view.

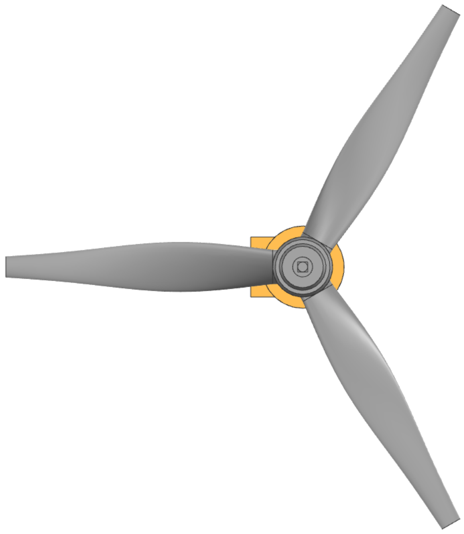

(c) Front view.

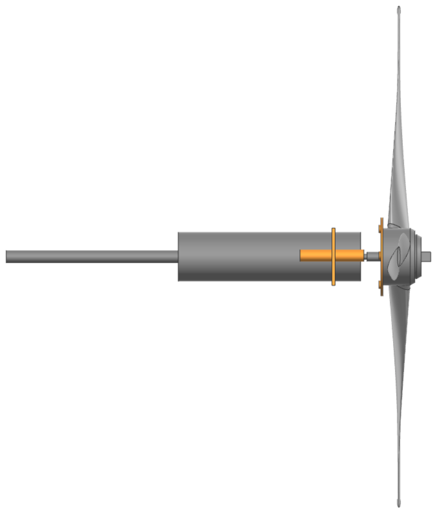

(d) Side view.

Figure 5.1: Top, back, side and front views of the experimental setup CAD with selected dimensions given in mm.

The different components of the setup are described in the following sections. The orange component corresponds to the tachometer support, which is presented in Section 5.6.

Wind tunnel integration

The experimental setup requires the pylon to be rigidly mounted on a rigid structure, in order to avoid unwanted flexibility. This rigid structure is considered as a vertical cylinder, on top of which a small plate is mounted, made of aluminium, for example.

Two U-shaped clamps are fixed on this plate in order to rigidly hold the circular pylon tube. This assembly, referred to as the pylon support, is shown in Figure 5.2.

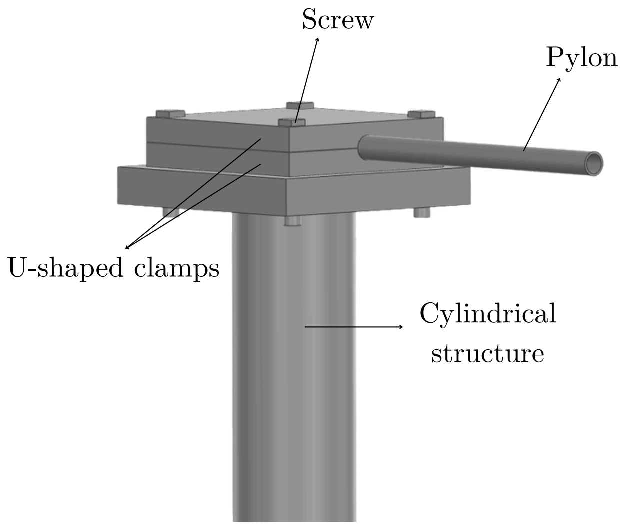

Figure 5.2: Pylon support.

5.3 Motor description

The motor is selected in order to rotate the propeller at $\Omega = 2000$ rpm for a free-stream velocity up to 13 m/s. It must be able to provide the torque required by the operating conditions identified in Section 4.3.4. The corresponding torque values are found in Table D.2.

A brushed DC motor is selected for this purpose. Its main characteristics are listed in Table 5.2.

Parameter	Value
Rotational velocity range	3000 rpm - 6000 rpm
Input voltage range	12 V - 24 V
Mass	496 g
Shaft diameter	5 mm
Diameter (with magnetic ring)	50 mm
Total length	102 mm

Table 5.2: Key parameters of the selected motor.

Pictures of the motor with its main geometrical dimensions are shown in Figure 5.3.

(a) Side view.

(b) Back view, where the power cables are connected.

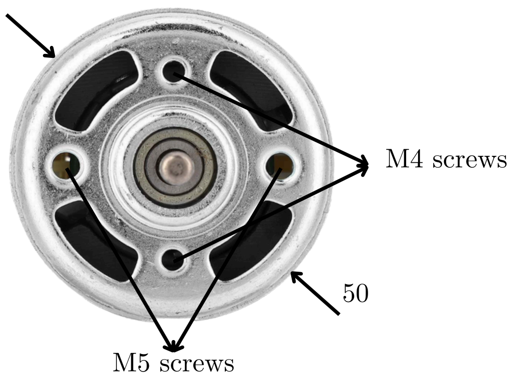

(c) Front view, with the four mounting-screws locations.

(d) Top view of the motor with key dimensions shown in mm.

Figure 5.3: Side, back, top and front views of the motor, with important dimensions shown in mm.

Furthermore, a heat dissipation study could be conducted in order to estimate the motor temperature during operation. This would be useful to confirm that the motor remains compatible with the pylon and motor support materials.

5.4 Motor integration

The motor is placed at the pylon tip, between the pylon and the propeller. Therefore, it must be connected to both components through rigid links, in order to avoid adding unwanted flexibility to the system. The motor-propeller and motor-pylon connections are described in Sections 5.4.1 and 5.4.2, respectively.

5.4.1 Motor-propeller connection

Since the motor shaft and propeller hub have different diameters, they cannot be directly connected. Therefore, a propeller adapter is required. This component is shown in Figure 5.4.

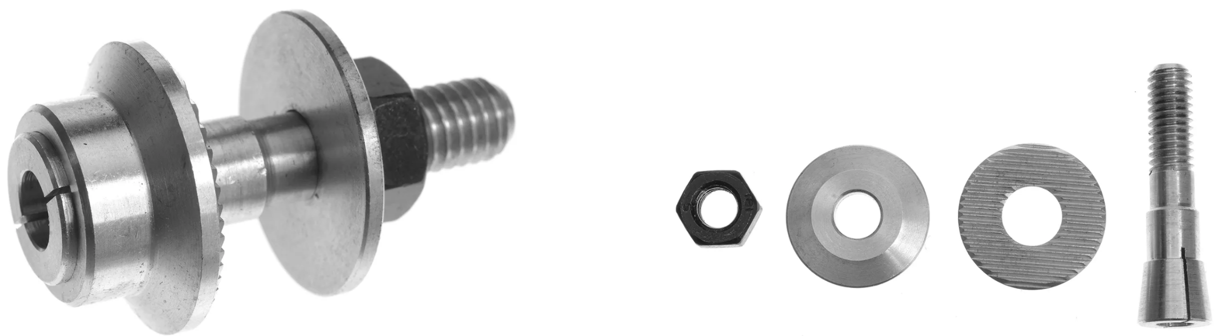

(a) Assembled propeller adapter.

(b) Components of the propeller adapter.

Figure 5.4: Propeller adapter.

This component is designed to receive the 5 mm diameter motor shaft on its left side, and to connect it to the propeller through a threaded rod of suitable length. The propeller adapter is mounted on the motor shaft. Once the assembly is properly tightened, the adapter clamps onto the shaft, creating a compressive force exerted by the adapter on the motor shaft. This prevents relative motion between both and ensures a rigid connection between the propeller and the motor shaft.
The characteristics of this device are given by Table 5.3.

Parameter	
Material	Steel
Motor shaft diameter	5 mm
Thread size	M6
Propeller shaft diameter	7 mm
Length	34 mm
Propeller maximum hub thickness	19 mm

Table 5.3: Propeller adapter key parameters.

Therefore, this component theoretically suits the selected motor and propeller perfectly. However, this is not fully the case in practice. A small clearance of 0.5 mm exists between the adapter and the motor shaft. To solve this issue, a sleeve can be manufactured in order to adapt the propeller shaft diameter to the adapter inner diameter. This sleeve, possibly made of aluminium, has the same holes as the adapter, so that both components can be properly assembled.

Another issue concerns the actual diameter of the threaded rod, which is too large for the propeller hub. Therefore, slightly increasing the diameter of the central hole of the propeller appears to be a simple way to solve this problem.

5.4.2 Motor-pylon connection

Since the motor is equipped with cooling fans, the support cannot fully surround the motor without openings allowing heat to be dissipated towards the environment.
This part is a 3D-printed component, and is made of polyethylene terephthalate glycol (PETG). This material provides higher strength than polylactic acid (PLA), for example, which is another well-know material commonly used for 3D-printing. PETG also has a heat resistance of approximately 70° to 80° and good toughness compared to other 3D-printing materials [82, 83].

The support has a cylindrical shape in order to fit the motor and pylon geometries, while preserving the symmetry of the system. It surrounds both the motor and the end of the pylon. An opening is made at the motor shaft location in order to allow the connection with the motor-propeller link. The support is attached to the motor with 4 screws, two M4 and two M5, using the four mounting holes already present on the motor.
In order to obtain a rigid motor-pylon connection, the pylon is inserted into the motor support over a length of 30 mm. This contact length provides sufficient longitudinal support, and the pylon is glued inside the support to prevent relative motion between both components.
The wall thickness of the support is 5 mm. Figure 5.5 illustrates this component. Additionally, a plastic sleeve is manufactured in order to rigidly connect the PVC pylon to the motor.

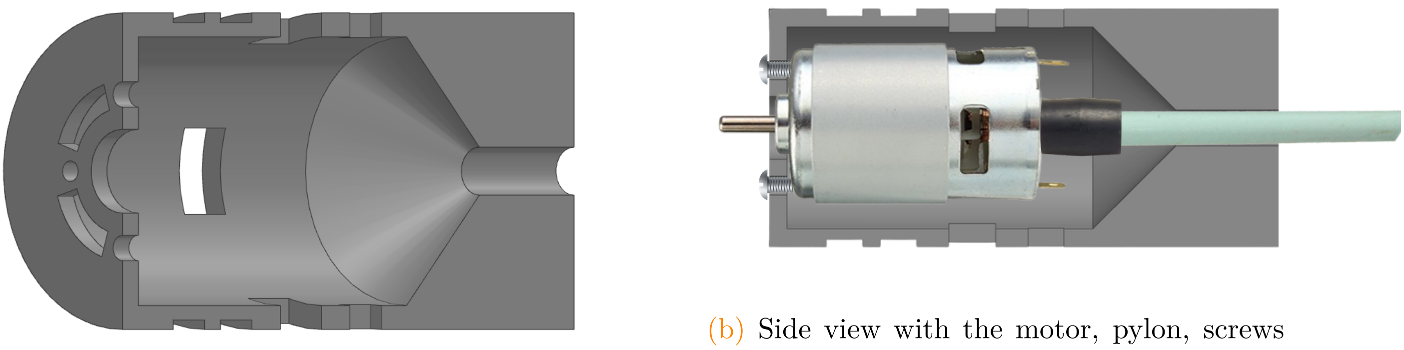

(a) Side view of a section.

(b) Side view with the motor, pylon, screws and plastic sleeve integrated into it.

Figure 5.5: Motor support.

Furthermore, the support is divided into two parts in order to allow the motor to be inserted. Both parts are assembled by two metallic clamps. This is the reason why the support is grooved by

2 mm around its entire circumference, allowing the clamps to be properly fitted.

Additionally, the technical drawing of the motor support, including its main dimensions, is provided in Figure F.1 of Appendix F.

5.4.3 Rotational speed control

To control the rotational speed of the motor, and, therefore, of the propeller, a DC pulse width modulation (PWM) device is selected. Without this device, the rotational speed of the motor would mainly depend on the applied voltage, which is not desirable for proper control because the achievable speed range would be limited and the supply voltage cannot always be varied.

The principle of this device is important for rotational speed management. It applies the full supply voltage, but not continuously. Indeed, the applied voltage is periodically switched on and off. Therefore, the motor is driven by an average voltage, which depends on the fraction of time during which the voltage is applied. The rotational speed is then controlled by varying this fraction, called the duty cycle [84]. The voltage amplitude is determined by the selected motor, and then ranging from 12 V to 24 V, depending on the rotational speed to be achieved.

Figure 5.6 illustrates this device.

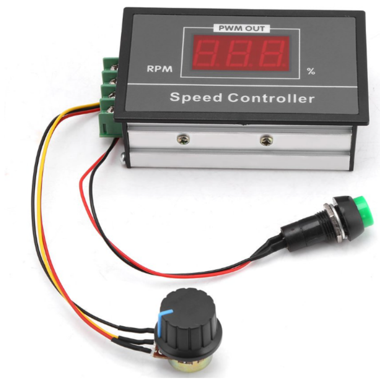

Figure 5.6: Pulse width modulation (PWM) device for motor rotational speed control.

Additionally, the PWM device can be used for 12 V, 24 V, 36 V, and even 48 V systems. It is equipped with a start/stop button and a display indicating the duty cycle, i.e. the percentage of time during which the voltage is applied to the motor. Table 5.4 provides additional technical information about the device. In this table, the control frequency corresponds to the frequency of the signal sent by the PWM device to the motor.

Parameter	
Maximum output current	30 A
Maximum continuous output current	20 A
Control frequency	15 kHz

Table 5.4: Additional technical information about the pulse width modulation (PWM) device.

For example, Figure 5.7 shows the time evolution of the voltage supplied to the motor for a 24 V supply voltage and a 50% duty cycle.

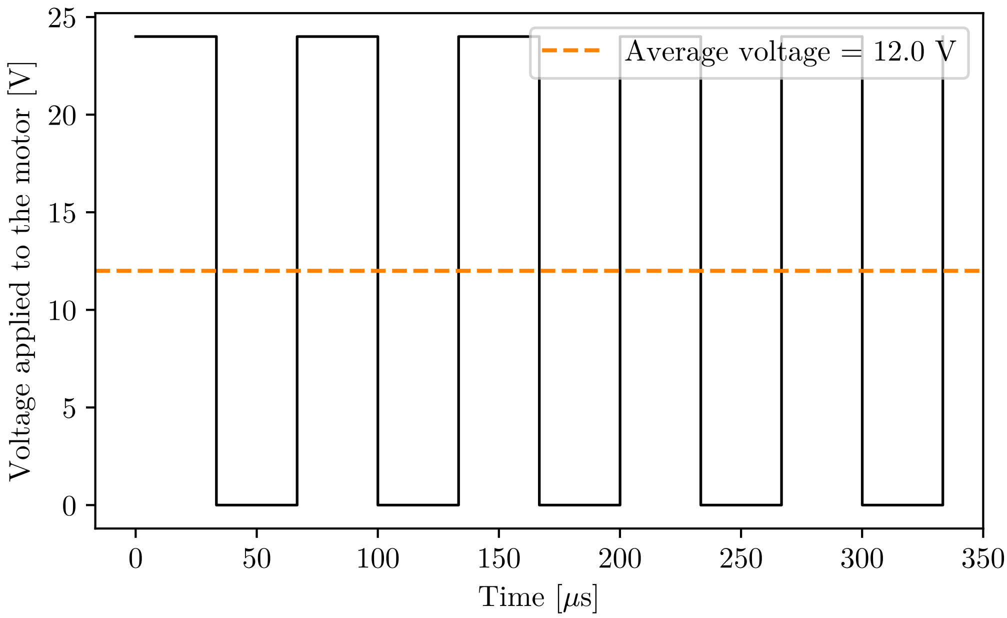

Figure 5.7: PWM voltage signal applied to the motor with a 24 V supply voltage and a duty cycle of 50%.

5.5 Propeller balancing

APC Propellers states that their manufactured propellers are well balanced. Nevertheless, it recommends checking the propeller balance before use in order to prevent unwanted behaviour during the experimental campaign.

Therefore, the balance of the APC 15.75x13-3 propeller is tested using a propeller balancer, which is illustrated in Figure 5.8a. The propeller mounted on the balancer for the balance test is shown in Figure 5.8b.

(a) Propeller balancer.

(b) APC 15.75x13-3 propeller on the propeller balancer.

Figure 5.8: APC 15.75x13-3 propeller balancing procedure.

A properly balanced propeller should remain at rest when released from any angular position. For the present case, it can therefore be concluded that the propeller is correctly balanced.

5.6 Rotational speed measurement

The propeller rotational speed can be measured using a magnetic tachometer. When the magnet is in front of the sensor, it induces a variation of the magnetic field variation and the sensor generates a current pulse. A picture of this device is shown in Figure 5.9.

Figure 5.9: Magnetic tachometer used to measure the rotational speed Ω of the propeller.

As the motor support diameter is too large compared with the propeller hub diameter, an additional rotating component is added in order to place the magnets. This component is integrated into the motor-propeller assembly, between the propeller and the screws, and rotates at the same speed as the propeller. It consists of a small circular plate on which three equally spaced small circulars magnet are glued. This component is referred to as the magnet support. A circular shape with three magnets is selected in order to limit the creation of an unbalance. Therefore, the measured rotational speed is three times the actual propeller rotational speed. This is not an issue, since the propeller is expected to rotate at 2000 rpm, while the maximum measurable rotational speed of the tachometer is 9000 rpm.

Concerning the tachometer, it is supposed to be glued to the motor support described in Section 5.4.2, in order to be aligned with the rotating magnet. The tachometer support surrounds half of the circumference of the motor support and has a thickness of 5 mm. It also includes a hole allowing the tachometer to pass through and to be fixed. This component is referred to as the tachometer support.
Both supports are represented in Figure 5.10, viewed from the rear side of the setup.

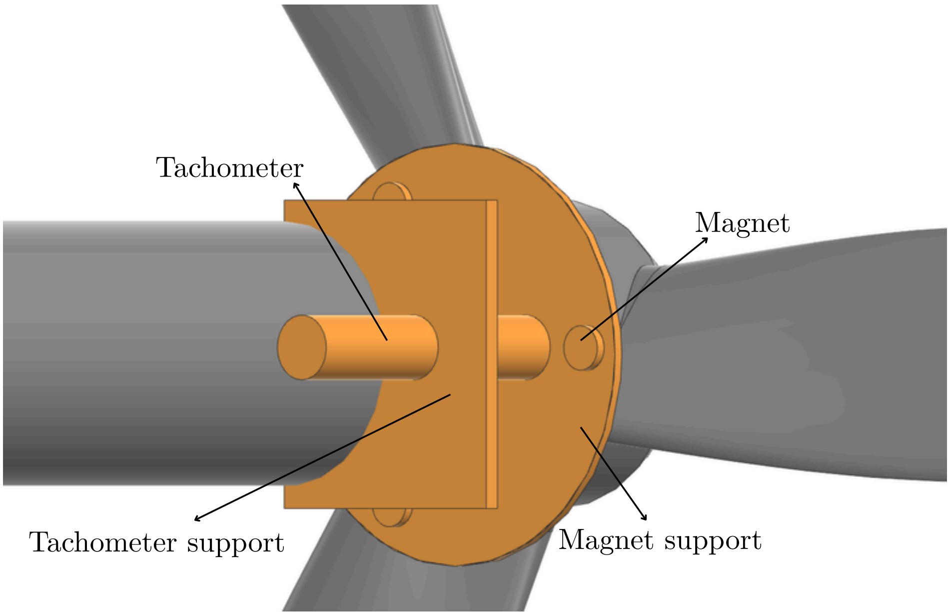

Figure 5.10: Focus on the tachometer and magnet supports, viewed from the back of the experimental setup.

Chapter 6. Conclusion and future work

This work provides an analytical study for the preliminary design of a small-scale pylon-propeller demonstrator aiming to observe the whirl flutter phenomenon. Two possible sources of structural flexibility are compared for the APC 15.75x13-3 propeller rotating at 2000 rpm, over a free-stream velocity range from 7 m/s to 13 m/s: a flexible pylon configuration and a rigid pylon configuration with linear traction springs.

Furthermore, the experimental setup associated with the flexible pylon configuration is investigated. The main components required for the assembly are studied and designed, including the pylon-motor and motor-propeller connections. The control and measurement of the propeller rotational speed are also discussed.

6.1 Overview of the findings

The analytical method was implemented by deriving the equations of motion, applying a Coleman transformation, and using eigenvalue analysis with mode tracking to identify the forward and backward whirling modes.

For both configurations, the results showed that only the backward whirling mode leads to whirl flutter, while the forward mode remains stable as the free-stream velocity increases. This behaviour was understood through the computation of the aerodynamic work over one oscillation period for both modes.

For the forward whirling mode, the aerodynamic work remains negative over the considered free-stream velocity range, meaning that the aerodynamic forces extract energy from the modal motion and therefore have a stabilizing effect.

In contrast, for the backward whirling mode, the aerodynamic work becomes positive above a given free-stream velocity. In this case, the aerodynamic forces transfer energy to the structure, leading to the onset of whirl flutter.

Beyond the stability behaviour, the mechanical feasibility of both configurations was also assessed.

For the flexible pylon configuration, the pylon design is governed by a trade-off between the flexibility required to obtain whirl flutter and the static rigidity required to limit the tip deflection and rotation under the motor-propeller assembly weight. The selected PVC pylon allows the instability to be theoretically observed within the considered free-stream velocity range, while keeping the static deformation acceptable for the experimental setup.

For the rigid pylon configuration with linear traction springs, the system flexibility is introduced by the springs while the pylon itself remains rigid. This configuration significantly reduces the static tip deflection and rotation of the pylon, but requires an appropriate initial elongation of the vertical springs to compensate for the elongation induced by the system weight. The results show that whirl flutter can also be obtained with this spring-based configuration, which highlights the interest of decoupling the system flexibility from the pylon rigidity.

The comparison between both configurations showed that the source of flexibility has a major influence on the experimental feasibility of the setup. Although the flexible pylon configuration is conceptually simpler, it can be more difficult to implement experimentally because of the motor-pylon connection and the significant static tip deflection and rotation. Moreover, its flexibility cannot be tuned independently from other design parameters, since changing the pylon length also affects its mass, transverse inertia, and static behaviour. In contrast, the spring-based configuration is more modular, as the stiffness can be adjusted through the spring stiffness or attachment position without modifying the pylon geometry. However, this modularity comes with additional design considerations, especially concerning the choice of the springs, their attachment to the pylon, and the flexible mount located at the pivot point.

Finally, the flexible pylon configuration was selected for the preliminary experimental design. Although no wind tunnel results are provided in the present work, the setup is designed to be tested in the wind tunnel facilities of the University of Liège. The main components required for the experimental assembly were defined, including the pylon support, the motor-propeller connection, the motor support, the propeller balancing procedure, and the rotational speed control and measurement systems.

6.2 Limitations

The analytical results obtained in this work must be interpreted with respect to the assumptions introduced in the model. The propeller is assumed to be composed of equally spaced identical blades made of a homogeneous material. For the computation of the structural matrices, the blades are modelled as untwisted beams with cross-sections varying along the radius. Additionally, the Euler-Bernoulli beam assumption is used. Therefore, the analytical results are mainly valid near the onset of the instability, where displacements and rotations can still be assumed to remain small.

Additionally, the structural damping is also introduced in a simplified way. In practice, damping can come from several sources, such as the material, the motor support, glued connections, or other mechanical interfaces. These contributions are difficult to estimate accurately and are not modelled separately in the analytical formulation. Moreover, possible nonlinear effects are neglected.

Furthermore, the aerodynamic forces applied on the propeller blades, as well as the induced velocities associated with the propeller rotation are computed using a quasi-steady aerodynamic approach. They are based on blade element and blade element momentum theories, which are two-dimensional approaches neglecting unsteady effects and spanwise flow over the blades. These methods are also difficult to apply near the propeller hub, where the blade geometry becomes unconventional. Moreover, the method completely neglects the aerodynamic forces acting on the pylon and the aerodynamic interactions existing between the pylon and the propeller.

Finally, the experimental part of this work remains limited to the preliminary design of the setup, since no wind tunnel tests were performed.

6.3 Future work

As a first step, the flexible pylon setup designed in this work should be experimentally tested in order to verify if the predicted whirl flutter behaviour can be observed in practice.
Before performing wind tunnel tests, additional mechanical checks should also be conducted. In particular, a stress analysis of the pylon would be required to ensure that it can sustain the expected loads without failure. Moreover, a heat dissipation study of the motor should be performed to estimate its operating temperature and verify its compatibility with the pylon and motor support materials.

Considering the assumptions of the analytical method, the prediction of the whirl flutter boundaries could first be improved by introducing an unsteady aerodynamic model. This would reduce the uncertainty associated with the predicted wind tunnel behaviour. Moreover, it would be relevant to experimentally measure the stiffnesses, inertias and structural damping coefficients of the setup in order to integrate more accurate parameters into the analytical model. The natural frequencies of the system could also be measured experimentally and compared with the analytical prediction to asses the reliability of the method in the present case.
Furthermore, a more detailed analysis of nonlinear effects would be required to improve the analytical estimates.

Additionally, the propeller-pylon system could be upgraded by introducing a tilt mechanism in order to approach a tiltrotor aircraft configuration more closely. This would improve the understanding of the whirl flutter mechanism configurations closer to current research applications, such as tiltrotor aircraft.

Future work should investigate other operational conditions, such as different propeller rotational speeds and free-stream velocities, in order to better assess their influence on the whirl flutter stability boundaries.

Finally, the spring-based configuration could be experimentally investigated in order to identify its advantages and its main differences with respect to the flexible pylon configuration. Experimental setups of both configurations could also be compared in order to determine if the spring-based configuration can reproduce the same instability mechanisms as the flexible pylon model, while allowing the static orientation of the propeller plane to be controlled more easily.

Bibliography

[1] Jordi Pons-Prats, Tanja Živojinović, and Jovana Kuljanin. "On the understanding of the current status of urban air mobility development and its future prospects: Commuting in a flying vehicle as a new paradigm". In: *Transportation Research Part E* 166 (Aug. 2022). ISSN: 13665545. DOI: 10.1016/j.tre.2022.102868.

[2] Laurie A. Garrow, Brian J. German, and Caroline E. Leonard. "Urban air mobility: A comprehensive review and comparative analysis with autonomous and electric ground transportation for informing future research". In: *Transportation Research Part C* 132 (Oct. 2021). ISSN: 0968090X. DOI: 10.1016/j.trc.2021.103377.

[3] World Intellectual Property Organization. "Future of transportation in the air". In: (202). DOI: 10.34667/tind.57971.

[4] Joby Aviation. *Technology: Joby Aircraft*. 2026. URL: https://www.jobyaviation.com/technology (visited on 05/19/2026).

[5] EHang. *EHang 216L: Heavy-Cargo Pilotless Aircraft*. 2026. URL: https://www.ehang.com/ehang216l/ (visited on 05/19/2026).

[6] A. R. Collar. "The Expanding Domain of Aeroelasticity". In: *The Journal of the Royal Aeronautical Society* 50 (428 June 1946). ISSN: 0368-3931. DOI: 10.1017/s0368393100120358.

[7] Jiri Cecrdle. *Whirl flutter of turboprop aircraft structures*. Ed. by Sara Greco. 2nd ed. Matthew Deans, 2023. ISBN: 978-0-323-95556-0.

[8] E. S. Taylor and K. A. Browne. "Vibration Isolation of Aircraft Power Plants". In: *Journal of the Aeronautical Sciences* 6 (2 Dec. 1938). DOI: 10.2514/8.760.

[9] F.W. Lanchester. *The flying machine from an engineering standpoint*. Princeton University Library, 1917.

[10] Wilmer H Reed. *Review of propeller-rotor whirl flutter*. Tech. rep. NASA, July 1967.

[11] Wilmer H Reed. *Aeroelasticity matters: some reflections on two decades of testing in the NASA Langley transonic tunnel*. Tech. rep. NASA, Sept. 1981.

[12] Charles Jacquet, Camille Denoël, and Loïc Salles. "Computational Methods for Whirl Flutter Analysis". In: *11th International Operational Modal Analysis Conference*. June 2025.

[13] *Propeller-rotor whirl flutter: A state-of-the-art review*. Tech. rep. NASA Langley Research Center, Sept. 1965.

[14] Vincent de Gaudemaris. "Development of low- to mid-fidelity models for the analysis of whirl flutter in rigid or flexible blade propellers". Phd thesis. Lyon, France: École Centrale de Lyon, 2025.

[15] Wilmer H Reed and Samuel R Bland. *An analytical treatment of propeller precession instability.* Tech. rep. National Aeronautics and Space Administration, Jan. 1961.

[16] Herbert S. Ribner. *Propellers in yaw.* Tech. rep. NACA report, 1945.

[17] Robert M Bennett and Samuel R Bland. *Experimental and analytical investigation of propeller whirl flutter of a power plant on a flexible wing.* Tech. rep. NASA, Aug. 1964.

[18] John L. Crigler and Jean Gilman. *Calculation of aerodynamic forces on a propeller in pitch and yaw.* Tech. rep. National advisory committee for aeronautics, Feb. 1949.

[19] David V. Swinney. "A fractional calculus model of aeroelasticity". PhD thesis. Air Force Institute of Technology Air University, Dec. 1989.

[20] Sahai Vireshwar and Tsao Chen-Pierce. *Use of Wagner functions in airfoil design optimization.* Tech. rep. Air force office of scientific research, Aug. 1979.

[21] Johan Boutet and Grigorios Dimitriadis. "Unsteady lifting line theory using the Wagner function for the aerodynamic and aeroelastic modeling of 3D wings". In: *Aerospace* 5 (Sept. 2018). ISSN: 22264310. DOI: 10.3390/aerospace5030092.

[22] Dan Zhao et al. *Wind turbines and aerodynamics energy harvesters.* Birtcher, Katey, 2019. Chap. 5, pp. 373–400. ISBN: 978-0-12-817135-6. DOI: 10.1016/C2018-0-01955-6.

[23] Jens Nørkaer Sørensen. *General Momentum Theory for Horizontal Axis Wind Turbines.* 1st ed. Vol. 4. Springer International Publishing Switzerland, Aug. 2016. ISBN: 978-3-319-22114-4. DOI: 10.1007/978-3-319-22114-4.

[24] Christopher Koch et al. "Comparison of Unsteady Low- and Mid-Fidelity Propeller Aerodynamic Methods for Whirl Flutter Applications". In: *Applied Sciences* 14 (Jan. 2024). ISSN: 20763417. DOI: 10.3390/app14020850.

[25] Samuel R Bland and Robert M Bennett. *Wind-tunnel measurement of propeller whirl-flutter speeds and static-stability derivatives and comparison with theory.* Tech. rep. NASA, Aug. 1963.

[26] Jiří Čečrdle et al. *W-WING aeroelastic demonstrator design modification and upgrade.* Tech. rep. Czech Aerospace Research Centre (VZLU), Jan. 2022.

[27] Clean Aviation. *OFELIA: Open Fan for Environmental Low Impact of Aviation.* 2026. URL: https://www.clean-aviation.eu/ofelia (visited on 05/18/2026).

[28] Jiri Cecrdle and Jaromir Malecek. *Design and development of new whirl flutter aeroelastic demonstrator*. Tech. rep. AIAA SciTech, Jan. 2014. DOI: 10.2514/6.2014-0678.

[29] Giuseppe M Gagliardi, Aniello D Marano, and Francesco Marulo. “Concept, development and testing of an experimental device for whirl flutter research”. In: *International forum on aeroelasticity and structural dynamics*. June 2022.

[30] C W Acree and Jr A L Sheikman. *Development and Initial Testing of the Tiltrotor Test Rig*. Tech. rep. NASA Ames Research Center, May 2018.

[31] Robert P Thornburgh et al. “An Experimental Parametric Study on the Whirl-Flutter Stability of Tiltrotors”. In: *Vertical Flight Society’s 81st Annual Forum & Technology Display*. May 2025.

[32] Andrew R Kreshock et al. “Initial Whirl-Flutter Characterization of the TiltRotor Aeroelastic Stability Testbed”. In: *Vertical Flight Society’s 79th Annual Forum & Technology Display*. May 2023.

[33] V. Heller. “Development of Wave Devices from Initial Conception to Commercial Demonstration”. In: *Comprehensive Renewable Energy* 8 (Jan. 2012), pp. 79–110. DOI: 10.1016/B978-0-08-087872-0.00804-0.

[34] Stefan van’t Hoff et al. “Whirl Flutter Testing of ATTILA Tiltrotor Testbed - Initial Results”. In: *Vertical Flight Society’s 80th Annual Forum and Technology Display*. May 2024.

[35] Hye Won Lee and Myung Il Roh. *Review of the multibody dynamics in the applications of ships and offshore structures*. Nov. 2018. DOI: 10.1016/j.oceaneng.2018.08.022.

[36] Steve Zhengjie Jia, Jay S. Gunasekera, and James Glancey. “Computer integrated sustainable manufacturing”. In: *Sustainable Manufacturing Processes*. Elsevier, Jan. 2022, pp. 313–334. ISBN: 9780323999908. DOI: 10.1016/B978-0-323-99990-8.00001-1.

[37] Hyeonsoo Yeo, Hao Kang, and Andrew R Kreshock. “Modeling and Analysis of Proprotor Whirl Flutter”. In: *Vertical Flight Society’s 77th Annual Forum & Technology Display*. May 2021.

[38] Jonathan Melvin and Caroline Raick. “Advances in resonance and cyclic symmetry on bladed rotor assemblies - Simcenter 3D 2306”. In: (June 2023).

[39] Jennifer Heeg et al. “Whirl flutter and the development of the NASA X-57 Maxwell”. In: *International forum on aeroelasticity and structural dynamics*. June 2019.

[40] Hyeonsoo Yeo et al. “Comparison of CAMRAD II and RCAS predictions of tiltrotor aeroelastic stability”. In: *Journal of the American Helicopter Society* 63 (2 Apr. 2018). ISSN: 00028711. DOI: 10.4050/JAHS.63.022001.

[41] M. Rafiee, F. Nitzsche, and M. Labrosse. “Dynamics, vibration and control of rotating composite beams and blades: A critical review”. In: *Thin-Walled Structures* 119 (Oct. 2017), pp. 795–819. ISSN: 02638231. DOI: 10.1016/j.tws.2017.06.018.

[42] Kelly Piaras. “The principle of virtual work and power”. In: *Solid Mechanics Part 3*. University of Auckland, pp. 369–381.

[43] Sinniah Ilanko and Luis E. Monterrubio. *The RayleighRitz Method for Structural Analysis*. Ed. by Noël Challamel. 1st ed. ISTE Ltd and John Wiley & Sons, Inc., 2014. ISBN: 978-1-84821-638-9.

[44] Herbert Goldstein, Charles P. Poole, and John Safko. *Classical mechanics*. 3rd ed. Pearson Education, Inc., 2002. ISBN: 978-81-317-5891-5.

[45] Alexander S. Poznyak. “Rigid body kinematics”. In: *Classical and Analytical Mechanics*. Elsevier, 2021, pp. 31–88. DOI: 10.1016/b978-0-32-389816-4.00013-2.

[46] J.L. Meriam and L.G. Kraige. *Engineering mechanics - dynamics*. Ed. by Linda Ratts. 7th ed. Vol. 2. John Wiley & Sons, Inc., 2012. ISBN: 978-04-706-1481-5.

[47] Richard Gentle, Peter Edwards, and Bill Bolton. “Statics”. In: *Mechanical Engineering Systems*. Elsevier, 2001, pp. 204–294. ISBN: 978-0-7506-5213-1. DOI: 10.1016/b978-075065213-1/50005-2.

[48] Giancarlo Genta and Mario Silvagni. “On centrifugal softening in finite element method rotor-dynamics”. In: *Journal of Applied Mechanics, Transactions ASME* 81 (1 2014). ISSN: 00218936. DOI: 10.1115/1.4024073.

[49] Bauchau O.A. and Craig J.I. *Structural Analysis - with applications to aerospace structures*. Ed. by Gladwell G.M.L. Vol. 163. Springer Science, 2009. ISBN: 978-90-481-2516-6.

[50] Lokanna Hoskoti, Shakti S. Gupta, and Mahesh M. Sucheendran. *Modeling of geometrical stiffening in a rotating blade—A review*. Dec. 2022. DOI: 10.1016/j.jsv.2022.117526.

[51] Bogdan Pamfil, Henrik Bredmose, and Taeseong Kim. “Coleman-free aero-elastic stability methods for three- and two-bladed floating wind turbines”. In: *Wind Energy Science* 10 (4 Apr. 2025), pp. 827–856. ISSN: 23667451. DOI: 10.5194/wes-10-827-2025.

[52] G S Bir. *User’s Guide to MBC3: Multi-Blade Coordinate Transformation Code for 3-Bladed Wind Turbines*. Tech. rep. U.S. Department of Energy, Sept. 2010.

[53] G Bir. *Multiblade Coordinate Transformation and Its Application to Wind Turbine Analysis: Preprint*. Tech. rep. ASME Wind Energy Symposium Reno, Jan. 2008.

[54] Koen Hillewaert. *Propeller Engines*. Lecture notes, AERO0014-1 – Aerospace Propulsion. Academic year 2024–2025. Liège, 2025.

[55] Snorri Gudmundsson. *General Aviation Aircraft Design: Applied Methods and Procedures*. Butterworth-Heinemann, 2014. Chap. 14, pp. 581–659. ISBN: 978-0-12-397308-5. DOI: 10.1016/C2011-0-06824-2.

[56] Chi-Tsong. Chen. *Linear system theory and design*. 3rd ed. Oxford University Press, 1999. ISBN: 0195117778.

[57] Hervé Abdi. “The Eigen-Decomposition: Eigenvalues and Eigenvectors”. In: *Encyclopedia of measurement and statistics* (2007).

[58] Xiaochen Hang, Qingguo Fei, and Weihua Su. “On tracking aeroelastic modes in stability analysis using left and right eigenvectors”. In: *AIAA Journal* 57 (10 July 2019), pp. 4447–4457. ISSN: 00011452. DOI: 10.2514/1.J057297.

[59] Michel Geradin and Daniel J. Rixen. *Mechanical Vibrations: Theory and Application to Structural Dynamics*. 3rd ed. Wiley, 2015. ISBN: 978-1-118-90020-8.

[60] Markus May, Yann Mauffrey, and Frédéric Sicot. *Numerical flutter analysis of turbomachinery bladings based on time-linearized, time-spectral time-accurate simulations*. Tech. rep. 2011.

[61] C. Reiber and M. Blocher. “Potential of Aeroelastic Tailoring to Improve Flutter Stability of Turbomachinery Compressor Blades”. In: *12th European Conference on Turbomachinery Fluid Dynamics and Thermodynamics*. Apr. 2017.

[62] Ming Wilson. “Mechanics: force, mass, acceleration energy, work, power”. In: *Anaesthesia and Intensive Care Medicine* 21 (5 May 2020). DOI: https://doi.org/10.1016/j.mpaic.2020.02.007.

[63] Randall J Allemang. *The Modal Assurance Criterion (MAC): Twenty Years of Use and Abuse*. Tech. rep. University of Cincinnati.

[64] R Jonker and A Volgenant. *Computing A Shortest Augmenting Path Algorithm for Dense and Sparse Linear Assignment Problems*. Tech. rep. May 1986.

[65] SciPy Developers. *scipy.optimize.linear_sum_assignment*. SciPy. 2026.

[66] APC Propellers. *About APC Propellers*. URL: https://www.apcprop.com/about/?v=d3dcf429c679 (visited on 05/14/2026).

[67] Airfoil Tools. *Airfoil Tools*. URL: http://airfoiltools.com/ (visited on 05/14/2026).

[68] Mark Drela and Harold Youngren. *XFOIL 6.9 User Primer*. 2001.

[69] John D Anderson. *Fundamentals of Aerodynamics*. Ed. by Lorraine K. Buczek and Bill Stenquist. 5th ed. McGraw-Hill, 2009. ISBN: 978-0-07-339810-5.

[70] Warren C.. Young and Richard G.. Budynas. *Roark's formulas for stress and strain*. 7th ed. McGraw-Hill, 2002. ISBN: 007072542X.

[71] Erik. Oberg et al. *Machinery's handbook*. Ed. by Christopher J. McCauley, Riccardo M. Heald, and Muhammed Iqbal Hussain. 27th ed. Industrial Press Inc., 2004. ISBN: 0831127007.

[72] Ferdinand P. Beer et al. *Vector mechanics for engineers - Statics and dynamics*. Ed. by Lora Neyens. 9th ed. McGraw-Hill Companies, 2010, p. 1326. ISBN: 0077275551.

[73] Mike Ashby. *Material and process charts*. Tech. rep.

[74] PTM. *Technical data sheet - rigid PVC*. URL: https://accwdev.co.uk/epdm-old/wp-content/uploads/2024/06/Rigid-PVC-Data-Sheet-Copy.pdf (visited on 05/28/2026).

[75] Joost de Vree. *Datasheet Polyvinyl chloride hard*. URL: https://www.joostdevree.nl/images/p/pvc_1_pvc-u_datasheet_www_designerdata_nl.pdf (visited on 05/28/2026).

[76] Armando Pérez-Peña et al. "A methodology for damping measurement of engineering materials: Application to a structure under bending and torsion loading". In: *JVC/Journal of Vibration and Control* 22 (10 June 2016), pp. 2471–2481. ISSN: 17412986. DOI: 10.1177/1077546314547728.

[77] J.P. Den Hartog. *Mechanical vibrations*. 3rd ed. McGraw-Hill book company, Inc., 1947.

[78] James M. Tinjum and Richard W. Christensen. "Site investigation, characterization and assessment for wind turbine design and construction". In: *Wind Energy Systems: Optimising Design and Construction for Safe and Reliable Operation*. Elsevier Ltd., 2011, pp. 28–45. ISBN: 9781845695804. DOI: 10.1533/9780857090638.1.28.

[79] Hydro Innovation and Technology. *Technical datasheet - Alloy EN AW-6082*. Tech. rep. 2023.

[80] Henri P Gavin. *Dynamics of Simple Oscillators*. Tech. rep. Duke University, 2026.

[81] *The University of Liège Wind Tunnel Facility*. Tech. rep. University of Liège, Dec. 2009.

[82] JLC3DP. *PETG Filament for 3D Printing: Properties and Settings Guide*. URL: https://jlc3dp.com/blog/petg-filament-guide (visited on 06/08/2026).

[83] Mohammad Taregh Sepahi et al. "Mechanical Properties of 3D-Printed Parts Made of Polyethylene Terephthalate Glycol". In: *Journal of Materials Engineering and Performance* 30.9 (2021), pp. 6851–6861. DOI: 10.1007/s11665-021-06032-4.

[84] *Motor Control*. Tech. rep. University of Michigan, Sept. 2008.

[85] James M. Gere and Barry J. Goodno. *Mechanics of materials*. Ed. by Randall Adams and Hilda Gowans. Brief edition. Shortt, Christopher M., 2012. ISBN: 978-1-111-13602-4.

Appendix A. Propeller aerodynamic matrices

The aerodynamic matrices are first written in the local aerodynamic variable space of each blade. In order to express these matrices in the generalized coordinate space of the isolated propeller, a coordinate transformation is introduced. Therefore, transformation matrices $\mathbf{T}_0(t)$, $\mathbf{T}_1(t)$, $\mathbf{T}_2(t)$ and $\mathbf{T}_3(t)$ are introduced.

For the derivation of $\mathbf{C}_{n,c}$, both matrices $\mathbf{T}_1(t)$ and $\mathbf{T}_2(t)$ are used. They are defined by:

$$\mathbf{T}_1 = \begin{pmatrix} \mathbf{0} & \mathbf{0} & \mathbf{0} & \mathbf{0} \\ \mathbf{0} & \mathbf{0} & \mathbf{0} & \mathbf{0} \\ \mathbf{0} & \mathbf{0} & \mathbf{P}_n^T & \mathbf{0} \\ \mathbf{0} & \mathbf{0} & \mathbf{0} & \mathbf{P}_n^T \end{pmatrix} \quad \text{and} \quad \mathbf{T}_2 = \begin{pmatrix} \mathbf{I} & \mathbf{0} & \mathbf{0} & \mathbf{0} \\ \mathbf{0} & \mathbf{I} & \mathbf{0} & \mathbf{0} \\ \mathbf{0} & \mathbf{0} & \mathbf{P}_n & \mathbf{0} \\ \mathbf{0} & \mathbf{0} & \mathbf{0} & \mathbf{P}_n \end{pmatrix}, \tag{A.1}$$

recalling that $\mathbf{P}_n$, defined in 3.30, denotes the rotation matrix between frame R_{b_n} and frame R_2.

Additionally, matrix $\mathbf{C}_n$ is given by:

$$\mathbf{C}_n = \begin{pmatrix} \int_{r_0}^{R} \mathbf{\Phi}^T \mathbf{Z}_{\dot{q}} \, dr & \mathbf{0} & \mathbf{0} & \mathbf{0} \\ \mathbf{0} & \mathbf{0} & \mathbf{0} & \mathbf{0} \\ \int_{r_0}^{R} \mathbf{Z}_{\dot{q}} \, dr & \mathbf{0} & \mathbf{0} & \mathbf{0} \\ \int_{r_0}^{R} r \mathbf{\Lambda}_{\mathbf{e}_y} \mathbf{Z}_{\dot{q}} \, dr & \mathbf{0} & \mathbf{0} & \mathbf{0} \end{pmatrix}, \tag{A.2}$$

where

$$\mathbf{Z}_{\dot{q}}(r) = \frac{1}{2}\rho_a a_l(r) c(r) \begin{pmatrix} -u_P^0 \, l_2 & 0 & u_P^0 \, l_1 + l_3 \\ 0 & 0 & 0 \\ -u_T^0 \, l_2 - l_3 & 0 & u_T^0 \, l_1 \end{pmatrix} \mathbf{\Phi} + \frac{1}{2}\rho_a C_d(r) c(r) \begin{pmatrix} -d_1 & 0 & d_3 \\ 0 & 0 & 0 \\ d_3 & 0 & -d_2 \end{pmatrix} \mathbf{\Phi}. \tag{A.3}$$

The air density is denoted by ρ_a, and l_1, l_2, l_3, d_1, d_2 as well as d_3 are notations introduced to simplify the equations. They are defined as follows:

$$\begin{cases} l_1 \ = \ (\gamma \ - \ \phi_0 \ - \alpha_0) \ \frac{u_P^0}{u_0} \ - \ \frac{u_T^0}{u_0} \\ l_2 \ = \ (\gamma \ - \ \phi_0 \ - \alpha_0) \ \frac{u_T^0}{u_0} \ + \ \frac{u_P^0}{u_0} \\ l_3 \ = \ (\gamma \ - \ \phi_0 \ - \alpha_0) \ u_0 \end{cases} \quad \text{and} \quad \begin{cases} d_1 \ = \ \frac{\left(u_T^0\right)^2}{u_0} \ + \ u_0 \\ d_2 \ = \ \frac{\left(u_P^0\right)^2}{u_0} \ + \ u_0 \\ d_3 \ = \ \frac{u_T^0 \ u_P^0}{u_0} \end{cases}, \tag{A.4}$$

where $u_0 \ = \ \sqrt{\left(u_P^0\right)^2 \ + \ \left(u_T^0\right)^2}$ and $\phi_0 \ = \ \arctan\left(\frac{u_P^0}{u_T^0}\right)$ are steady relative velocity and steady inflow angle of a blade section, respectively. α_0 is the zero-lift incidence angle of the blade section.

Moreover, $C_d(r)$, $c(r)$ and $a_l(r)$ respectively denote the drag coefficient, chord and the lift curve slope coefficient with compressible effects finite blade length correction of a blade section at a radial position r. The lift curve slope coefficient is written as:

$$a_l \ = \ a_0 \ C_{3D} \ C_{compr}, \tag{A.5}$$

with a_0 the blade section lift curve slope coefficient without any correction. On the one hand, when the blade Mach number does not exceed 0.3, the compressible effects correction C_{compr} is set to 1. On the other hand, the finite blade length correction is equal to:

$$C_{3D} \ = \ \frac{A \ \sqrt{1 \ - \ M^2}}{2 \ + \ A \ \sqrt{1 \ - \ M^2}} \tag{A.6}$$

with M the Mach number seen by the blade section, and $A \ = \ \frac{L^2}{S_{tot}}$ the blade aspect ratio. The total area of the blade is denoted by S_{tot} and L refers to the blade length. This correction comes from Houbolt and Reed's work, which used the Prandtl lifting line theory on an elliptical wing to establish this correction [14].

The remaining matrix used to derive $\mathbf{C}_{n,c}$ is $\mathbf{K}_n$, defined as follows:

$$\mathbf{K}_n = \begin{pmatrix} \int_{r_0}^{R} \Big(\mathbf{\Phi}^T \left(\mathbf{Z}_q - \mathbf{\Lambda}_{\mathbf{f}_p^{stat}} \mathbf{\Lambda}_{\mathbf{e}_y} \, \partial_r \mathbf{\Phi} \right) - \partial_r \mathbf{\Phi}^T \mathbf{\Lambda}_{\mathbf{e}_y}^T \mathbf{\Lambda}_{\mathbf{m}_p^{stat}} \mathbf{\Lambda}_{\mathbf{e}_y} \partial_r \mathbf{\Phi} \Big) \, dr & \int_{r_0}^{R} \left(\mathbf{\Phi}^T \left(\mathbf{Z}_t - \mathbf{\Lambda}_{\mathbf{f}_p^{stat}} \mathbf{e}_y \mathbf{\Phi}_t \right) \right) dr & \int_{r_0}^{R} \mathbf{\Phi}^T \mathbf{Z}_\nu \, dr & \int_{r_0}^{R} \mathbf{\Phi}^T \mathbf{Z}_\omega \, dr \\ - \int_{r_0}^{R} \mathbf{\Phi}_t^T \mathbf{e}_y^T \mathbf{\Lambda}_{\mathbf{m}_p^{stat}} \mathbf{\Lambda}_{\mathbf{e}_y} \, \partial_r \mathbf{\Phi} \, dr & \mathbf{0} & \mathbf{0} & \mathbf{0} \\ \int_{r_0}^{R} \left(\mathbf{Z}_q - \mathbf{\Lambda}_{\mathbf{f}_p^{stat}} \mathbf{\Lambda}_{\mathbf{e}_y} \, \partial_r \mathbf{\Phi} \right) dr & \int_{r_0}^{R} \left(\mathbf{Z}_t - \mathbf{\Lambda}_{\mathbf{f}_p^{stat}} \mathbf{e}_y \mathbf{\Phi}_t \right) dr & \int_{r_0}^{R} \mathbf{Z}_\nu \, dr & \int_{r_0}^{R} \mathbf{Z}_\omega \, dr \\ \int_{r_0}^{R} \Big(r \mathbf{\Lambda}_{\mathbf{e}_y} \left(\mathbf{Z}_q - \mathbf{\Lambda}_{\mathbf{f}_p^{stat}} \mathbf{\Lambda}_{\mathbf{e}_y} \, \partial_r \mathbf{\Phi} \right) - \mathbf{\Lambda}_{\mathbf{f}_p^{stat}} \mathbf{\Phi} - \mathbf{\Lambda}_{\mathbf{m}_p^{stat}} \mathbf{\Lambda}_{\mathbf{e}_y} \, \partial_r \mathbf{\Phi} \Big) \, dr & \int_{r_0}^{R} \left(r \mathbf{\Lambda}_{\mathbf{e}_y} \left(\mathbf{Z}_t - \mathbf{\Lambda}_{\mathbf{f}_p^{stat}} \mathbf{e}_y \mathbf{\Phi}_t \right) \right) dr & \int_{r_0}^{R} r \mathbf{\Lambda}_{\mathbf{e}_y} \mathbf{Z}_\nu \, dr & \int_{r_0}^{R} r \mathbf{\Lambda}_{\mathbf{e}_y} \mathbf{Z}_\omega \, dr \end{pmatrix}, \tag{A.7}$$

All the terms present in this matrix are defined below.

For instance, $\mathbf{f}_p^{stat}$ and $\mathbf{m}_p^{stat}$, respectively representing the steady force and torque on the blade profile, are defined by:

$$\mathbf{f}_p^{stat}(r) = \frac{1}{2}\rho_a a_l(r) c(r) \begin{pmatrix} u_P^0 l_3 \\ 0 \\ u_T^0 l_3 \end{pmatrix} + \frac{1}{2}\rho_a C_d(r) c(r) u_0 \begin{pmatrix} u_T^0 \\ 0 \\ -u_P^0 \end{pmatrix} \quad \text{and} \quad \mathbf{m}_p^{stat}(r) = \begin{pmatrix} 0 \\ m_0(r) \\ 0 \end{pmatrix} \tag{A.8}$$

where $m_0(r)$ is the static pitching moment of a blade section at a radial location r. The $\mathbf{\Lambda}$ matrix operator, defined in 3.23, is applied to these vectors.

Besides, all the other matrices introduced in $\mathbf{K}_n$ definition are defined as:

$$\mathbf{Z}_q(r) = \frac{1}{2}\rho_a a_l(r) c(r) \begin{pmatrix} 0 & \Omega \, u_P^0 \, l_2 & 0 \\ 0 & 0 & 0 \\ 0 & \Omega \left(u_T^0 \, l_2 + l_3 \right) & 0 \end{pmatrix} \mathbf{\Phi} + \frac{1}{2}\rho_a C_d(r) c(r) \begin{pmatrix} 0 & \Omega \, d_1 & 0 \\ 0 & 0 & 0 \\ 0 & -\Omega \, d_3 & 0 \end{pmatrix} \tag{A.9}$$

$$\mathbf{Z}_t(r) = \frac{1}{2}\rho_a a_l(r) c(r) \begin{pmatrix} V u_P^0 \, l_2 - r\Omega \left(u_P^0 \, l_1 + l_3 \right) \\ 0 \\ V \left(u_T^0 \, l_2 + l_3 \right) - r\Omega \, u_T^0 \, l_1 \end{pmatrix} \mathbf{\Phi}_t + \frac{1}{2}\rho_a C_d(r) c(r) \begin{pmatrix} V d_1 - r\Omega d_3 \\ 0 \\ -V d_3 + r\Omega d_2 \end{pmatrix} \mathbf{\Phi}_t \tag{A.10}$$

$$\mathbf{Z}_\nu(r) = \frac{1}{2}\rho_a a_l(r) c(r) \begin{pmatrix} -u_P^0 \, l_2 & 0 & u_P^0 \, l_1 + l_3 \\ 0 & 0 & 0 \\ -u_T^0 \, l_2 - l_3 & 0 & u_T^0 \, l_1 \end{pmatrix} + \frac{1}{2}\rho_a C_d(r) c(r) \begin{pmatrix} -d_1 & 0 & d_3 \\ 0 & 0 & 0 \\ d_3 & 0 & -d_2 \end{pmatrix} \tag{A.11}$$

$$\mathbf{Z}_{\omega}(r) \;=\; \frac{1}{2}\rho_a a_l(r)c(r)\begin{pmatrix} r\left(u_P^0\; l_1 \;+\; l_3\right) & 0 & ru_P^0\; l_2 \\ 0 & 0 & 0 \\ ru_T^0\; l_1 & 0 & r\left(u_T^0\; l_2 \;+\; l_3\right) \end{pmatrix} + \frac{1}{2}\rho_a C_d(r)c(r)\begin{pmatrix} rd_3 & 0 & rd_1 \\ 0 & 0 & 0 \\ -rd_2 & 0 & -rd_3 \end{pmatrix} \tag{A.12}$$

Once matrix $\mathbf{C}_{n,c}$ is fully defined, the remaining matrices involved in $\mathbf{K}_{n,c}$ can be defined. On the one hand, matrices $\mathbf{K}_n$ and $\mathbf{T}_2$ are the same as in the derivation of $\mathbf{C}_{n,c}$ and are respectively defined in Equations A.7 and A.1. On the other hand, both remaining transformation matrices $\mathbf{T}_3$ and $\mathbf{T}_0$ are given by:

$$\mathbf{T}_0(t) \;=\; \begin{pmatrix} \mathbf{I} & \mathbf{0} & \mathbf{0} & \mathbf{0} \\ \mathbf{0} & \mathbf{I} & \mathbf{0} & \mathbf{0} \\ \mathbf{0} & \mathbf{0} & \mathbf{0} & -\mathbf{P}_n^T\;\boldsymbol{\Lambda}_{\mathbf{v}_\infty} \\ \mathbf{0} & \mathbf{0} & \mathbf{0} & \mathbf{0} \end{pmatrix} \qquad \text{and} \qquad \mathbf{T}_3(t) \;=\; \begin{pmatrix} \mathbf{0} & \mathbf{0} & \mathbf{0} & \mathbf{0} \\ \mathbf{0} & \mathbf{0} & \mathbf{0} & \mathbf{0} \\ \mathbf{0} & \mathbf{0} & \mathbf{0} & -\boldsymbol{\Lambda}_{\mathbf{P}_n\mathbf{l}_n^c} \\ \mathbf{0} & \mathbf{0} & \mathbf{0} & \boldsymbol{\Lambda}_{\mathbf{P}_n\mathbf{l}_n^d} \end{pmatrix}, \tag{A.13}$$

with

$$\mathbf{l}_n^c \;=\; \int_{r_0}^{R_p} \mathbf{f}_p^{stat}\; dr \qquad \text{and} \qquad \mathbf{l}_n^d = \int_{r_0}^{R_p}\left(r\boldsymbol{\Lambda}_{\mathbf{e}_y}\mathbf{f}_p^{stat} \;+\; \mathbf{m}_p^{stat}\right)\; dr \tag{A.14}$$

where $\mathbf{f}_p^{stat}$ and $\mathbf{m}_p^{stat}$ are defined in Equation A.8.

Appendix B. Method verification plots

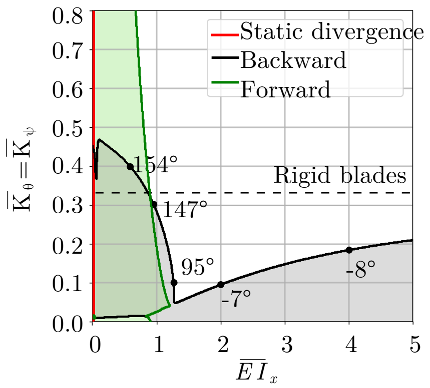

(a) Results obtained by V.de Gaudemaris [14].

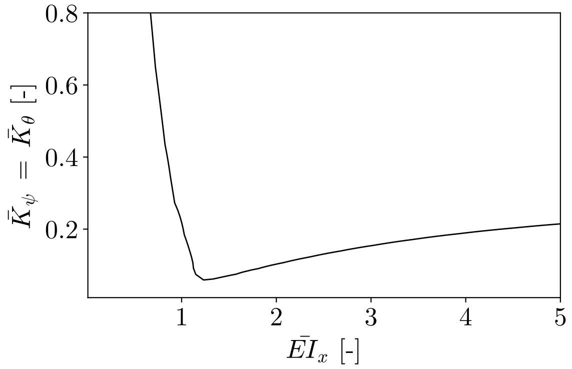

(b) Results obtained with the present implementation.

Figure B.1: Comparison between the considered implementation and the results of V.de Gaudemaris for the evolution of $\bar{K}_\theta = \bar{K}_\psi$ as functions of $\bar{EI}_x$ with aerodynamic effects, without prestress effects, and considering only the out-of-plane blade motion.

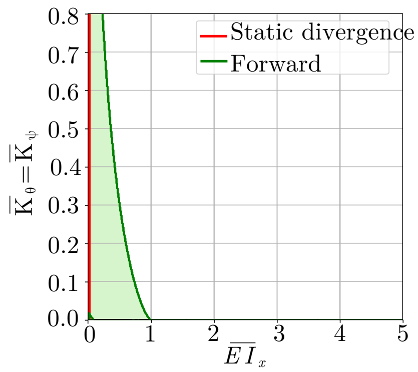

(a) Results obtained by V.de Gaudemaris [14].

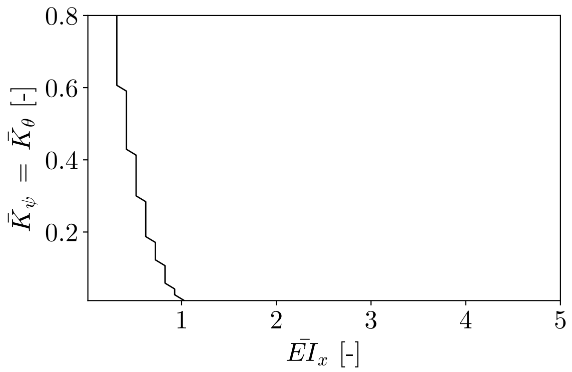

(b) Results obtained with the present implementation.

Figure B.2: Comparison between the considered implementation and the results of V.de Gaudemaris for the evolution of $\bar{K}_\theta = \bar{K}_\psi$ as functions of $\bar{EI}_x$ without aerodynamic effects, without prestress effects, and considering only out-of-plane blade motion.

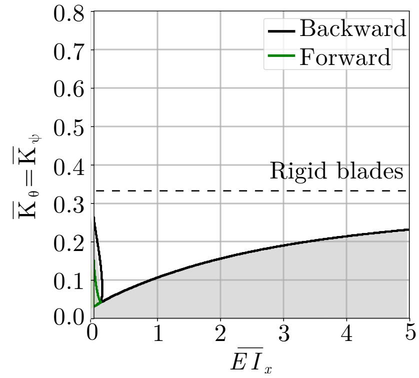

(a) Results obtained by V.de Gaudemaris [14].

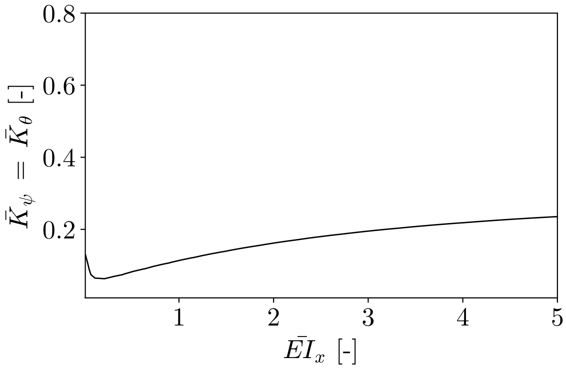

(b) Results obtained by the present implementation.

Figure B.3: Comparison between the considered implementation and the results of V.de Gaudemaris for the evolution of $\bar{K}_\theta = \bar{K}_\psi$ as functions of $\bar{EI}_x$ with aerodynamic effects, with prestress effects, and considering only the out-of-plane blade motion.

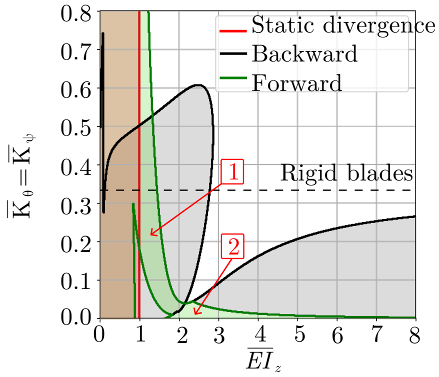

(a) Results obtained by V.de Gaudemaris [14].

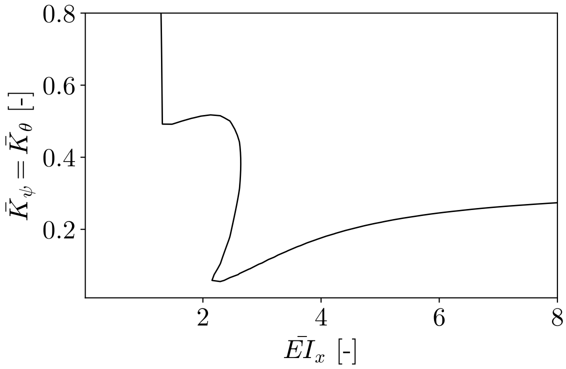

(b) Results obtained with the present implementation.

Figure B.4: Comparison between the considered implementation and the results of V.de Gaudemaris for the evolution of $\bar{K}_\theta = \bar{K}_\psi$ as functions of $\bar{EI}_z$ with aerodynamic effects, without prestress effects, and considering only the in-plane blade motion.

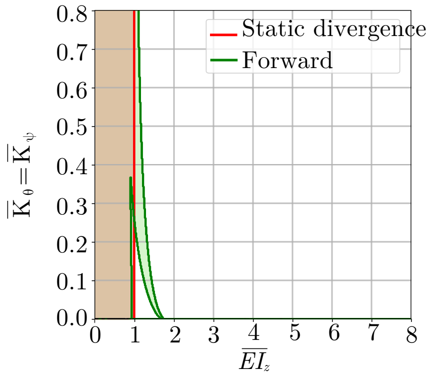

(a) Results obtained by V.de Gaudemaris [14].

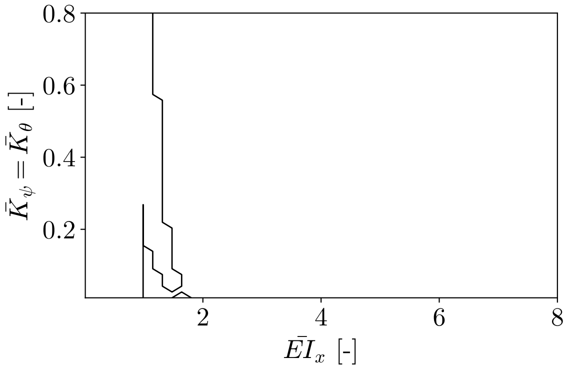

(b) Results obtained with the present implementation.

Figure B.5: Comparison between the considered implementation and the results of V.de Gaudemaris for the evolution of $\bar{K}_\theta = \bar{K}_\psi$ as functions of $\bar{EI}_z$ without aerodynamic effects, without prestress effects, and considering only in-plane blade motion.

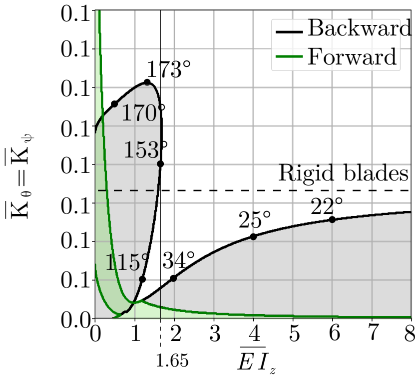

(a) Results obtained by V.de Gaudemaris [14].

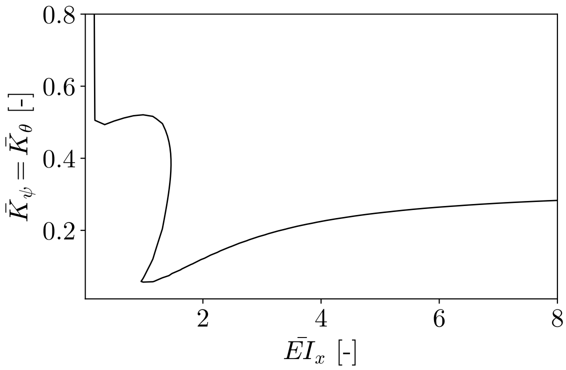

(b) Results obtained with the present implementation.

Figure B.6: Comparison between the considered implementation and the results of V.de Gaudemaris for the evolution of $\bar{K}_\theta = \bar{K}_\psi$ as functions of $\bar{EI}_z$ with aerodynamic effects, with prestress effects, and considering only in-plane blade motion.

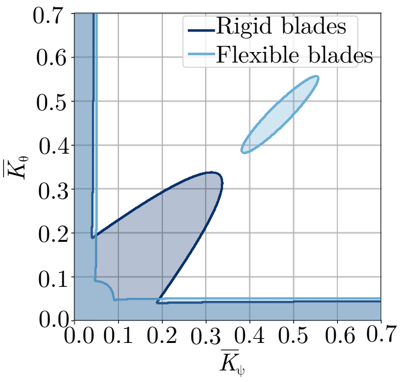

(a) Results obtained by V.de Gaudemaris [14].

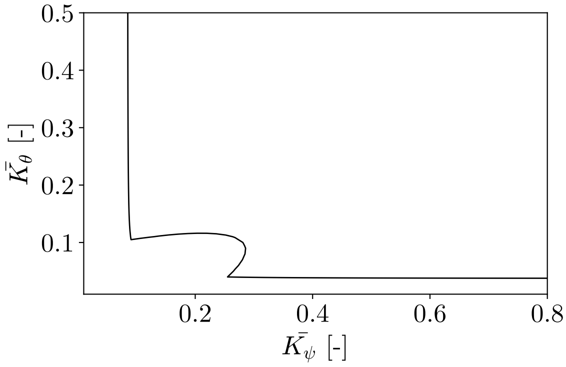

(b) Results obtained with the present implementation.

Figure B.7: Comparison between the considered implementation and the results of V.de Gaudemaris for the evolution of $\bar{K}_\theta$ as a function of $\bar{K}_\psi$ with aerodynamic effects, with prestress effects, and considering only in-plane blade motion.

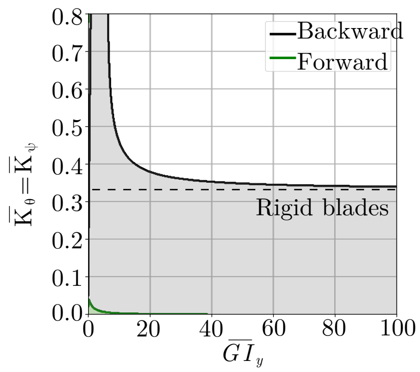

(a) Results obtained by V.de Gaudemaris [14].

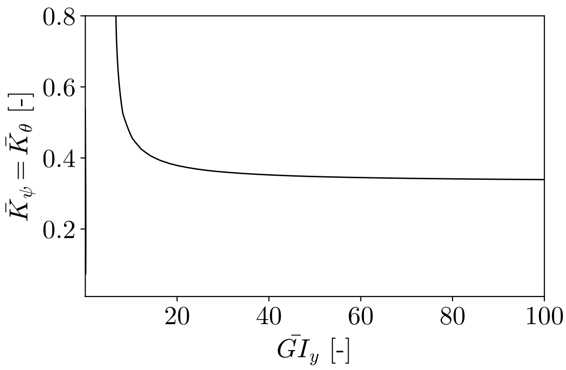

(b) Results obtained with the present implementation.

Figure B.8: Comparison between the considered implementation and the results of V.de Gaudemaris for the evolution of $\bar{K}_\theta = \bar{K}_\psi$ as functions of $\bar{GI}_y$ with aerodynamic effects, prestress effects, and considering only blade torsional motion.

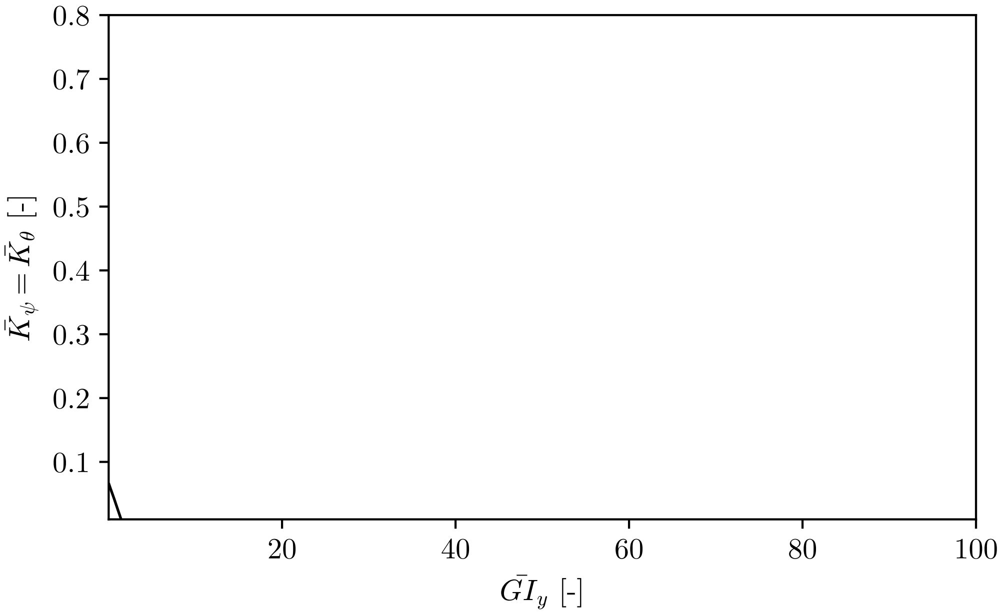

Figure B.9: Evolution of $\bar{K}_\theta = \bar{K}_\psi$ as functions of $\bar{GI}_y$ obtained by the present implementation without aerodynamic effects but with prestress effects, considering only torsion blade motion.

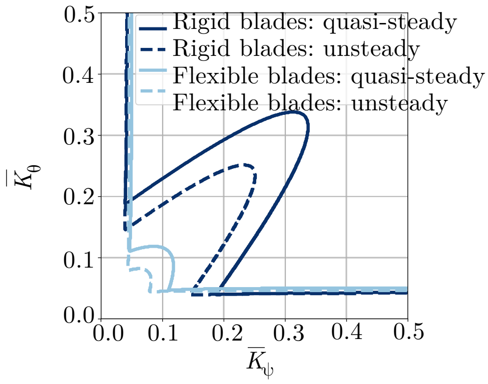

(a) Results obtained by V.de Gaudemaris [14].

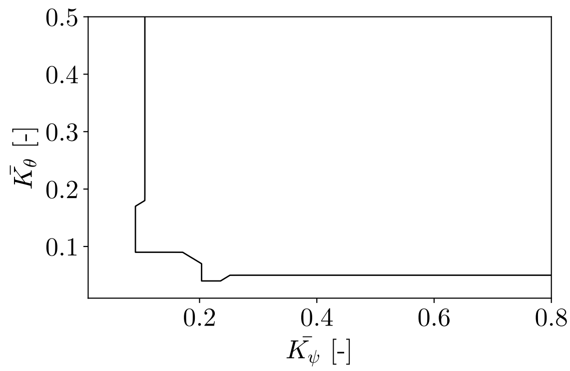

(b) Results obtained with the present implementation.

Figure B.10: Comparison between the considered implementation and the results of V.de Gaudemaris for the evolution of $\bar{K}_\theta$ as a function of $\bar{K}_\psi$ with aerodynamic effects, without prestress effect, and considering the fully-flexible blades.

Appendix C. Cantilever beam static deflection

A cantilever beam loaded at its tip by a concentrated force and a moment is represented in Figure C.1.

Figure C.1: Cantilever beam of length L loaded at its tip by a concentrated force F and a moment M_0.

According to the superposition theorem, force and moment contributions to δ and θ can be computed separately, and then added together as follows:

$$\delta = \delta_F + \delta_M \qquad \text{and} \qquad \theta = \theta_F + \theta_M. \tag{C.1}$$

The differential equation describing the deflection curve of a beam is the following [85]:

$$\frac{d^2 v}{dx^2} = \frac{M}{EI} \tag{C.2}$$

where v is the deflection, x the longitudinal coordinate of the beam, M the moment applied at its tip, and E and I the Young modulus and the bending beam inertia, respectively. Therefore, the tip deflection is $\delta = v(x = L)$.

Since a cantilever beam is considered, the following boundary conditions can be applied:

$$v(x = 0) = 0 \qquad \text{and} \qquad \left.\frac{dv}{dx}\right|_{x=0} = 0 \tag{C.3}$$

For an arbitrary beam position x, the moment generated by the concentrated tip force is given by

$M(x) = F(L - x)$, leading to, by successive integrations:

$$EI \frac{d^2v}{dx^2} = F(L - x) \tag{C.4}$$

$$\Rightarrow \frac{dv}{dx} = \frac{FL\,x}{EI} - \frac{FL\,x^2}{2EI} + C_1 \tag{C.5}$$

$$\Rightarrow v(x) = \frac{FL\,x^2}{2EI} - \frac{FL\,x^3}{6EI} + C_1 x + C_2 \tag{C.6}$$

where the integration constants C_1 and C_2 can be obtained from the boundary conditions of Equation C.3. Finally, it comes:

$$v(x) = \frac{F}{6EI}x^2\,(3L - x)\,, \tag{C.7}$$

and thus the beam tip deflection due to the concentrated force equals

$$\delta_F = v\,(x = L) = \frac{FL^3}{3EI}. \tag{C.8}$$

Following the small displacements assumption, the rotation equals

$$\theta = \frac{dv}{dx}. \tag{C.9}$$

Therefore, the beam tip angular deflection due to a concentrated load is equal to:

$$\theta_F = \frac{FL^2}{2EI} \tag{C.10}$$

For a moment M_0 applied on the cantilever beam, Equation C.2 becomes:

$$\frac{d^2v}{dx^2} = \frac{M_0}{EI}. \tag{C.11}$$

Similarly to the concentrated force case, the beam deflection and the rotation caused by a moment M_0 at the tip of a cantilever beam are given by:

$$\delta_M = \frac{M_0 L^2}{2EI} \qquad \text{and} \qquad \theta_M = \frac{M_0 L}{EI}. \tag{C.12}$$

And, finally, the total quantities equal:

$$\delta = \frac{FL^3}{3EI} + \frac{M_0 L^2}{2EI} \qquad \text{and} \qquad \theta = \frac{FL^2}{2EI} + \frac{M_0 L}{EI}. \tag{C.13}$$

Appendix D. Propeller performance

V [m/s]	Efficiency [-]	C_T [-]	C_P [-]	Power [W]	Torque [N.m]	Thrust [N]	M at the tip	Re at 75% of span
0.00	0	0.1702	0.0947	5.509	0.053	1.484	0.06	27875
0.23	0.06	0.1687	0.0963	5.602	0.053	1.472	0.06	27909
0.46	0.117	0.1671	0.0979	5.695	0.054	1.457	0.06	27946
0.68	0.1707	0.1652	0.0995	5.787	0.055	1.441	0.06	27986
0.92	0.2214	0.1631	0.1010	5.875	0.056	1.422	0.06	28031
1.14	0.2689	0.1607	0.1024	5.957	0.057	1.402	0.06	28079
1.37	0.3134	0.1580	0.1037	6.031	0.058	1.378	0.06	28132
1.60	0.3549	0.1550	0.1048	6.093	0.058	1.351	0.06	28189
1.83	0.3935	0.1515	0.1056	6.142	0.059	1.322	0.06	28250
2.06	0.4293	0.1477	0.1062	6.174	0.059	1.288	0.06	28316
2.28	0.4623	0.1435	0.1064	6.186	0.059	1.251	0.06	28387
2.51	0.4927	0.1388	0.1062	6.176	0.059	1.210	0.06	28462
2.74	0.5205	0.1336	0.1056	6.139	0.059	1.165	0.06	28541
2.97	0.5458	0.1279	0.1045	6.075	0.058	1.116	0.06	28625
3.20	0.5684	0.1218	0.1029	5.982	0.057	1.062	0.06	28714
3.43	0.5883	0.1153	0.1008	5.860	0.056	1.006	0.06	28807
3.66	0.6055	0.1084	0.0982	5.711	0.055	0.945	0.06	28905
3.88	0.6196	0.1012	0.0952	5.535	0.053	0.883	0.06	29007
4.11	0.6304	0.0937	0.0917	5.334	0.051	0.817	0.06	29114
4.34	0.6374	0.0860	0.0878	5.108	0.049	0.750	0.06	29225
4.57	0.6402	0.0780	0.0835	4.858	0.046	0.680	0.06	29340
4.80	0.6378	0.0698	0.0788	4.583	0.044	0.609	0.06	29460
5.03	0.6293	0.0615	0.0737	4.286	0.041	0.536	0.06	29584
5.26	0.6128	0.0530	0.0682	3.965	0.038	0.462	0.06	29712
5.49	0.5861	0.0444	0.0623	3.621	0.035	0.387	0.06	29845
5.71	0.5452	0.0356	0.0560	3.255	0.031	0.311	0.06	29982
5.94	0.4839	0.0268	0.0493	2.867	0.027	0.233	0.06	30123
6.17	0.3912	0.0179	0.0423	2.459	0.023	0.156	0.07	30268
6.40	0.2459	0.0089	0.0349	2.031	0.019	0.078	0.07	30417
6.63	0.0012	0.0000	0.0273	1.585	0.015	0.000	0.07	30570

Table D.1: Main performance parameters of the APC 15.75x13-3 propeller: efficiency, thrust coefficient C_T, power coefficient C_P, power, torque, thrust, Mach number M at the propeller tip and Reynolds number Re at 75% of the blade span as functions of the incoming velocity V at 1000 rpm [66].

V [m/s]	Efficiency [-]	C_T [-]	C_P [-]	Power [W]	Torque [N.m]	Thrust [N]	M at the tip	Re at 75% of span
0.00	0	0.1710	0.0867	40.323	0.193	5.966	0.12	55750
0.46	0.0663	0.1696	0.0884	41.104	0.196	5.916	0.12	55817
0.92	0.1288	0.1680	0.0900	41.891	0.200	5.860	0.12	55892
1.38	0.1876	0.1661	0.0917	42.669	0.204	5.795	0.13	55974
1.84	0.2427	0.1640	0.0933	43.422	0.207	5.722	0.13	56064
2.30	0.2942	0.1617	0.0949	44.131	0.211	5.640	0.13	56162
2.76	0.3422	0.1590	0.0962	44.774	0.214	5.546	0.13	56268
3.22	0.3868	0.1559	0.0974	45.330	0.216	5.440	0.13	56383
3.68	0.4281	0.1525	0.0984	45.774	0.219	5.320	0.13	56508
4.14	0.4664	0.1487	0.0991	46.082	0.220	5.186	0.13	56641
4.60	0.5017	0.1444	0.0994	46.229	0.221	5.037	0.13	56783
5.06	0.5341	0.1396	0.0993	46.188	0.221	4.871	0.13	56935
5.53	0.5639	0.1344	0.0987	45.936	0.219	4.688	0.13	57096
5.99	0.5911	0.1287	0.0977	45.453	0.217	4.488	0.13	57266
6.45	0.6157	0.1225	0.0962	44.731	0.214	4.272	0.13	57446
6.91	0.6377	0.1159	0.0941	43.773	0.209	4.042	0.13	57635
7.37	0.6571	0.1089	0.0915	42.584	0.203	3.798	0.13	57833
7.83	0.6738	0.1016	0.0885	41.173	0.197	3.544	0.13	58040
8.29	0.6874	0.0940	0.0850	39.546	0.189	3.280	0.13	58256
8.75	0.6977	0.0862	0.0811	37.707	0.180	3.007	0.13	58480
9.21	0.7043	0.0782	0.0767	35.661	0.170	2.727	0.13	58714
9.67	0.7062	0.0699	0.0718	33.409	0.160	2.440	0.13	58956
10.13	0.7027	0.0615	0.0665	30.954	0.148	2.147	0.13	59208
10.59	0.6920	0.0530	0.0608	28.299	0.135	1.849	0.13	59468
11.05	0.6716	0.0443	0.0547	25.447	0.121	1.547	0.13	59736
11.51	0.6373	0.0356	0.0482	22.401	0.107	1.240	0.13	60013
11.97	0.5817	0.0267	0.0412	19.170	0.092	0.931	0.13	60299
12.43	0.4897	0.0178	0.0339	15.760	0.075	0.621	0.13	60594
12.89	0.3280	0.0089	0.0262	12.185	0.058	0.310	0.13	60896
13.35	-0.0002	0.0000	0.0182	8.456	0.040	0.000	0.13	61205

Table D.2: Main performance parameters of the APC 15.75x13-3 propeller: efficiency, thrust coefficient C_T, power coefficient C_P, power, torque, thrust, Mach number M at the propeller tip and Reynolds number Re at 75% of the blade span as functions of the incoming velocity V at 2000 rpm [66].

Appendix E. Tracking ratios

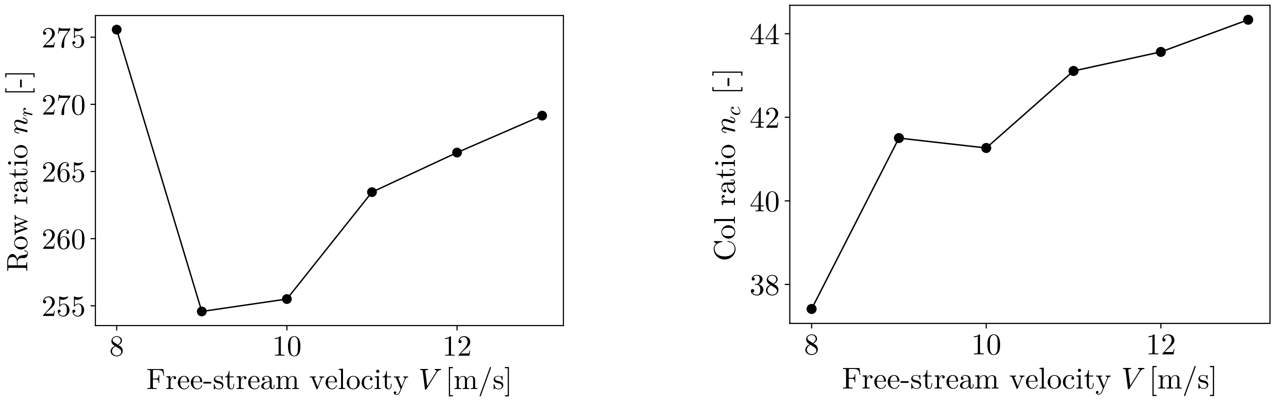

(a) Row tracking index n_r.

(b) Column tracking index n_c.

Figure E.1: Row and column tracking indices n_r and n_c of the backward whirl flutter mode as functions of the free-stream velocity V for the final flexible pylon configuration.

Appendix F. Motor support

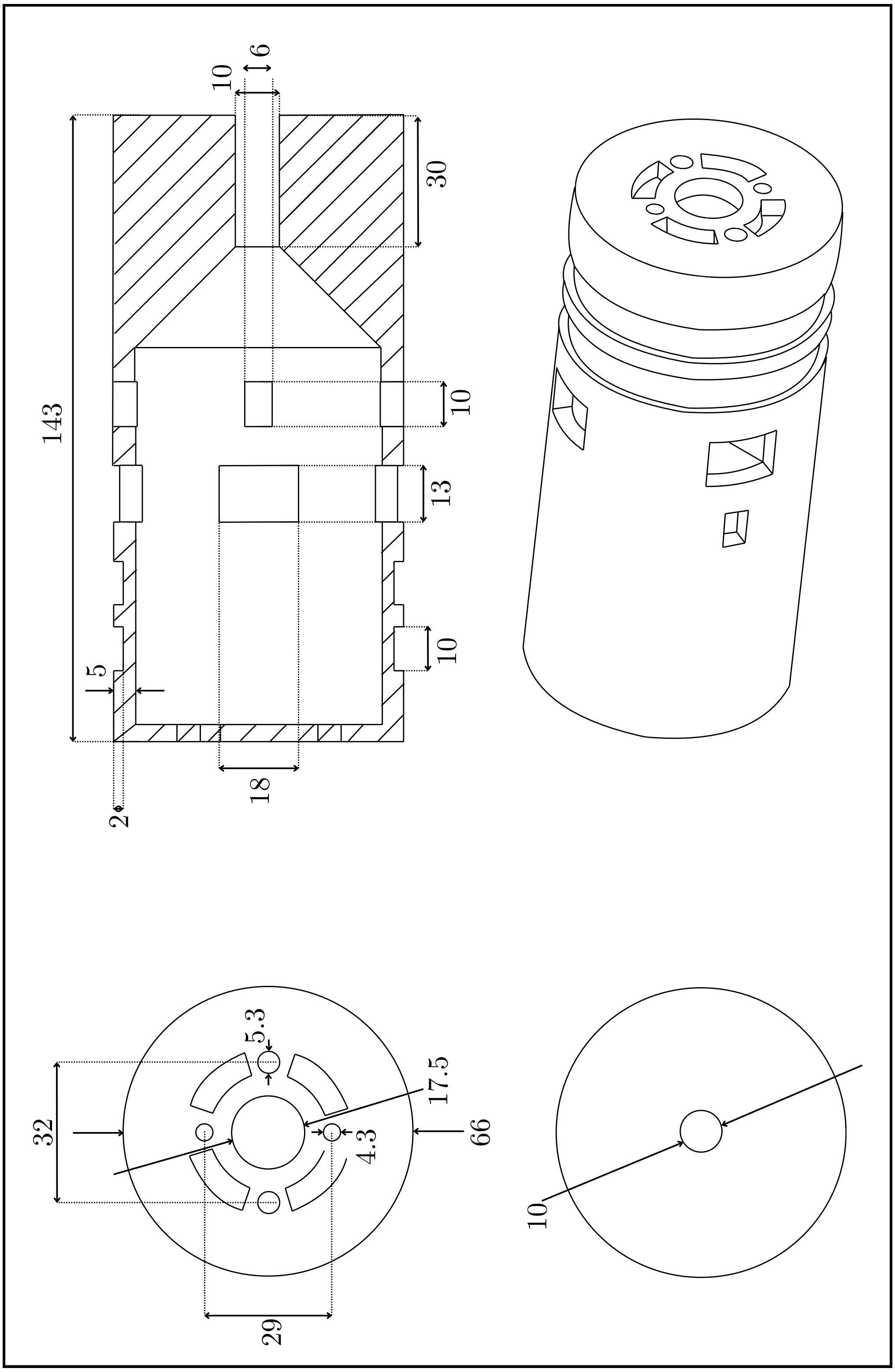

Figure F.1: Technical drawing of the motor support.